



NBSIR 87-3584

Effect of Slag Penetration on the Mechanical Properties of Refractories: Final Report

Report Prepared by

S.M. Wiederhorn and R.F. Krause, Jr.
U.S. DEPARTMENT OF COMMERCE
National Bureau of Standards
Institute for Materials Science and Engineering
Ceramics Division
Gaithersburg, MD 20899

under

Contract Number DE-AI05-83OR21349

for

OAK RIDGE NATIONAL LABORATORY
Oak Ridge, Tennessee 37831
operated by
MARTIN MARIETTA ENERGY SYSTEMS, INC.
for the
U.S. DEPARTMENT OF ENERGY
under Contract No. DE-AI05-83OR21349

QC

100

.U56

NO. 87-3584

1987

DISCLAIMER

This report was prepared as an account of work sponsored by an agency of the United States Government. Neither the United States Government nor any agency thereof, nor any of their employees, makes any warranty, express or implied, or assumes any legal liability or responsibility for the accuracy, completeness, or usefulness of any information, apparatus, product, or process disclosed, or represents that its use would not infringe privately owned rights. Reference herein to any specific commercial product, process, or service by trade name, trademark, manufacturer, or otherwise, does not necessarily constitute or imply its endorsement, recommendation, or favoring by the United States Government or any agency thereof. The views and opinions of authors expressed herein do not necessarily state or reflect those of the United States Government or any agency thereof.

Printed in the United States of America
Available from
National Technical Information Service
U. S. Department of Commerce
5285 Port Royal Road
Springfield, VA 22161

NTIS price codes
Printed copy: A07
Microfiche copy: A01

**EFFECT OF SLAG PENETRATION ON THE MECHANICAL
PROPERTIES OF REFRACTORIES:
FINAL REPORT**

Research sponsored by the U.S. Department of Energy
Advanced Research and Technology Development
Fossil Energy Materials Program

Report Prepared by

S. M. Wiederhorn and R. F. Krause, Jr.
U.S. DEPARTMENT OF COMMERCE
National Bureau of Standards
Institute for Materials Science and Engineering
Ceramics Division
Gaithersburg, MD 20899

under

Contract Number DE-AI05-83OR21349

for

OAK RIDGE NATIONAL LABORATORY
Oak Ridge, Tennessee 37831
operated by
MARTIN MARIETTA ENERGY SYSTEMS, INC.

for the

U.S. DEPARTMENT OF ENERGY
under Contract No. DE-AI05-83OR213490

September 30, 1986

Issued June 1987



U.S. DEPARTMENT OF COMMERCE, Malcolm Baldrige, *Secretary*
NATIONAL BUREAU OF STANDARDS, Ernest Ambler, *Director*

EFFECT OF SLAG PENETRATION ON THE MECHANICAL
PROPERTIES OF REFRACTORIES

	Page No.
<u>INTRODUCTION</u>	1
 <u>APPENDED PUBLICATIONS</u>	
1. Compressive Strength and Creep Behavior of a Magnesium Chromite Refractory	5
2. Creep and Fracture of a Vitreous-Bonded Aluminum Oxide	14
3. Nucleation and Growth of Cracks in Vitreous Bonded Aluminum Oxide at Elevated Temperatures	29
4. Rising Fracture Toughness of an Alumina Ceramic Using the Bending Strength of Indented Specimens	64
5. Coal Slag Penetration in a Magnesium Chromite Refractory	88

1. INTRODUCTION

Recently, in a review of materials for coal gasification applications, Bakker and Stringer noted that the most critical material problem for slagging coal gasifiers is the selection of refractory insulation for the gasifiers. This problem of selecting refractory insulation is the result of refractory lining exposure to the gasifier environment and to slag present in that environment. The lifetime of the refractory depends on the temperature of operation and the composition of slag at the hot face of the refractory. Higher temperatures (1500°C to 1700°C) and more corrosive slags (high alkali; high Fe) reduce the lifetime of refractories. Since slag is a universal solvent for refractories, all refractories eventually dissolve in coal slag. However, by appropriate materials design, the resistance of the refractory to dissolution (and hence lifetime) can be increased.

This project involved basic research to provide fundamental data and models necessary to improve the mechanical behavior of refractories in gasifiers, particularly those of the wet bottom type. The project consisted of two tasks: (1) to characterize the fracture and deformation behavior of high chromia refractories penetrated by slag, and (2) to evaluate the creep and creep rupture behavior of model refractories in terms of mechanisms that explain cavity formation, cavity coalescence, and crack growth in ceramic materials.

2. TECHNICAL PROBLEM AND APPROACH

This project dealt primarily with the structural integrity of refractories that have been penetrated by coal slag. In part 1 of this study, the fracture and deformation behavior of high-chromia refractories, penetrated by slag were characterized. The creep behavior of high-chromia refractories, were determined as a function of applied load and temperature. Changes in density and microstructure were studied for high-chromia refractories subjected to creep deformation. Data were evaluated in terms of mechanisms that have been developed to explain cavity formation, cavity coalescence and crack growth in ceramic materials.

In part 2 of this study, experimental data were collected on model ceramic refractories to identify and quantify high temperature mechanisms that lead to a loss in the mechanical integrity of refractory materials. Studies were conducted on vitreous bonded aluminum oxide to duplicate the type of structure expected at the hot face of refractories in slagging gasifiers. Microstructural variables were the grain size of the Al_2O_3 , and the quantity and viscosity of glass at the grain boundaries. Experiments were of two types: (1) application of mechanical loads to the model refractories to determine the creep and fracture behavior as a function of temperature; and (2) analyses of the microstructure of the deformed ceramics to determine the mechanisms that control their mechanical behavior at elevated temperature.

3. PRINCIPAL FINDINGS

The output on this project included five technical papers in various stages of the publication process. Subjects studied include: an analysis of creep and creep rupture behavior of glass impregnated ceramics; crack nucleation and growth processes in glass impregnated ceramics, creep behavior of magnesium chromite refractories and finally, slag penetration of magnesium chromite refractories; and the effect of slag penetration on strength of magnesium chromite refractories. Complete copies of these publications are included as part of this report.

Principal findings of the project are summarized below:

Magnesium Chromite Refractories:

- o Compressive strength of magnesium chromite refractory was measured to 1600°C; strength decreased with increasing temperature above 1200°C.
- o Creep of magnesium chromite refractory was characterized as a function of compressive stress and temperature in the range 1300°C to 1600°C.
- o The stress exponent and activation energy for creep were evaluated from strain rate data.
- o Magnesium chromite spinel dissolution by slag resulted from the diffusion of FeO/Fe₂O₃ and Al₂O₃ from slag into the refractory to form a low melting solid solution.
- o Viscosity of the slag that penetrated the refractory controlled both dissolution rate of the magnesium chromite spinel and the rate of diffusion of the ions from the brick to the slag. Dissolution rate of the brick is exacerbated by the presence of Ca and Mg which lowers the viscosity of the slag in the brick.
- o Improvement of brick performance might be achieved by the addition of network formers such as Al₂O₃ to the refractory.

Creep and Creep Rupture of Vitreous Bonded Alumina Ceramics:

- o Creep rupture data for vitreous bonded alumina ceramics can be represented by a modified Monkman-Grant equation, which relates the rupture time to the creep rate of the material.

- o Creep rates depend on the viscosity of the glass bonding the aluminum oxide grain: increasing the viscosity of the glass bonding phase reduces the creep rate of the composite material. Devitrification of the bonding phase appears to be a useful way of increasing the viscosity.
- o Crack nucleation occurs in the amorphous intergranular phase in vitreous bonded ceramics. Crack growth occurs primarily through the glass phase, failure occurring at a rupture strain of 0.1% for a ceramic containing 8% vitreous phase and at 1% for a ceramic containing 30% vitreous phase.
- o A new, inexpensive method was developed for determining R-curve behavior of ceramic materials at elevated temperatures. Data collected at room temperature are consistent with data obtained with other techniques of measurement.

Detailed discussion of each of the above accomplishment are given in the papers included in this report. During the course of this project, a total of 8 lectures were presented at scientific meetings and seminars. In addition, five technical papers have been or are in the process of being published. A list of these are given below:

Publications:

1. R.F. Krause, Jr. "Compressive Strength and Creep Behavior of a Magnesium Chromite Refractory," Ceram. Eng., and Sci. Proc. of Amer. Ceram. Soc., 220-228, Jan/Feb (1986).
2. S.M. Wiederhorn, B.J. Hockey, R.F. Krause, Jr. and K. Jakus, "Creep and Fracture of a Vitreous-Bonded Aluminium Oxide," J. Mater. Sci. 21, 810-824 (1986).
3. K. Jakus, S.M. Wiederhorn and B.J. Hockey, "Nucleation and Growth of Cracks in Vitreous Bonded Aluminum Oxide at Elevated Temperature," J. Amer. Ceram. Soc. 69, 725-31 (1986).
4. R.F. Krause, Jr., "Rising Fracture Toughness from the Bending Strength of Indented Alumina Beams," J. Amer. Ceram. Soc., submitted.
5. S.M. Wiederhorn, R.F. Krause, Jr. and J. Sun, "Slag Penetration in a Magnesium Chromite Refractory," Bull. Amer. Ceram. Soc., in preparation.

Technical Talks:

1. R.F. Krause, Jr., "High Temperature Creep Measurements of Refractory Materials," The American Ceramic Society, 86th Annual Meeting, Pittsburgh, PA, May 1, 1984.
2. R.F. Krause, Jr., "Compressive Strength and Compressive Creep of a Magnesium Chromite Refractory in Nitrogen," The Norton Company, Worcester, MA, September 28, 1984.
3. R.F. Krause, Jr. and S.M. Wiederhorn, "Creep Behavior of a Magnesium Chromite Refractory," The American Ceramic Society, 87th Annual Meeting, Cincinnati, OH, May 7, 1985.
4. R.F. Krause, Jr. and S.M. Wiederhorn, "Creep Behavior of a Vitreous-Bonded 85 Percent Alumina Refractory, The American Ceramic Society, 87th Annual Meeting, Cincinnati, OH, May 7, 1985.
5. R.F. Krause, Jr., Jing Sun and S.M. Wiederhorn, "Effect of Coal Slag on the Composition and Creep Behavior of Magnesium Chromite Refractory," The American Ceramic Society, 88th Annual Meeting, Chicago, IL, April 29, 1986.
6. S.M. Wiederhorn, R.F. Krause, T.-J. Chuang and K. Jakus, "Creep and Fracture of Vitreous Bonded Ceramics," 86th Annual Meeting of the American Ceramic Society, Pittsburgh, PA, April 29-May 3, 1984.
7. S.M. Wiederhorn, "Strength versus Crack Size in Vitreous Bonded Aluminum Oxide at Elevated Temperatures," 4th International Symposium on the Fracture Mechanics of Ceramics, Blacksburg, VA, June 19-21, 1985.
8. S.M. Wiederhorn, "Creep Rupture of Ceramic Materials", University of California-Santa Barbara Winter Study Group, 4-16 January 1986.

Compressive Strength and Creep Behavior of a Magnesium Chromite Refractory

RALPH F. KRAUSE, JR.

National Bureau of Standards
Gaithersburg, MD 20899

The compressive strength of a magnesium chromite refractory in nitrogen was measured by rapidly loading specimens to failure at several temperatures up to 1600°C. Strength retrogression was observed at temperatures above 1200°C. The creep behavior of the refractory in nitrogen was measured as a function of compressive stress in the range from 1.4 to 5.6 MPa and as a function of temperature in the range from 1300 to 1600°C. A nitrogen atmosphere was used to suppress distillation of Cr₂O₃. Generally, the experiments were terminated when the specimens sustained from 0.01 to 0.02 creep strain. The creep strain (ϵ) at a given stress (σ) and a given absolute temperature (T) was represented by the following function of time (t), $\epsilon = C t^m$, where (C) depends on stress and temperature. The time exponent (m) was evaluated as less than unity, indicating a strain-hardening model, and was independent of stress and temperature within the precision of measurements. The creep strain rate was represented by the relationship, $(d\epsilon/dt) = A \epsilon^{(1-1/m)} \sigma^n \exp(-Q/RT)$, in which (R) is the molar gas constant. The material constant (A), the stress exponent (n), and the activation energy (Q) were evaluated from a least squares fit of this relationship to the creep data at constant strain.

Introduction

Magnesium chromite refractory brick is a candidate for use as hot face linings in slagging coal gasifiers. Laboratory studies¹ in which cylindrical specimens are rotated in high temperature coal slags indicate that refractories with high chromia content are very resistant to wear by coal slags. However, refractories obtained from a pilot plant after several hundred h service were deeply penetrated by slag and contained intergranular cracks parallel to the hot face, suggesting that creep cracking can be a major cause of failure.¹ In the present study the compressive strength and creep behavior of a commercial magnesium chromite refractory are characterized at high temperatures. This will provide a basis to compare the creep behavior of the refractory when it is impregnated with slag in future studies.

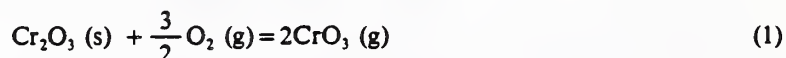
Test Material

Based on a manufacturer's report,² the magnesium chromite refractory material which was used in the present work consisted of 20 wt% MgO and 80 wt% Cr₂O₃. The Cr₂O₃ was slightly in excess over the compound MgCr₂O₄. The refractory was single phase, having the cubic structure of the spinel group. Fused-grain aggregates of magnesium chromite, some of which were as large as 3 mm across, had been sintered in a porous bonding matrix of much smaller grains of the same material. Bulk density measurements indicated a porosity of 14 to 16% based upon the theoretical crystal density of 4.414 g/cm³ at 25°C.

The sample of refractory supplied² was a cross-sectional slice (9 mm × 62 mm × 102 mm) of a manufactured brick from current production. Test specimens were diamond-sawed from the sample and diamond-ground with a 50 μm finish to make bearing faces flat, parallel, and perpendicular to adjacent sides. These specimens (nominally 8 mm × 9 mm × 18 mm high) were used in compressive strength tests and in a series of creep tests described below.

Test Environment

During the high temperature tests, the refractory specimens were kept in a nitrogen atmosphere to suppress oxidation and subsequent distillation of chromia,



At 1600°C the minimum vapor pressure of $\text{MgCr}_2\text{O}_4 (\text{s})$ occurs with an oxygen partial pressure of about 10^{-4} atm.³ At higher oxygen pressures, the partial pressure of $\text{CrO}_3 (\text{g})$ becomes predominant and increases with increasing oxygen pressure. When the partial pressure of oxygen is less than 10^{-4} atm, the partial pressure of $\text{Cr} (\text{g})$ becomes predominant and increases with decreasing oxygen pressure. A flow at 500 mL/min of 99.99 vol% nitrogen was maintained through a gas-tight furnace to keep decomposition of the MgCr_2O_4 specimen at a minimum. An alumina tube (100 mm × 28 mm inside diam) surrounded the specimen in the center of the hot-zone of the furnace and was supported on legs to clear both the furnace floor and ceiling by 25 mm. In this way the furnace interior was protected from exposure to any chromium vapor species. The furnace interior remained uncontaminated while gas circulated freely around the specimen, leaving a slight film of chromia condensed inside the protection tube near its openings.

The gas-tight box furnace had a hot-zone cavity (150 mm cube) that was radiantly heated by molybdenum disilicide resistive elements and could be controlled to operate at a temperature as high as 1600°C. Figure 1 shows a test specimen as mounted between 99.8 wt% recrystallized Al_2O_3 discs (5 mm × 19 mm diam) to prevent contact between the specimen and silicon carbide loading rods (19 mm diam). New discs were ground flat and parallel for each test and were easily separated from the specimen and the loading rods following a high temperature run. The loading rods protruded into the center of the furnace cavity through upper and lower ports which were made in the stainless steel shell and alumina fiber insulation of the furnace. The loading rods were supported and aligned by set screws in socket fixtures that had gas-tight seals with the furnace. The upper fixture was attached to the underside of a moveable crosshead in a frame and was surrounded by a bellows assembly between the crosshead and the furnace top. The lower fixture was attached to a load cell on the frame and was surrounded with a bellows assembly between the load cell and the furnace bottom. Water from a controlled 24°C constant temperature bath circulated through these fixtures to avoid uncertain thermal deformations, which would be especially troublesome in the creep measurements discussed below. This circulating water also cooled the rubber seals of the front door of the furnace and the radiation shields which were placed above and below the furnace shell. The furnace was heated from ambient to 1200°C in about 20 min and thereafter about 20 K/min to attain the test temperature. After reaching temperature, approximately another hour

was required for steady-state temperature equilibration. The temperature of the furnace cavity was controlled within ± 0.5 K and was determined by a calibrated Pt and 6% Rh vs Pt and 30% Rh thermocouple.

Compressive Strength Measurements

The furnace was established in the frame of a universal test loading machine. The gear-driven crosshead of the machine was used at a constant speed of 0.5 mm/min to apply uniaxial, compressive loading on a specimen through a hemispherical block of silicon carbide. Loading was indicated by a linear strain gauge type of load cell and was recorded on a constant-speed chart. The load cell was calibrated at the full scale of the chart with a known 10 kg mass acting at the local $9.801 \text{ m} \cdot \text{s}^{-2}$ acceleration of gravity. Calibration was performed with the furnace at the elevated temperature of a given test to avoid any systematic error due to thermal changes in the spring action of the bellows attached to the load cell. Alternative proportional chart scale factors besides unity (2, 5, 10, 20, 50, and 100) allowed larger loads to be read within $\pm 0.2\%$ full scale.

Figure 2 shows two examples of typical loading versus displacement curves for specimens of the magnesium chromite refractory. The dashed curve, which represents a test at 1200°C, is similar to that obtained in a room temperature test. In these tests, failure of the specimen occurred suddenly. The solid curve, which represents a test at 1500°C, is similar to all tests conducted at temperatures at 1300°C and higher; broadening of the peak load is due to specimen creep. Figure 2 indicates that the displacement, which was deduced from the chart and crosshead speeds, corresponds to about 2% rupture strain at the peak loads.

Figure 3 shows the results of duplicate tests on separate specimens at room temperature in air and at 1200, 1300, 1400, 1500, and 1600°C in nitrogen. The compressive strength for a given specimen was calculated from the observed peak load divided by its initial cross-sectional area. The compressive strength of the magnesium chromite refractory appears to decrease at temperatures above 1200°C and at 1600°C is about one-third of the room temperature value.

Compressive Creep Measurements

Creep specimens of the refractory were mounted in the same apparatus as that used for the compressive strength measurements. A preload of 50 N was applied to a specimen prior to heating in order to maintain alignment. Crosshead movement was controlled automatically by the test machine to accommodate thermal expansion during heat up and to maintain the preload within 10% variation. Temperature equilibration of the loading train at the test temperature was indicated by a steady crosshead position. A linear voltage displacement transducer, calibrated with gauge blocks, was used to monitor the crosshead displacement resulting from the specimen deformation. The transducer was sensitive to $\pm 1 \mu\text{m}$ displacement which corresponds to about $\pm (5) 10^{-5}$ creep strain. A creep test was initiated by application of a test load in the range from 100 to 400 N. The load was held constant within $\pm 0.5\%$ full scale chart throughout the test by automatic adjustment of the crosshead position, using intermittently a crosshead speed of 0.8 mm/h. Variation in stress due to specimen deformation during the test was assumed negligible. Creep strain was measured as a function of time following the initial elastic

and plastic strain. Generally, the experiments were terminated when the specimens sustained from 0.01 to 0.02 creep strain.

Creep measurements were conducted on 9 specimens. The stress and temperature applied to a given specimen were kept constant during a test. In the collection of tests the stress ranged from 1.4 to 5.6 MPa and the temperature ranged from 1300 to 1600°C. The duration of the creep tests varied from about 3 to 170 h. Figure 4 shows a typical experiment of creep strain vs time. Absolute values of strain were used to facilitate an analysis. Note that no steady-state creep rate was attained.

Analysis of Creep Data

The compressive creep strain (ϵ) of a given specimen under a constant stress and at a constant temperature was found to be represented within 1% by the following primary creep function⁴ of time (t)

$$\epsilon = Ct^m \quad (2)$$

in which (C) and (m) are coefficients that were evaluated by a least squares fit of Eq. 2 for each experiment. An example of such a fit is the line in Fig. 4.

No systematic trend of the time exponent (m) was apparent either as a function of the applied stress or as a function of temperature. Figures 5 and 6 show (m) as the slope of $\log_e(\epsilon)$ versus $\log_e(t)$ for various stresses applied to specimens kept at constant temperature, and for various temperatures applied to specimens held at constant stress, respectively. In these figures the slopes are roughly parallel. The mean value of (m) for 9 experiments was 0.74 with ± 0.16 standard deviation of an individual measurement. If any creep strain that might have occurred during the period of temperature equilibration of a specimen under the preload were included, a lower value of (m) and perhaps a better precision would have resulted.

Differentiation of Eq. 2 and substitution of the strain equivalent of time gives

$$d\epsilon/dt = mC^{1/m}\epsilon^{(1-1/m)} \quad (3)$$

which shows a strain-hardening effect for (m) < 1. Thus, the creep rate ($d\epsilon/dt$) decreases continually as the strain (ϵ) increases, exemplifying primary creep. The parameter (C) is a function of the applied stress (σ) and the absolute temperature (T).

Using customary stress and temperature functions,⁵ the creep strain rate can be represented as follows:

$$d\epsilon/dt = A \epsilon^{(1-1/m)} \sigma^n \exp(-Q/RT) \quad (4)$$

where (A) is a material constant, (n) is the stress exponent, (Q) is the activation energy, and (R) is the molar gas constant. Strain rates were calculated from Eq. 3, using values of strain generated in increments between 0.002 and 0.02. At constant strain (ϵ) and the mean value of the time exponent (m), the coefficients A , n , and Q were evaluated by a least squares fit of the \log_e of Eq. 4 to the strain rates at their respective stresses and temperatures. Although the resulting values of the coefficients of Eq. 4 had a slight systematic trend over the generated range of strain, they could be considered constant within the precision of measurements. Table I shows the values of these coefficients. Figures 7 and 8 show the stress exponent (n) and the activation energy (Q) as slopes of $\log_e(d\epsilon/dt)$ vs $\log_e(\sigma)$ and vs $1/T$, respectively.

Summary

The compressive strength of a magnesium chromite refractory was measured at temperatures up to 1600°C. The strength decreased with increasing temperature above 1200°C.

The creep behavior of the magnesium chromite refractory was measured as a function of compressive stress in the range from 1.4 to 5.6 MPa and as a function of temperature in the range from 1300 to 1600°C. The strain rate of this refractory was represented by a strain-hardening model.

The stress exponent and the activation energy for the creep of the magnesium chromite refractory were evaluated from the strain rate data at constant strain.

Acknowledgment

Funding was provided by the U.S. Department of Energy, Fossil Materials Program, Oak Ridge National Laboratory, Oak Ridge, TN. Helpful discussions with Sheldon Wiederhorn, who suggested the work be undertaken, and with Robert Polvani are gratefully acknowledged.

References

- ¹W. T. Bakker, S. Greenberg, M. Trondt, and U. Gerhardus, *Am. Ceram. Soc. Bull.*, 63 870-6 (1984).
- ²M. E. Washburn, private communications, The Norton Company, Worcester, Massachusetts, March 9, 1984.
- ³T. Sata, T. Sasamoto, H. L. Lee, and E. Maeda, *Rev. Int. Hautes Temp. Refract.*, 15 237-48 (1978).
- ⁴J. D. Lubahn and R. P. Felgar, p. 157 in *Plasticity and Creep of Metals*, John Wiley and Sons, Inc., New York, 1961.
- ⁵J. T. Boyle and J. Spence, pp. 12-13 in *Stress Analysis for Creep*, Butterworths, London, 1983.

Table I. Values of the coefficients of Eq. 4 for the creep of magnesium chromite refractory at 1% strain

m	0.74 ± 0.16
n	2.26 ± 0.23
Q, kJ/mol	364 ± 29
log _e A ^a	12.95 ± 1.97
Number runs	9
Residual standard deviation of log _e (dε/dt)	± 0.28

^aCorresponds to stress in MPa and time in h. The uncertainties are the standard deviations of the respective coefficients.

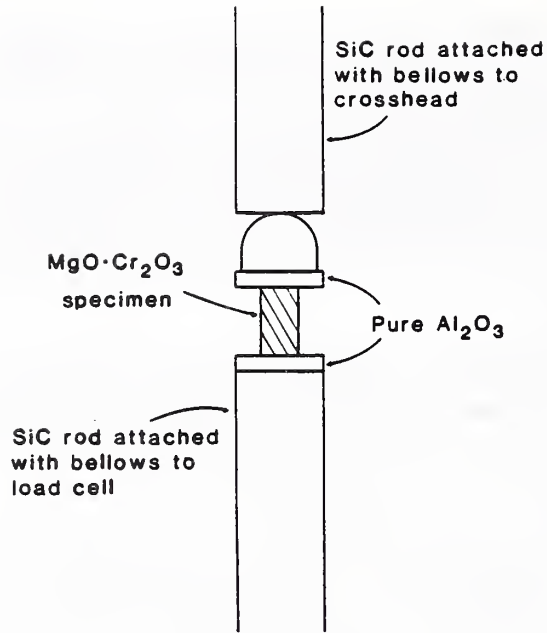


Fig. 1. Schematic of compressive loading of specimen.

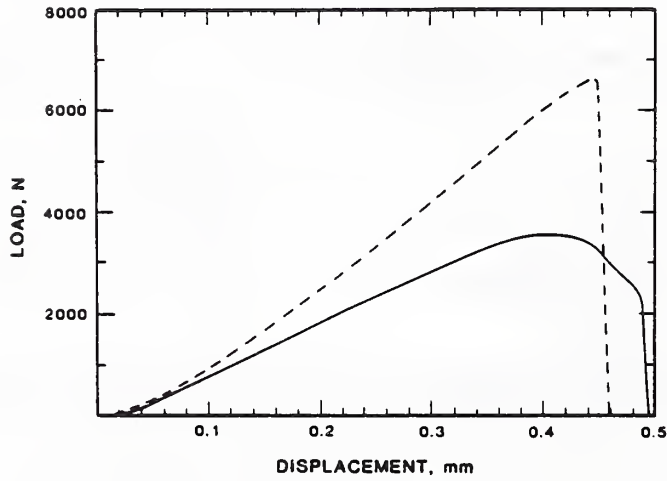


Fig. 2. Typical compressive loading tests conducted at constant 0.5 mm/min displacement rate for magnesium chromite refractory specimens (8 mm × 9 mm × 18 mm high) in nitrogen at 1200°C (dash) and 1500°C (solid).

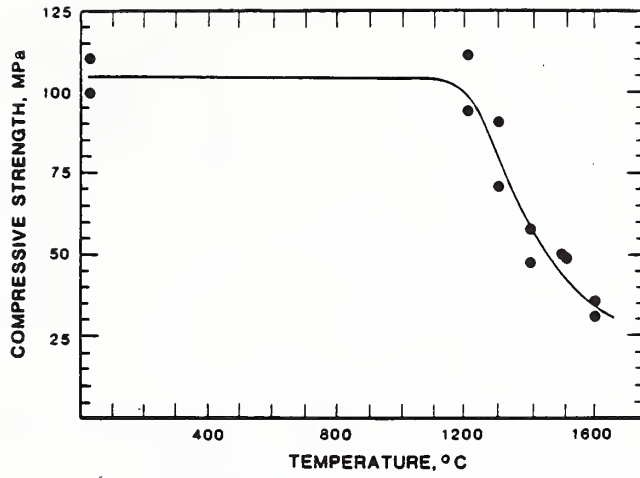


Fig. 3. Compressive strength of magnesium chromite refractory specimens in nitrogen as a function of temperature.

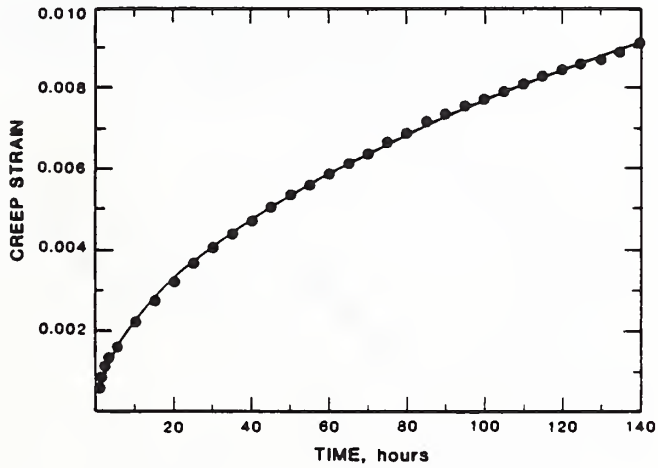


Fig. 4. Typical experiment for compressive creep of a magnesium chromite refractory specimen in nitrogen, in this case at 1400°C under an applied stress of 2.25 MPa. The circles denote observed values, and the line represents Eq. 2 fitted by a least squares method.

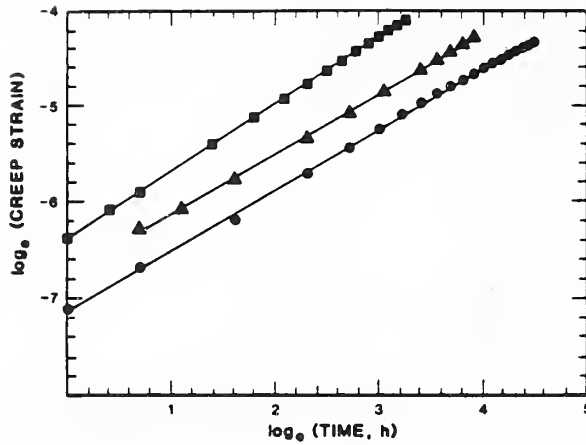


Fig. 5. Time exponent (m) as the slope of \log_e of creep strain vs \log_e of time at various applied stresses on a magnesium chromite refractory in nitrogen at 1500°C. The circles, triangles, and squares denote observed values for separate specimens under applied stresses of 1.4, 2.2, and 3.5 MPa, respectively. The lines represent the \log_e of Eq. 2 fitted by a least squares method.

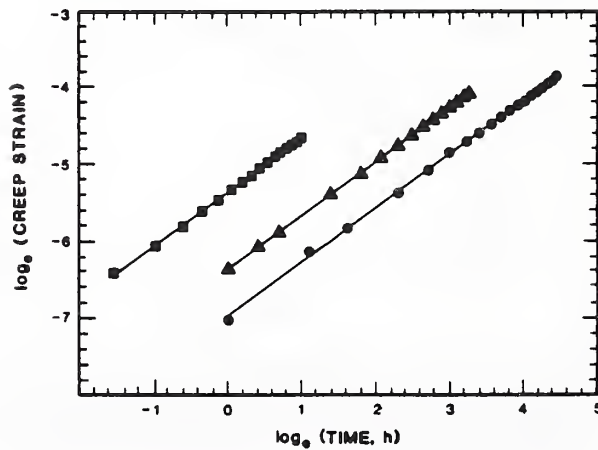


Fig. 6. Time exponent (m) as the slope of \log_e of creep strain vs \log_e of time at various temperatures of a magnesium chromite refractory under applied stress of 3.5 MPa in nitrogen. The circles, triangles, and squares denote observed values for separate specimens at temperatures of 1400, 1500, and 1600°C, respectively. The lines represent the \log_e of Eq. 2 fitted by a least squares method.

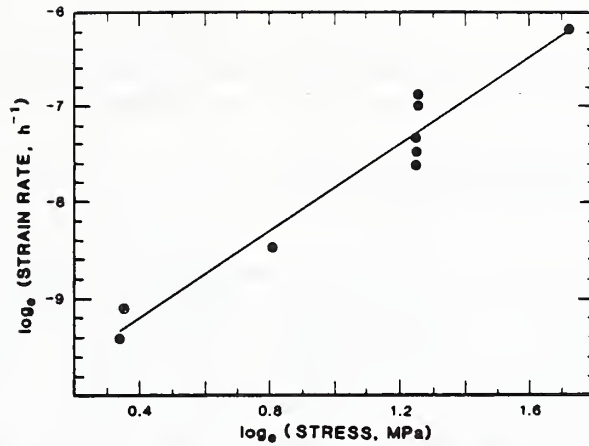


Fig. 7. Stress exponent (n) as the slope of \log_e of stress for a magnesium chromite refractory in nitrogen. The circles are observed strain rates that were temperature corrected to 1500°C, using the fitted value (Q) in Eq. 4, and the line represents the \log_e of Eq. 4 fitted by a least squares method.

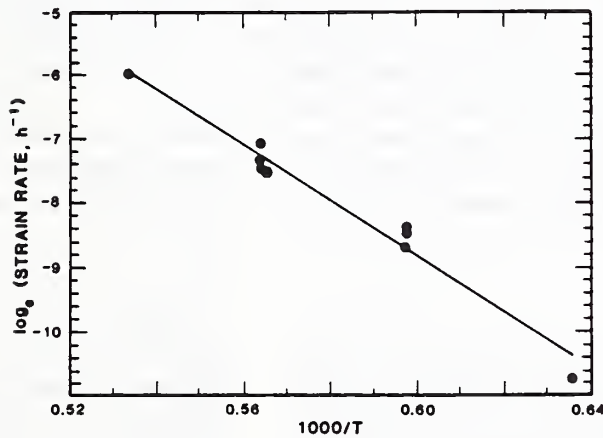


Fig. 8. Activation energy (Q) as the slope ($-Q/R$) of \log_e of strain rate at 0.01 creep strain vs absolute reciprocal temperature for a magnesium chromite refractory in nitrogen. The circles are observed strain rates that were stress corrected to 3.5 MPa, using the fitted value (n) in Eq. 4, and the line represents the \log_e of Eq. 4 fitted by a least squares method.

Creep and fracture of a vitreous-bonded aluminium oxide

S. M. WIEDERHORN, B. J. HOCKEY, R. F. KRAUSE, Jr
National Bureau of Standards, Gaithersburg, Maryland 20899, USA

K. JAKUS
University of Massachusetts, Amherst, Massachusetts 01003, USA

Creep and creep-rupture behaviour of a commercial grade of glass-bonded, 96% aluminum oxide was characterized as a function of temperature and applied stress. The creep data were fitted to the classical empirical relation usually used to describe this phenomenon. The apparent activation enthalpy, $\Delta H = 926 \text{ kJ mol}^{-1}$, and the stress exponent, $n = 4.8$, lie at the high end of the range reported for two-phase materials, primarily as a result of structural modifications that occur during creep. A stress-modified Monkman-Grant relationship was fitted to the creep-rupture data to give a stress exponent of -4.2 . None of the available theories of creep rupture provided a satisfactory description of the present set of data. Analytical electron microscopy was used to characterize the composition and structure of this material. In the as-received material the intergranular phase was a glass of nearly uniform composition. During high-temperature exposure, devitrification of the glass resulted in the formation of various crystalline phases within the intergranular region of the material. Devitrification depended on both the proximity to the surface, where it was most pronounced, and on the state of stress. In this regard, flexural creep samples exhibited extensive crystallization within the tensile region of the flexural specimens, but little crystallization within the compressive cross-section. From the composition of the retained glass, estimates of the viscosity of the glass at the grain boundaries were made and used, in combination with microstructural information, to compare the creep behaviour with available theories of creep. The results of this paper are consistent with percolation and solution precipitation mechanisms of creep deformation. By contrast, cavitation did not seem to play a major role in the creep deformation process.

1. Introduction

Current interest in the mechanical behaviour of multi-phase ceramics has its origin in the potential use of these materials in high-temperature structural applications. In the automotive industry, for example, two-phase ceramics such as sintered silicon nitride and glass-bonded cordierite are being used as structural materials for combustors, turbines, turbochargers and heat regenerators [1]. In the power industry, two-phase materials are being considered for heat recuperators and for linings in slagging gasifiers [2]. In these applications, the mechanical response of the ceramic to external forces depends on the microstructure, in particular on the refractoriness and chemical activity of the phases that make up the ceramic. Most high-temperature structural ceramics consist of highly refractory grains bonded by a less refractory vitreous intergranular phase. Therefore, creep and creep rupture of these materials depend primarily on the physical and chemical properties of the vitreous phase and on the amount and distribution of the vitreous phase within the ceramic structure.

Because of the importance of the intergranular vitreous phase for the structural integrity of high-

temperature ceramics, most recent studies on these materials have concentrated on characterizing the behaviour of the vitreous phase as a means of understanding the behaviour of the ceramic composite. Thus, Lange *et al.* [3] have shown how the compressive creep behaviour of silicon nitride can be modified by changing the composition and volume fraction of the glassy phase within hot-pressed silicon nitride. These authors also demonstrated that high-temperature exposure, which removes glass modifiers from the vitreous matrix, also greatly reduces the susceptibility of the hot-pressed silicon nitride to creep [4]. These findings reinforced earlier findings of Kossowsky, Miller and Diaz [5], who showed that glass modifiers, such as calcium, reduce the viscosity of glass and therefore increase the susceptibility of hot-pressed silicon nitride to creep. Similar findings were made by others on porcelains [6], fire bricks [7] and glass ceramics [8].

Despite our general understanding of the importance of glass composition and structure in creep and fracture, it is only now with the development of high resolution analytical microscopy that the chemical composition of the glass bonding phase can be deter-

mined. Evaluation of the glass composition opens the possibility of estimating physical properties of the glass matrix, such as diffusivity or viscosity, which are required for the critical evaluation of most theories of creep and creep rupture. By analysing the composition of the vitreous matrix, these physical properties can either be determined experimentally on a similar composition of glass, or estimated theoretically, and a direct comparison between these theories of creep and creep rupture, and experimental creep and creep-rupture data, can then be made.

In this paper analytical electron microscopy is used to elucidate the creep and creep-rupture behaviour of a commercial grade of vitreous bonded aluminum oxide. The chemical composition of the glass bonding phase is determined before and after static annealing and creep deformation. From the chemical compositions, theoretical estimates of the viscosity of the glasses are made in order to compare creep and creep-rupture theory with experimental data. The electron microscope is also used in a more classical way: as a method of identifying changes in the microstructure that occur during creep. Using these methods, the creep rate is shown to be determined by the viscosity of the glass, suggesting that viscous flow and/or solution precipitation contribute to the creep process. Although cavitation is not observed to occur homogeneously in our specimens, cavitation at select boundaries followed by crack growth is believed to be important in later stages of the creep process.

2. Experimental procedure

Creep and creep-rupture experiments were conducted on a commercial grade of vitreous bonded aluminum oxide, COORS AD-96,* reported to contain 96% aluminum oxide. Experiments were conducted using four-point bending as a test technique. This technique was selected for ease of testing and for the fact that specimens for the electron microscope could be obtained from the tensile and compressive portions of the same specimen, thus excluding thermal history and extent of strain in comparative analysis. Creep-test specimens, 3 mm high and 5 mm wide, were loaded on a bending fixture of silicon carbide with outer and inner loading points of 40 and 10 mm, respectively. Approximately half the specimens were polished on the tensile surface to permit identification of incipient failure sites and crack nuclei as they formed during creep. Dead-weight loads from 40 to 100 N were applied via a lubricated rubber diaphragm air cylinder, which, in combination with a two-step, continuous leak pressure regulator, was capable of maintaining the applied load to within ± 1.5 N. Stress and strain were calculated by the procedure given by Hollenberg *et al.* [9], assuming a stress exponent of unity. No further corrections to the estimated stresses and strains were made in the present paper.

The loading point displacement during creep was monitored by a linear voltage displacement transducer

(LVDT) that was attached to the upper ram of the test equipment. The loading point displacement of specimens was measured to within $\pm 2 \mu\text{m}$. To enhance the long-term accuracy of the displacement readings, a block of sintered silicon carbide, of the same grade as that used for the rams, was used in one of the three test stations in each furnace. Since the block did not undergo creep at the loads and temperatures used in the present study, any displacement measured by the LDVT on the block reflected changes in the test facility due to electronic drift or to fluctuations in the ambient temperature. These displacement fluctuations were subtracted from the displacements measured on the specimens in the other two stations of the same furnace, so as to minimize errors due to electronic drift or to differential thermal expansion of the test fixture. Even though two specimens were tested in the same furnace for each run, the failure of one specimen was never observed to affect the other in the course of our investigation, primarily because pneumatic pistons and rubber shock absorbers were used to restrain the propagation of stress waves.†

Recognizing that phase changes often occur in ceramics during extended high-temperature exposure [6, 7], most specimens were annealed at 1050°C for a period of 96 h before testing to stabilize the ceramic against composition or structural changes that might influence the creep behaviour. Since most of the creep studies in this programme were typically less than 100 h duration, it was hoped that this annealing period would be sufficient to ensure a constant structure for the present investigation. Despite this precaution, some phase changes were observed during creep. The affect of annealing on both creep and microstructure represents an important aspect of our results, and accordingly will be discussed extensively below.

To establish the temperature range to be investigated, a stepped-temperature creep test [10] was conducted using an initial applied stress of 60 MPa, which was approximately one-third of the reported breaking stress at 1000°C. In this test a constant load was applied to the specimen, and the temperature was increased at various time intervals either until failure occurred, or deformation was so severe that further creep was pointless. Significant creep activity for this material starts at approximately 950°C; at 1050°C the creep of the ceramic is relatively rapid, failure occurring in approximately 24 h at approximately 0.14% strain. Based on these results, experiments were conducted at temperatures ranging from 980 to 1100°C, and at applied stresses ranging from 40 to 100 MPa.

Specimens for examination by transmission electron microscopy (TEM) were obtained from the deformed bend bars using standard sectioning, polishing and ion-milling techniques. Two types of sections were used in these studies (Fig. 1). Specimens with the major plane of the foil parallel to the plane of maximum tensile or compressive stress were used to analyse the near-surface regions of the specimen, i.e.

*Coors Porcelain Co., 600 Ninth Street, Golden, Colorado. Identification of this material is not to be construed as endorsement by the National Bureau of Standards.

†Bellows are a non-inertial method of loading the specimens, and the air gaps in the bellows do not permit the passage of a stress wave. Hence, when a specimen breaks, the stress waves resulting from the fracture are largely dissipated before reaching the second specimen.

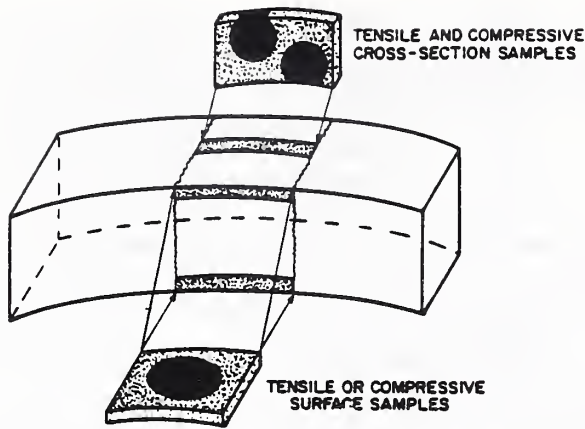


Figure 1 Schematic diagram of bend bar showing regions from which thin sections were prepared for examination by transmission electron microscopy.

from 0 to 50 μm from the external surface. Specimens with the plane of the foil perpendicular to the bending axes were used to examine changes in composition and structure at greater distances (0.2 to 1 mm) from the tensile or compressive surfaces of the creep specimens. This orientation was selected to examine the ceramic structure as a function of distance from the tensile and compressive surfaces of the bend bars.

3. Experimental results

3.1. Microstructure

A representative view of the material used in this study is shown in Fig. 2. The material consists principally of aluminum oxide grains (A) bonded by an intergranular glassy phase (M). Interspersed throughout the material there are also abnormally large grains of spinel (MgAl_2O_4), S, ranging in size from 20 to 40 μm , and irregularly shaped pores of microscopic (5 to 10 μm) dimensions. Using the line-intercept method, the mean grain size of Al_2O_3 was determined to be 8 μm , but ranged from 3 to 20 μm . The volume fraction of intergranular glassy phase, which was located primarily at multi-grain junctions, was roughly 8%. The porosity of the material was also roughly 8% by volume.

In applying TEM, major emphasis was placed on

determining the structure and chemical composition of the intergranular phase. Chemical compositions were determined by energy dispersive X-ray analysis (EDX) using the ratio method in the thin-foil approximation [11] after background subtraction by linear extrapolation. The required K values for the various oxides[‡] were determined from spectra obtained from two glass standards (Table I), which were also prepared by ion milling. In all cases, spectra from either the standards or the unknowns were taken under similar conditions (beam current, beam size, angle of tilt, etc.), a precaution necessitated by the presence of sodium in both the glass bonding phase and in one of the crystalline products of devitrification. The highly volatile nature of sodium during electron irradiation, moreover, placed severe restrictions on the imposed electron beam flux and duration of exposure. Most generally, this precluded the use of a focused probe regardless of other operating conditions and required the use of defocused beams of (typically) 400 μm or greater in diameter. While many grain-boundary widths were considerably smaller than this limiting probe size, most joined continuously with triple junctions of larger dimensions. As a check on spacial resolution, "hole count" spectra obtained from etched-out grain boundaries and triple junctions showed only an insignificant aluminum intensity enhancement, while differences in the elemental composition of the various intergranular phases allowed for a ready check on possible "overlap". In all cases, chemical compositions are given in terms of average values obtained from at least ten determinations.

Transmission electron microscopy provided not only a more detailed view of the microstructure, but also revealed that pronounced changes occur within the intergranular bonding phase due to prolonged static annealing and creep. In the as-received material, the intergranular bonding phase was found to consist entirely of a glass (Fig. 3). EDX analyses of the glass found at triple junctions (Fig. 3a), two-grain boundaries (Fig. 3b), and larger multi-grain junctions or "pockets" gave a fairly uniform composition listed in Table II. Though not particularly evident in Fig. 3, most Al_2O_3 grains were separated by a glass film

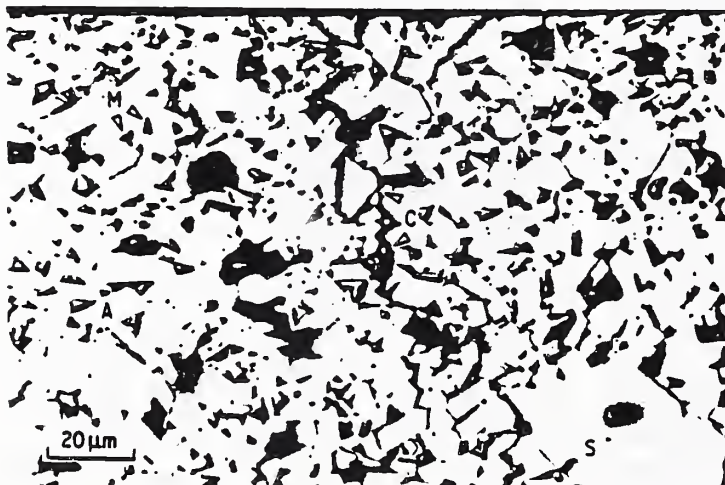


Figure 2 Light micrograph of longitudinal cross-section from creep sample. Relief polishing distinguishes intergranular phase (M) from aluminum oxide grains (A) and abnormally large spinel grains (S). Also evident are large pores, inherent in the material. Arrow indicates tensile creep crack that extends part way through the sample. Note that crack path is entirely intergranular.

[‡]It was assumed that all constituents were present as stoichiometric oxides.

TABLE I Glasses used for calibration purposes in the present study

Glass	Component (wt fraction)							
	SiO ₂	Al ₂ O ₃	B ₂ O ₃	FeO	Na ₂ O	K ₂ O	MgO	CaO
Soda-lime silica	0.72	0.02	—	—	0.14	0.01	0.04	0.07
K-412*	0.45	0.09	—	0.10	—	—	0.19	0.15
Cl720†	0.62	0.17	0.05	—	0.01	—	0.07	0.08
C0080†	0.73	0.01	—	—	0.17	—	0.04	0.05

*NBS Standard Reference Material, SRM 470. Compositions in the standard are reported to better than two significant figures.

†Corning Glass Co. See Hutchins and Harrington [21] for compositions. The use of this glass does not imply endorsement by the National Bureau of Standards.

which, due to the irregular morphology of the Al₂O₃ grains, ranged in thickness from roughly 10 nm upwards of several tenths of a micrometre. In this regard, the relatively wide, glassy grain-boundary region — as well as the apparent Al₂O₃ surface faceting — seen in Fig. 3b was not uncommon. The results thus indicate that, in the as-received condition, the bonding phase can be regarded as a continuously linked, glassy structure.

Upon prolonged annealing (1050° C, 96 h), pronounced changes were found within the bonding phase due to partial devitrification of the glass. Specifically, devitrification results in the formation of various crystalline phases and, as a consequence, changes the volume fraction and composition of the retained glassy phase. Although devitrification occurs throughout the samples, it is most pronounced within the surface regions. Accordingly, results obtained from the interior and from the surface regions of bulk, annealed samples are described separately. Within the interior of annealed samples, analytical electron microscopy revealed only the presence of two different magnesia aluminosilicate phases within the bonding phase: one having an average composition of 4MgO · Al₂O₃ · 4SiO₂ and being isomorphous with orthorhombic enstatite (MgSiO₃), the other having an average composition of 2MgO · 2Al₂O₃ · SiO₂ and being isomorphous with monoclinic sapphirine (4MgO · 5Al₂O₃ · 2SiO₂).

Moreover, small crystallites of one or both of these phases were found within many, but not all, of the larger triple junctions or multi-grain "pockets" (Fig. 4a), and never within two-grain boundaries. Because of this, devitrification results in only a minor decrease in the volume fraction of the glassy phase, (estimated at less than 10%). This, however, is sufficient to produce a significant change in glass composition which from Table II is seen to be nearly depleted in MgO. Here it is important to note that the observed change in glass composition was uniform throughout the interior of annealed samples, regardless of whether localized crystallization had occurred.

As indicated earlier, devitrification was especially pronounced within the surface regions, where it is estimated that from 50 to 75% of the intergranular glassy phase devitrified during annealing. Although enhanced formation of both magnesia-aluminosilicate crystalline phases at the surface played a role in reducing the volume fraction of glass, the reduction of the glass fraction was primarily related to the formation of a triclinic, sodium-calcium aluminosilicate phase identified by electron diffraction and chemical analyses (Table II) as intermedite plagioclase.[§] Unlike the magnesia-aluminosilicate phases, the intermedite plagioclase formed more uniformly throughout the intergranular regions and often resulted in the (apparently) complete crystallization of two-grain

TABLE II Chemical analysis of residual glass at grain boundaries of AD-96 aluminum oxide

Treatment	Composition (mol %)				
	Na ₂ O	MgO	CaO	Al ₂ O ₃	SiO ₂
As-received	5.03 (1.25)*	11.21 (1.63)	2.77 (0.37)	16.11 (0.91)	64.88 (2.33)
Annealed† (unstressed material)	5.05 (0.86)	3.37 (0.35)	3.72 (0.44)	16.09 (0.76)	71.78 (1.80)
Annealed (100 μm thin section)	4.41 (1.85)	2.50 (0.76)	0.66 (0.16)	14.60 (0.96)	77.78 (3.13)
Tensile surface	3.52 (1.44)	2.74 (0.39)	0.65 (0.12)	13.42 (0.45)	79.67 (1.49)
Tensile surface	3.66 (1.09)	2.62 (0.04)	0.92 (0.17)	14.13 (0.63)	78.52 (1.65)
Compressive surface	3.61 (0.67)	3.02 (0.65)	0.92 (0.13)	14.70 (0.47)	77.75 (1.42)
Tensile section	2.83 (1.73)	3.03 (0.82)	1.97 (0.55)	15.26 (0.90)	76.96 (2.36)
Compressive section	3.24 (1.78)	3.31 (0.72)	3.44 (0.40)	16.48 (1.17)	73.59 (2.46)

*The standard deviation of each measurement is given in parentheses.

†Annealed for 96 h at 1044° C, then subjected to creep for ~50 h at an initial applied stress of 60 MPa. The unstressed material was taken from the end of the specimen.

§The chemical composition of members of the plagioclase series is generally given in terms of its pure end-members anorthite (An), CaAl₂Si₂O₈, and albite (Ab), NaAlSi₃O₈. On this basis, the average composition listed in Table II corresponds to 50% Ab · 50% An, although considerable variations in compositions and a systematic calcium deficiency were observed.

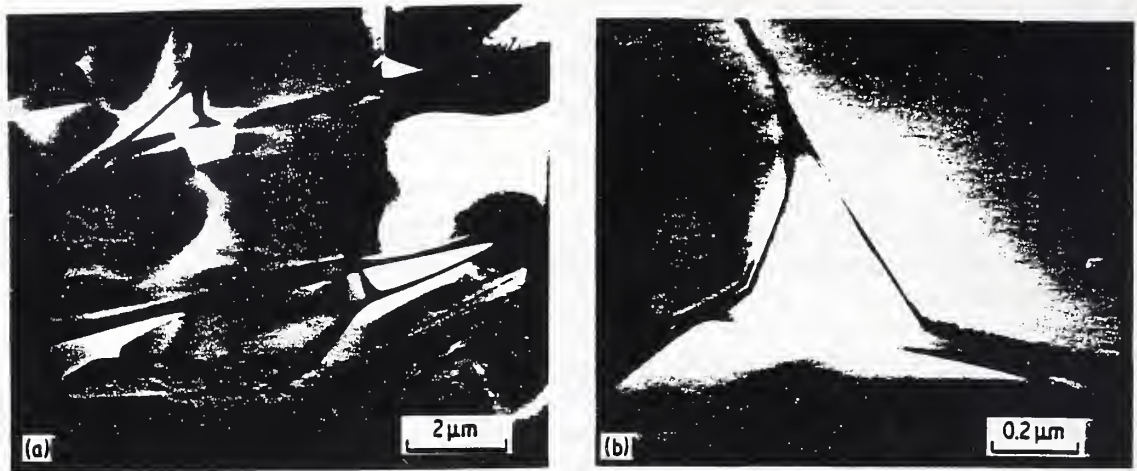


Figure 3 TEM illustrating microstructure of vitreous bonded alumina in as-received condition. (a) Representative view showing non-uniform morphology of aluminium oxide grains and glassy binder phase at triple junctions. (b) Enlarged view of structureless glassy phase at triple junctions and between widely separated grains. Surface faceting of aluminium oxide grains evident in (b) was characteristic feature of vitreous-bonded material.

boundaries and multi-grain junctions (Fig. 4b). Moreover, the additional crystallization of plagioclase within the surface regions results in a retained glass phase composition (Table II) which is more silica-like, and hence is different from the glass phase found within the interior.

To a large extent, analytical electron microscopy results for annealed samples provide a basis for summarizing the differences in microstructures found within samples that were preannealed at 1050°C and then deformed in creep to -0.1% strain at an applied stress of 60 MPa. Particular emphasis is again placed on the intergranular regions, since this is where deformation occurs. With reference to Fig. 1, samples taken from within 100 μm of the tensile and compressive surfaces of deformed samples were virtually indistinguishable from each other and from those from the surfaces of statically annealed samples. In each, the intergranular binder phase was largely crystalline (again estimated as up to 75% of binder phase volume), due to the formation magnesio-aluminosilicates and intermediate plagioclase. From

Table II, the compositions of retained glass in the surface intergranular regions were also quite similar. Tensile surface sections were, however, marked by the occasional presence of stoichiometric, orthorhombic cordierite and, in samples where the original surface was retained, by the presence of discrete magnesio-aluminosilicate crystallites along the periphery of two-grain boundaries and multi-grain junctions. By scanning electron microscopy (SEM) these crystallites were determined to lie on the surface, thus indicating a transfer of material from the interior to the tensile surface.

Further examination of deformed samples, using longitudinal cross-sections (Fig. 1), provided clear evidence that the stresses developed during testing have a significant effect on the devitrification process, and hence on the structure and composition of the intergranular bonding phase. Within the tensile regions, extensive devitrification of the glass binder phase resulting in 50 to 70% crystallization, extending to distances of approximately one-fourth the sample thickness, the limit of observations (Fig. 5). In con-

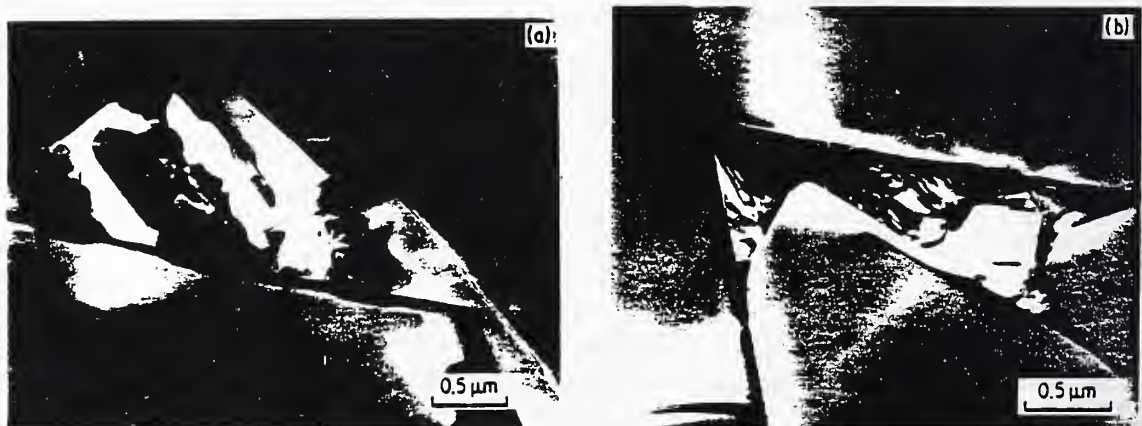


Figure 4 TEM results. (a) Discrete crystallites of magnesio-aluminosilicate phases (see text for description) produced within multi-grain junction after prolonged heat treatment at 1050°C. Nature and extent of crystallization typifies partial devitrification of glassy binder phase that occurs within interior of bulk samples. (b) Fully crystallized intergranular structure typically produced within near-surface regions after similar heat treatment. More complete devitrification is related to additional formation of intermediate plagioclase. As described in text, (a) is also typical of compressive subsurface regions and (b) typical of tensile subsurface regions after flexural creep.

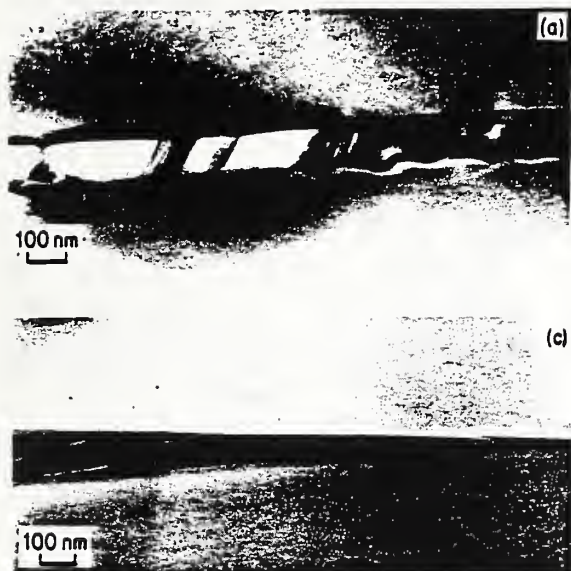


Figure 5 TEM results. Examples of crystallized grain boundary structures, invariably intermediate plagioclase, produced within tensile regions of flexural creep samples.

trast, the degree of devitrification diminished rapidly below the compressive surface, and at a depth corresponding to one-tenth the sample thickness the bonding phase was essentially glassy. Within the compressive regions, the structure and composition of the bonding phase was, in fact, nearly identical to that found within the interior of bulk annealed samples, whereas within the subsurface tensile region it closely resembled that found at the surface. These results suggest a net increase in specific volume of the bonding phase (i.e. the combined volume change of the glass and crystalline phases at the grain boundaries) as a result of the devitrification process. Thus, devitrification would be enhanced in the tensile cross-section of the specimen, and retarded in the compressive cross-section of the specimen.[†]

Creep samples were also examined for evidence of void or cavity formation within the intergranular phase. In contrast to earlier results for hot-pressed

silicon nitride (tested in both tension and compression) [3, 5, 13–15] and for a glass-bonded alumina (tested in compression) [16], definitive evidence for widespread cavitation was not found.[‡] Nevertheless, observations on tensile surface regions by SEM (Fig. 6a) clearly showed intergranular cavitation, though it was generally restricted to the neighborhood of well-developed creep cracks. In addition, TEM studies on similar tensile surface sections revealed occasional evidence of grain-boundary delamination in the form of narrow plate-like cavities (Fig. 6b). While it appears clear that grain-boundary delamination eventually leads to the formation of fully developed cracks that are responsible for creep rupture, the necessary conditions and processes involved in crack formation remain the object of continuing study.

3.2. Creep data

Examples of creep data obtained in the present experiments are illustrated in Figs. 7 and 8. There was little indication of Stage 3 creep prior to failure in any of the creep tests. Failure often occurred without any change in the creep rate, suggesting that a second process, such as rapid crack growth, abruptly cuts off the normal creep process in these specimens. Sometimes a slight increase in the creep rate is observed just before

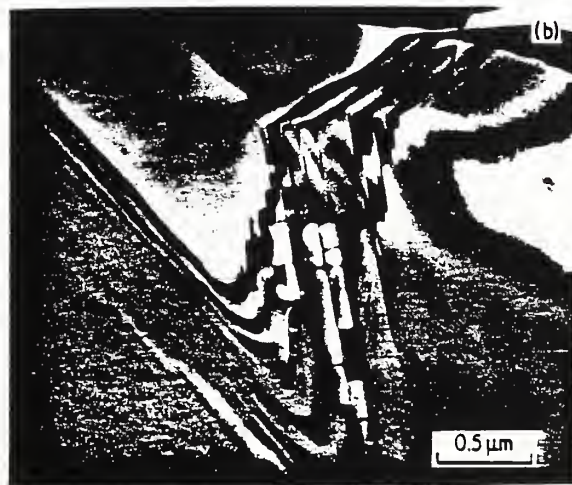


Figure 6 (a) SEM illustrating cavitation at grain boundaries and triple junctions in vicinity of developing creep crack on tensile surface. (b) TEM showing plate-like cavities at inclined grain boundary after creep deformation. Formation and growth of such cavities is considered responsible for intergranular creep crack extension.

[†]The thermodynamics of devitrification of grain boundaries has been discussed recently in some detail by Raj and Lange [12].

[‡]While cavity-like holes were often found within multi-grain junctions even in thick regions of TEM samples, they were similarly present in tested and untested samples and are, therefore, attributed to preferential ion-thinning.

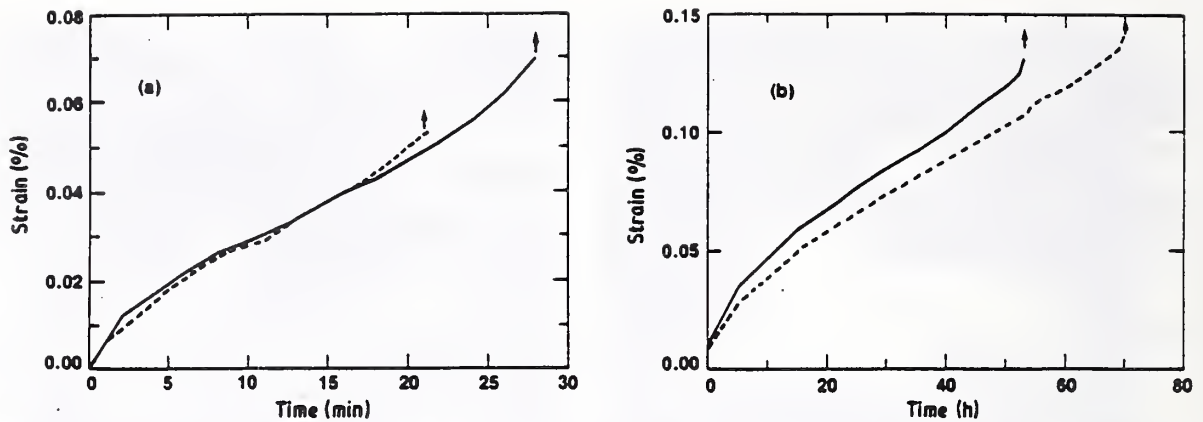


Figure 7 Creep of AD-96 alumina under an applied stress of 60 MPa at 1044°C. (a) No prior annealing. Note that failure occurred within 30 min of initial load application for both specimens. (b) Specimen annealed for 96 h at 1044°C prior to testing. Annealing results in an approximate two hundred-fold increase in specimen lifetime, primarily as a consequence of grain-boundary devitrification.

failure, but the sort of creep-rate enhancement often reported for structural metals does not occur for this ceramic. This slight increase in creep rate is probably due to an increase in specimen compliance resulting from rapid crack growth.

Considerable run-to-run scatter was observed in the failure times for a given test condition, even when specimens were tested simultaneously in the same furnace. Scatter in the failure times by as much as a factor of three was not uncommon. By contrast, the minimum creep rate for a given test condition was relatively constant from run to run. Finally, annealing has an enormous effect on the creep behaviour of this material. The annealing treatment of 96 h at $\sim 1050^\circ\text{C}$ decreased the creep rate and increased the lifetime by a factor of almost 100 (Fig. 7). As will be discussed below, this decrease in the creep rate can be directly attributed to devitrification and to the changes in the volume fraction and the viscosity of the glass at grain boundaries.

The creep data illustrated in Figs. 7 and 8 may be summarized by expressing the minimum strain rate, $\dot{\epsilon}$, as a function of applied stress, σ , and temperature, T :

$$\dot{\epsilon} = A(\sigma/\sigma_0)^n \exp(-\Delta H/RT) \quad (1)$$

where R is the gas constant and A , n and ΔH are empirically determined constants. The constant A has units of h^{-1} and the normalization constant, σ_0 , for the stress has units of MPa. In the present experiment the constants A , n and ΔH were determined by a least-squares fit of Equation 1 to 28 sets of the experimental data. The values of these constants and their standard deviations are $\ln A = 53.6 \pm 5.0$; $n = 4.85 \pm 0.45$; $\Delta H = 926 \pm 58 \text{ kJ mol}^{-1}$. The standard deviation of the fit was approximately ± 0.45 .

3.3. Creep-rupture behaviour

The creep-rupture data obtained in the present experiments are summarized in Fig. 9, where the logarithm of the minimum creep rate is plotted as a function of the logarithm of the rupture time. As can be seen from this figure, there is a negative correlation between the minimum strain rate and the time to failure. If the failure time is expressed as a power function of the minimum strain rate, then the data shown in Fig. 9 can be expressed by the following equation:

$$t\dot{\epsilon}^n = b \quad (2)$$

where the constants and their standard deviations,

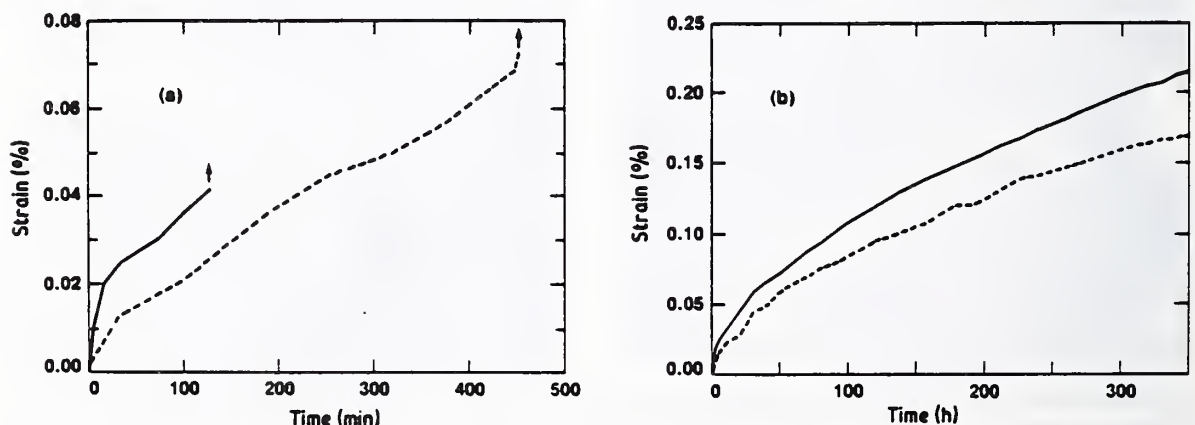


Figure 8 Comparison of short- and long-term creep of AD-96 alumina at 1044°C: initial applied load (a) 80 MPa, (b) 40 MPa. In neither creep measurement could a distinct steady-state region be identified. This is particularly true for the long term runs (b), which suggest continual work-hardening. The upper curve in (b) was in an advanced state of fracture and yet gave no indication of Stage 3 behaviour. In the other creep curves of Figs. 7 and 8, the initial and final stages of creep tend to overlap.

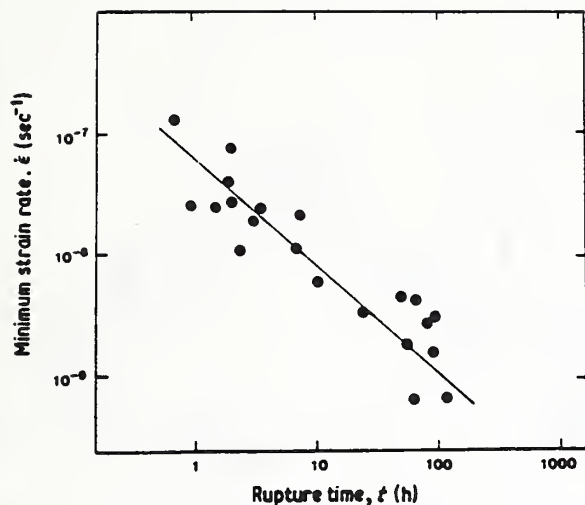


Figure 9 Creep-rupture data fitted to a Monkman-Grant type of plot for AD-96 aluminium oxide.

$a = 1.10 \pm 0.11$ and $\ln b = -8.97 \pm 0.13$, were obtained by a linear regression analysis of $\ln t$ upon $\ln \dot{\epsilon}$ for 21 sets of data. The standard deviation of the fit was approximately 0.72. Equation 2 is the Monkman-Grant [17] equation, first used to describe the creep of metals. The exponent, a , in this equation is not significantly different from 1, the value usually used to describe creep.

The variance of the data about the regression line in Fig. 9 can be reduced significantly if temperature and/or applied stress are introduced as variables. This is illustrated in Fig. 10 where the data from Fig. 9 have been replotted and identified as either constant temperature (Fig. 10a) or constant stress (Fig. 10b) data. In both representations, the data are observed to be layered: the points lie on straight lines of either constant temperature or constant stress. Furthermore, it can be seen that the scatter of the data about the lines, in either representation, appears to be less than that given by the Monkman-Grant relation, indicating the importance of temperature and stress as experimental variables.

The introduction of temperature and applied stress into the analysis can be quantified by assuming that the creep rupture data fit an empirical equation of the following type:

$$t\dot{\epsilon}^a = B\sigma^m \exp(-\Delta H'/RT) \quad (3)$$

TABLE III Summary of creep-rupture data*

$\ln B$	a	m	$\Delta H'$ (kJ mol ⁻¹)	Standard deviation of fit	Degrees of freedom
-7.95 (0.16) [†]	1 (assumed)	0 (assumed)	0 (assumed)	0.71	20
-8.97 (0.13)	1.1 (0.1)	0 (assumed)	0 (assumed)	0.72	19
-7.6 (3.6)	1 (assumed)	-4.2 (0.56)	195 (54.0)	0.334	18
-8.0 (7.9)	1.0 (0.1)	-4.2 (0.94)	200 (141.3)	0.344	17

*Data fitted to the logarithmic form of Equation 3: $\ln t = \ln B - a \ln \dot{\epsilon} + m \ln \sigma - \Delta H'/RT$.

[†]Standard deviation given in parentheses.

By taking the natural logarithm of both sides of the above equation, the equation can be linearized and the constants a , B , m and $\Delta H'$ can be determined by a linear regression analysis of the data. The results of this analysis are given in Table III. A large and significant dependence of $t\dot{\epsilon}$ on applied stress and temperature indicates that some of the variance in Fig. 9 can be attributed to a variation in these two parameters. In fact, the standard deviation of the fit, ± 0.34 , is reduced by a factor of approximately one-half by taking temperature and stress into account.

3.4. Strain at failure

Another relationship that can be obtained from the creep-rupture data is that of the maximum strain to failure. In the metals literature, the assumption of a constant maximum strain to failure is often used as a criterion for failure [18]. The unmodified Monkman-Grant relation of Equation 2, for example, is essentially a constant strain to failure criterion. By plotting the strain to failure as a function of other test variables, it should be possible to provide additional data for comparing creep and creep-rupture data with theory.

In Fig. 11, the total strain to failure is plotted as a function of the applied stress.[§] Although the scatter of the data is considerable, the figure suggests a negative correlation between these two variables, so that as the stress applied to the specimen is decreased the failure strain is observed to increase. This correlation is supported by data collected on two other specimens loaded at 40 MPa and 1044°C for a period of 350 h. Although they did not fail, the strains on the specimens at the time the tests were discontinued were 0.17 and 0.21%, which were greater than any of the failure strains indicated in Fig. 11. Similar observations were made by Clarke [16], who also noted that failure shown in compressive creep correlated inversely with applied stress.

4. Discussion

4.1. Grain-boundary viscosity

In the temperature range used in the present investigation, all but a few high-silica glasses behave as viscous liquids. Therefore, the glasses at grain boundaries in the present study are also most likely to be liquid, and liquid-enhanced creep undoubtedly dominates the creep results presented in this paper. In all of the theories developed to describe the effect of inter-

[§]The total strain at failure includes that determined from the minimum creep rate ($t\dot{\epsilon}$) and that determined from the transient portion of the creep curve. The total strain ranged from ~ 1.5 to $\sim 2.5 t\dot{\epsilon}$.

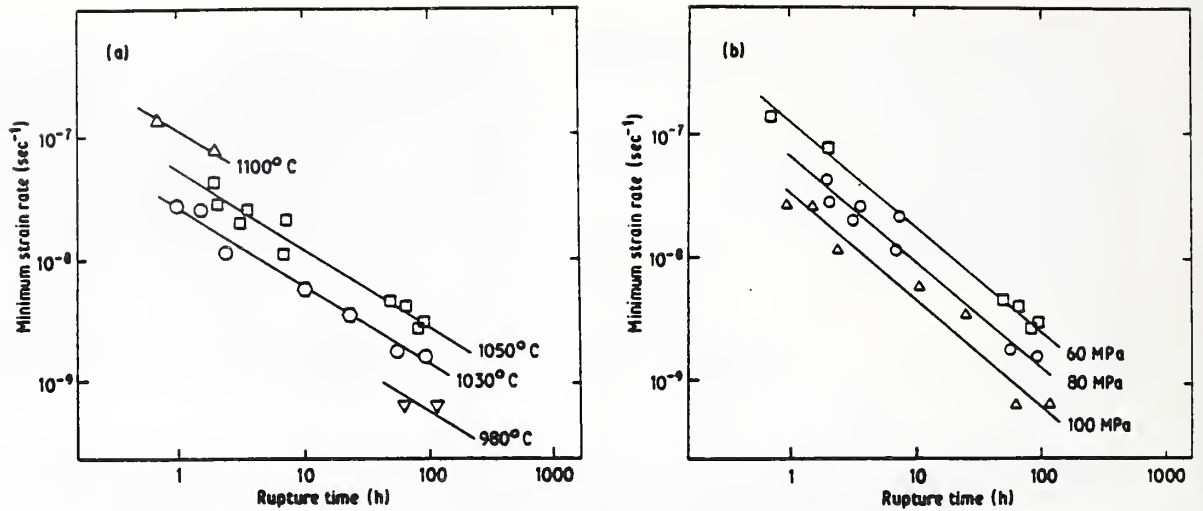


Figure 10 Creep-rupture data for AD-96 plotted as in Fig. 9, but identifying points of either (a) constant temperature, or (b) constant applied stress; (∇) 980°C, (\circ) 1000°C, (\circ) 1030°C, (\square) 1050°C, (Δ) 1100°C.

granular liquids on creep deformation, the viscosity of the liquid is an important variable which should be evaluated to fully understand the creep process. Therefore, in this section the viscosity of the intergranular glass is calculated from its composition. In the next section, these calculated viscosities are used to evaluate mechanisms of creep.

The viscosities of the vitreous grain-boundary phases were estimated from the compositions given in Table III, by using empirical equations developed by Urbain *et al.* [19] for this purpose. These equations were developed from experimental data on a series of calcia-alumina-silica glass melts, and were tested on a number of slags and glasses for which the equations gave values of viscosity that agreed with experimental measurements to within a factor of 5 [20]. The equations were, however, developed for the low viscosity range $< 10^4$ Pa sec, so that agreement between these equations and experimental data is not expected over the entire range of viscosities.

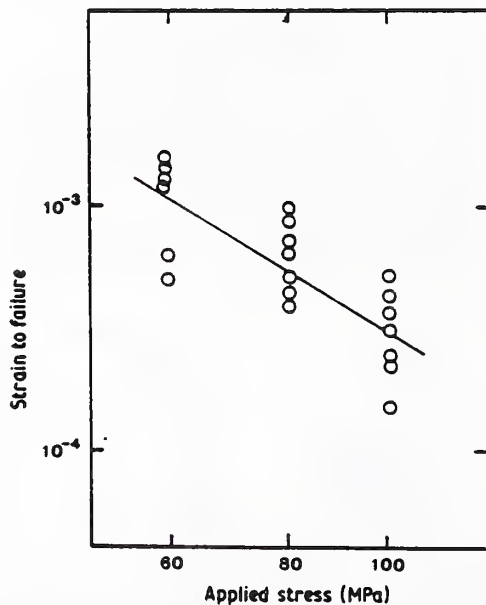


Figure 11 Strain to failure as a function of initial applied stress.

Before using the equations of Urbain *et al.* [19] on the present set of data, the equations were applied to commercial glasses with known compositions and viscosities. The glasses selected for comparison were made by the Corning Glass Works (Houghton Park, Corning, New York) and have the composition indicated in Table I [21]. The calculated and experimental values of the viscosity for C0080 glass, (Fig. 12) agree to within an order of magnitude for the viscosity range 10^{11} Pa sec (530°C) to 10^2 Pa sec (1000°C), which was almost the entire practical range of viscosities for annealing and forming this glass. For C1720 (Fig. 12) an order-of-magnitude agreement between calculated and measured viscosity is obtained for viscosities lying between 10^7 Pa sec (900°C) and 1 Pa sec (1200°C).

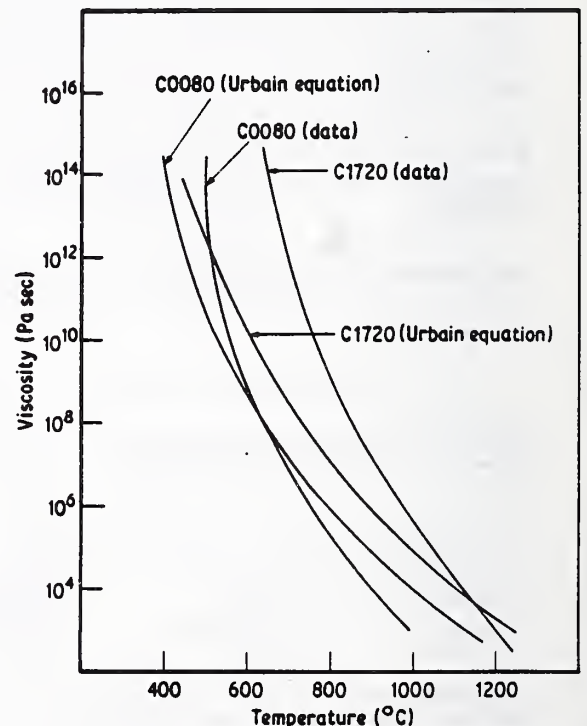


Figure 12 Viscosity of two commercial glasses compared with viscosities calculated from the equations of Urbain *et al.* [19].

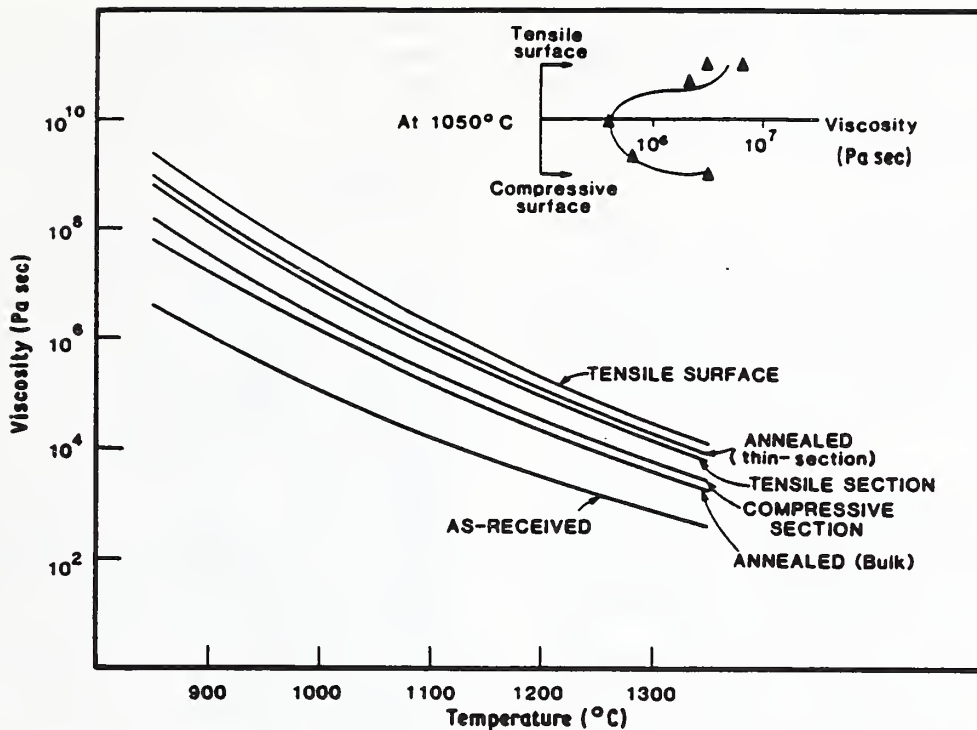


Figure 13 Calculated viscosities of glass composition given in Table III. The insert shows how the glass viscosity changes from the tensile to the compressive cross-section of the bend bars at a temperature of 1044°C.

This agreement between calculated and measured viscosities is considered reasonable for the present study.

The viscosities of the glass compositions given in Table III are shown in Fig. 13. The figure demonstrates the rather sizeable effect of annealing and deformation on the viscosities of these glasses. At any given temperature, changes by a factor of ten in viscosity are observed as a consequence of annealing and creep deformation. This increase in glass viscosity should reduce the creep rate of the annealed specimens by a commensurate amount, because the creep rate is inversely proportional to the viscosity in most theories of creep. Similarly, the additional factor of ~ 10 increase in the glass viscosity in both the tensile and compressive surfaces of the annealed specimens suggests that the surface of the specimens are more resistant to creep than the body of the specimens. This finding raises the possibility of surface embrittlement as a consequence of devitrification during annealing.

The difference in composition of the glass in the tensile and compressive cross-sections suggests a difference in viscosity of the glasses in these cross-sections. Using the formulation of Urbain *et al.* [19], the viscosity of the glass in the tensile cross-section is calculated to be approximately a factor of three greater than that in the compressive cross-section. The presence of crystalline material at the grain boundaries of the tensile cross-section magnifies the viscosity difference even further, so that the effective viscosity of grain boundaries that have been devitrified will be greater than that indicated by the viscosity of the glass alone. Thus, the effective viscosity of the material at the grain boundaries in the tensile cross-section should be more than a factor of three greater than the effective viscosity of the material at the grain boundaries of the compressive cross-section.

These effects of composition on viscosity have interesting implications with regard to the effects of the state of stress on the creep rate. If the effective grain-boundary viscosity were the sole determinant of creep rate, then one would expect tensile specimens to be more creep-resistant than compressive test specimens, for an equivalent temperature and applied stress. In fact, experimental studies on this subject reach the opposite conclusion; creep occurs more easily in tension than in compression [22]. Therefore, while grain-boundary viscosity is important, it is not the only physical or structural parameter determining the creep rate. The overall rheology of the test specimen *vis-à-vis* the state of stress must also be considered. Creep no doubt depends on details of the microstructure such as level of agglomeration, level of homogeneity and amount of direct contact between grains of the microstructure. These effects of microstructure have not yet been considered for ceramic materials. In fact, most theories of creep assume a homogeneous microstructure, an assumption that is clearly not consistent with the structure of most materials investigated. Thus, while intergranular viscosity is probably of paramount importance in determining the creep rate of a component subjected to a particular state of stress, other factors must be considered when the state of stress is a variable.

The effect of devitrification on the creep rate can be quantified by comparing the creep rate of the annealed specimens with that of the as-received specimens. At 1044°C and an initial applied load of 60 MPa, a hundred-fold decrease in the creep rate is observed upon annealing the specimens. Based on most theories of creep, this result suggests a factor of 100 decrease in the effective grain-boundary viscosity. Since the viscosity of the glass at the grain boundaries decreases by

only a factor of ten due to annealing, a change in glass composition alone cannot explain the decrease in creep rate. Crystallization of the grain boundaries effectively increases the average viscosity of the grain-boundary phase by another factor of ten, and in this way decreases the creep rate of the specimens.

4.2. Models of creep

The simplest model of liquid-enhanced creep is that of lubricated flow wherein the grain-boundary glass behaves as a lubricant, reducing the friction between grains. For an applied deviatoric stress $\bar{\sigma}$, the creep rate $\dot{\epsilon}$ is given as a function of grain size d , grain boundary thickness w and viscosity η [23]:

$$\dot{\epsilon} = \alpha \left(\frac{w}{w + d} \right) \left(\frac{\bar{\sigma}}{\eta} \right) \quad (4)$$

where α is a constant having a value of approximately $\frac{1}{3}$. Substituting $\bar{\sigma} = 40$ MPa, $d = 8 \mu\text{m}$, $\eta = 10^6$ Pa sec (the value for the annealed specimen at 1040°C) into Equation 1, we obtain a calculated value of the grain boundary thickness, w , of 1.8×10^{-15} m for a creep rate of $3 \times 10^{-9} \text{sec}^{-1}$ (60 MPa applied stress, 1040°C). This estimated value of w is of course subatomic, indicating that frictional forces at grain boundaries provide almost no impediment to the creep process. Therefore, lubricated flow cannot possibly be an acceptable mechanism for the creep results in the present study. As noted by others [23, 24], lubricated flow is probably never an explanation for liquid-enhanced creep because the mechanism does not take into account the complexity of the microstructure for most materials. Grains that form the microstructure do not lie in ordered planes, as assumed in the model of lubricated flow. When subjected to stress, grains tend to lock up as the solid is deformed, greatly increasing the forces required to maintain a given rate of creep. In this way, the material work-hardens. For flow to continue, i.e. for the grains to slide over one another, an increase in the volume (a dilatation) must occur [25, 26]. Therefore, if liquid lubrication were the only possible process, creep would become more and more difficult as the strain increased and the creep would eventually stop. In fact, creep continues because there are mechanisms of accommodation that relieve the stresses caused by the volume expansion. In the order to be discussed below these mechanisms include (a) fluid flow or percolation, (b) pressure solution or solution precipitation, and (c) grain-boundary cavitation.

Percolation, or fluid flow, was first mentioned as a mechanism of accommodation by Reynolds [25], and later by Frank [26]. The effect of fluid flow on creep was quantified by Drucker [27] and by Lange [24], who calculated the rate of creep resulting from the localized flow of liquid from the compressive to the tensile surfaces of individual grains. The equation developed by Drucker for the strain rate is

$$\dot{\epsilon} = \left(\frac{\sigma}{\eta 3^{1/2}} \right) \left(\frac{w}{d} \right)^3 \quad (5)$$

where σ is the applied tensile or compressive stress.

The model assumes that the grains lie in a two-dimensional hexagonal array and that flow is homogeneous throughout the material. Substituting experimental values of η (10^6 Pa sec), σ (60 MPa) and d ($8 \mu\text{m}$) into this equation yields the following relation between $\dot{\epsilon}$ and w : $\dot{\epsilon}/w^3 = 6.7 \times 10^{16} \text{sec}^{-1} \text{m}^{-3}$, from which a grain-boundary thickness of 3.5 nm is calculated for a creep rate of $3 \times 10^{-9} \text{sec}^{-1}$ at 1044°C . This value of the grain-boundary thickness lies at the lower end of the range normally observed for glass-bonded aluminum oxide, which suggests that a significant resistance to fluid flow only occurs along the narrowest boundaries of the composite. During deformation, glass flows easily from pores or external surfaces along triple junctions and therefore wide grain boundaries offer little resistance to fluid flow. By contrast fluid flow along narrow grain boundaries is difficult, so that the local stresses will be greatest along these boundaries. Because of these preferred paths for fluid flow, deformation of polyphase materials is most likely non-homogeneous. Devitrification increases the difficulty of fluid flow by increasing the effective grain-boundary viscosity by a factor of approximately ten over that calculated for the glass in the annealed specimens. This increase in viscosity should increase the estimate of the grain-boundary thickness by a factor of approximately two.

Turning now to solution precipitation as a means of liquid-enhanced creep, two types of mechanism have been suggested. In one, the grains of the solid are in firm contact and the driving forces for solution and precipitation result from the high stress that occurs at contact points [23, 28, 29]. The creep rate can then be limited either by the kinetics of solution and precipitation, or by the rate of transport from regions of high to regions of low stress, the transport processes being driven by the gradient of the chemical potential and its dependence on pressure. These mechanisms were discounted in the present experiments because no evidence of intergranular contact was found in microstructural analyses of deformed specimens. If contact sites were present they would appear as well-defined regions of strain contrast, as has been reported by Lange *et al.* [30] in TEM studies of hot-pressed silicon nitride. Similar patterns of strain contrast due to intergranular contact have been observed in hot-pressed silicon nitride in our own laboratory [31]. In the glass-bonded aluminum oxide, however, no such strain contrast was observed at grain boundaries in the present study. Therefore, either the contact sites were not there, or they were so widely spaced that their observation would have been rare. In this section we assume that the grains were not in contact, and that each grain of solid was completely surrounded by glass.

When glass forms a continuous phase around the grains, then stress gradients within the glass result from the high viscosity of the glass, which resists the imposed forces and prevents the grains from touching. Solution reprecipitation for this situation has been analysed by a number of investigators [32–35], and creep equations similar to the following one by Rutter [34] have been reported for transport limited processes:

$$\dot{\epsilon} = \frac{32\sigma VC_0 Dw}{N_0 k T \rho d^3} \quad (6)$$

where V is the molar volume of the solid (Al_2O_3), C_0 is the concentration (mass vol^{-1}) of the diffusing species in the solution, D is the diffusivity, N_0 is Avogadro's constant, k is Boltzmann's constant and ρ is the density of the solid.

In our treatment of creep by solution precipitation, the diffusivity must be estimated in order to evaluate the creep rate. Usually, the Stokes–Einstein relation ($D = kT/6\eta r$) is used in solution precipitation theories to estimate the diffusivity in terms of the liquid viscosity, η , and the radius, r , of the diffusing species. Whereas the Stokes–Einstein relation works well for liquid metals and molten salts, problems are encountered in its application to liquids, such as glasses and polymeric melts, that have a network structure [36]. In these structures, most atoms diffuse through the network. By contrast, viscous flow is determined primarily by the structure of the network, i.e. by the breaking of network bonds, so that the two processes may not be closely related, and consequently the errors in estimating the diffusivity can be large [36, 37]. Thus, before using the Stokes–Einstein relation, its potential for error should be recognized and if possible the equation should be assessed on known sets of data.

In the present investigation the transport of aluminum ion, Al^{3+} , probably controls aluminum oxide diffusion, because its rate of diffusion is much less than that of oxygen, O^{2-} , in silicate melts [38, 39]. To test the applicability of the Stokes–Einstein relation to Al^{3+} , experimental parameters for viscosity and diffusivity assembled by Cooper and Kingery [39] were used. At 1400°C the diffusivity of Al^{3+} is $\sim 2.6 \times 10^{-7} \text{cm}^2 \text{sec}^{-1}$, while the viscosity is 23.3 poise (2.33 Pa sec), from which an ionic radius of $\sim 0.02 \text{nm}$ is calculated. This value is about a factor of 2.5 smaller than that (0.05 nm) estimated by Pauling [40] from wave-mechanical considerations. The diffusivity and the viscosity also appear to have similar temperature dependencies ($\Delta H = \sim 272 \text{kJ mol}^{-1}$ for diffusion and $\sim 229 \text{kJ mol}^{-1}$ for viscous flow). Based on this comparison, the Stokes–Einstein relation is expected to give an order-of-magnitude estimate for the diffusivity of Al^{3+} in the temperature range used for the present study.

Substituting the Stokes–Einstein equation into Equation 6, the following relation is obtained for the creep rate:

$$\dot{\epsilon} = \frac{32\sigma VC_0 w}{6N_0 \eta r \rho d^3} \quad (7)$$

Using appropriate experimental values ($V = 25.5 \text{cm}^3 \text{mol}^{-1}$, $C_0 = 0.625 \text{g cm}^{-3}$, $r = 0.02 \text{nm}$, $\rho = 4 \text{g cm}^{-3}$) in Equation 7, the relation between $\dot{\epsilon}$ and w is given by $\dot{\epsilon}/w = 8.7 \times 10^{-2} \text{sec}^{-1}$, from which a grain-boundary thickness of 34 nm is calculated for an initial applied stress of 60 MPa at a temperature of 1044°C . This grain-boundary thickness lies within the range of values observed in the present experiment. In view of the assumptions made in obtaining this number, the

fact that this estimate of grain-boundary thickness is an order of magnitude greater than that for percolation with the same experimental parameters cannot be considered significant. Within the accuracy of the models and the material property estimates, therefore, the solution precipitation and the percolation models of creep must be considered competitive.

Nucleation and growth of cavities within grain boundaries provides a third mechanism by which work-hardening resulting from the dilatant behaviour of the polycrystalline solid can be relieved. Cavitation is commonly observed as a means of accommodation in metals, and has been reported in a number of studies for ceramics tested in tension, bending and compression [3, 5, 13–16, 20]. Since homogeneous cavitation was not observed in the present study it must be concluded that cavity formation and growth did not play a major role during creep deformation. This conclusion is very different from that reached by Clarke [16], who found that high-temperature deformation of glass-bonded alumina was dominated by cavitation within the glass phase. The reasons for the difference between our results and Clarke's are not fully understood at the present time, but may reside in differences in the composition and viscosity of the glasses used in the two studies. Although the two studies were conducted over roughly the same temperature range, the viscosity of the glass bonding phase in Clarke's study was approximately two orders of magnitude less than in our own study. In fact, the viscosity of the glass used by Clarke [16] was similar to that of the glass in the unannealed specimens in our study. Further studies are indicated to clarify the role of cavitation in the creep process, and the conditions under which cavitation occurs in two-phase ceramics.

Although extensive cavity nucleation, of the type reported in the creep-rupture literature, was not observed in the present study, isolated and fairly widely spaced grain-boundary delaminations were observed. The delaminations occurred at the tensile surface where the stresses were highest, and where the surfaces were embrittled by extensive devitrification of glass at the grain boundaries. These delaminations form preferentially at two grain boundaries where, according to percolation theories of creep, the stresses are highest. These delaminations may be precursors of cracks that nucleate in the tensile surface of the specimen and grow to a critical size during the course of the creep experiment.

4.3. Creep and creep-rupture phenomenology

Although the initial purpose of this study was to estimate the creep behaviour of a two-phase ceramic from an analysis of the microstructure of the ceramic, the extensive collection of creep and creep-rupture data presented in this paper warrants some brief comment on the data and its comparison with other data of the same type. In this section, discussion is limited to vitreous-bonded oxides including refractories, porcelain and glass–ceramics, which are closest in structure to the material used in the present study.

4.3.1. Stress exponent

In the present paper the classical power-law creep expression given by Equation 1 was fitted to the creep data. Both the power-law exponent, $n = 4.85$, and the apparent activation enthalpy, $\Delta H = 926 \text{ kJ mol}^{-1}$, lie at the high end of values reported for creep processes. Literature values of n range from ~ 1 to 6 depending on the material tested and the level of stress [6, 7, 22, 41, 42]. The value of n tends to increase as the stress is increased, but does not appear to depend on the sign of the applied stress, i.e. whether the applied stress is tensile or compressive [20]. In view of these comments, the value of n obtained in the present experiments is not unusual, even though it lies at the high end of the range of values.

Since most theories of creep are linear in applied stress ($n = 1$) they cannot be used in unaltered form to explain non-linear aspects of creep or creep rupture. Most often, investigators have suggested cavitation or microcrack formation as the primary explanation for a high creep exponent [3, 22]. As cavities are formed the applied stress is transferred from the cavitated to the uncavitated portion of the specimen, and the creep rate increases as a result of both cavity nucleation and cavity growth. Since the rate of nucleation and growth of cavities is basically a non-linear function of applied stress [14], the creep process is also a non-linear function of stress. Thus, Moreel and Ashbee [22], Lange *et al.* [3], Clarke [16] and others have used cavitation as a means of explaining the non-linear dependence of creep on stress.

In the present experiments, no evidence of cavitation at grain boundaries was obtained, and therefore it is difficult to explain the non-linear creep behaviour by cavitation. Instead other time-dependent processes such as devitrification and premature termination of the creep process by fracture are probably responsible for the observations. The importance of crystallization or devitrification was first noted by Norton [6] in a study of the tensile creep of porcelain. Devitrification increases the effective viscosity of the grain-boundary phase and hence increases the resistance of a two-phase material to creep deformation. Norton [6] noted that when crystallization has sufficient time to occur, as when the applied loads are low, then the changes in the microstructure increase the amount of work-hardening and reduce the apparent steady state creep rate. The converse is true at high loads, when creep is rapid and devitrification does not have sufficient time to occur. In this case, the apparent steady state creep rate is higher than would be determined from a linear dependence of creep rate on applied load.

In addition to the structural effects discussed above, premature termination of the creep process by specimen fracture can also play a role in establishing a high value of the creep exponent n . When crack nucleation and crack growth are strongly dependent on the applied stress, then the time to failure may depend on the applied stress in a way that is independent of the creep process. At high levels of applied load, failure is likely to occur in an early stage (i.e. Stage 1) of the creep process, so that the creep rate will be greater

than that obtained if creep were not interrupted by fracture. By contrast, failure at low levels of applied stress is likely to occur much later in the creep process (i.e. Stage 2) so that the two measured creep rates will not correspond to the same portion of the creep curve. The net effect of representing such a set of data by Equation 1 is to obtain a non-linear dependence of creep rate on applied stress.

In the present experiments both devitrification and premature specimen failure played a role in establishing the high value of n . Creep occurs initially in a "crack-free" condition; the specimen deforms, work-hardens, and then at some point in time grain-boundary delamination results in crack formation and eventually in specimen failure. The minimum creep rate achieved during each run depends both on the devitrification process, and on the crack nucleation and growth process, both of which lead to a non-linear dependence of the creep rate on applied stress.

4.3.2. Apparent activation enthalpy

Based on the discussions in Sections 4.1 and 4.2, the temperature dependence of the creep rate might be expected to be determined primarily by the glass viscosity, and the dependence of the glass viscosity on composition. For the glass compositions given in Table II, the apparent activation enthalpy for viscous flow is estimated to be $\sim 330 \text{ kJ mol}^{-1}$. This estimate can be increased somewhat by taking into account changes in glass composition that result from changes in temperature. The magnitude of this effect is inferred from the net change in composition due to annealing. From Fig. 13, annealing results in approximately two orders of magnitude increase in viscosity, which should increase the estimated value of the apparent activation enthalpy for viscous flow from ~ 330 to $\sim 550 \text{ kJ mol}^{-1}$, a value that is clearly not enough to explain the high apparent activation enthalpy, 926 kJ mol^{-1} , for creep in the present experiment.

This lack of agreement between the estimated and measured activation enthalpies clearly indicates that factors other than glass viscosity play a role in establishing the temperature dependence of the creep process. Grain-boundary devitrification may be one such factor, since it is known to occur during creep and should have a dramatic influence on the effective viscosity of the grain boundaries. If grain-boundary devitrification is important, then the enthalpy of solution of grain-boundary phases will contribute to the apparent activation enthalpy of the creep process. The importance of the heat of solution in the creep process has been suggested by Raj and Morgan [43] for a number of high-temperature processes in hot-pressed silicon nitride, and has been applied by Wang and Raj [44] to explain the high activation energies ($\sim 700 \text{ kJ mol}^{-1}$) for the creep of glass-ceramics. The heat of solution is also important when solution precipitation occurs during creep. Further studies will be required to fully elucidate the importance of grain-boundary devitrification in the creep of multiphase ceramics.

4.3.3. Creep rupture

The creep-rupture data shown in Figs. 10 and 11 were found to fit the modified Monkman-Grant relation given by Equation 3. This equation was selected to represent the creep-rupture data because theoretical work by Evans and Blumenthal [45, 46] have been represented in this format. Furthermore, the creep-rupture experiments presented by Johnson *et al.* [47] on direct-bonded aluminum oxide have been shown to fit this type of equation. In this regard, it may be significant that the stress exponent of $t\dot{\epsilon}$ obtained by Johnson *et al.* [47], -6 ± 2 , is close to the value obtained in our own experiments, -4.2 ± 0.9 , despite the great difference in the microstructures of the two materials.

Most theories that have been developed to describe the creep rupture of polycrystalline systems assume a rather simple microstructure. For two-phase ceramics, the microstructure is usually viewed as a collection of equiaxed grains separated by a viscous fluid [14, 45, 48]. For this type of material, models of crack nucleation, crack coalescence and crack growth have been developed. Generally, these predict a small dependence of $t\dot{\epsilon}$ on applied stress. To be more specific, $t\dot{\epsilon}$ for nucleation-controlled creep rupture is predicted to be stress-independent. In view of this prediction, crack nucleation cannot be considered rate-limiting in the present study. For crack-growth controlled fracture, $t\dot{\epsilon}$ is proportional to σ^{n-p} , where n is the stress exponent for creep and p is the stress exponent for crack growth.* From theoretical considerations, Tsai and Raj [48] suggest $p \leq 4$ for crack propagation in two-phase materials. Combining $p = 4$ with the value $n = 4.85$ measured in the present paper yields a value for the stress exponent of $t\dot{\epsilon}$, 0.85, which is not consistent with the experimental results of the present paper. Thus, crack growth alone cannot be used to rationalize the present set of creep-rupture data. The remaining theory of creep rupture, the coalescence theory, is not sufficiently developed to be compared with the present set of data [51].

From the above discussion we must conclude that the theories of two-phase creep fracture that have been developed to date are not able to explain the stress dependence of $t\dot{\epsilon}$ for the current set of data. In view of the complexity of the material used in the present investigation, this finding is not, perhaps, surprising. Alteration of the material by stress-dependent devitrification undoubtedly plays a role in both the nucleation and crack-growth processes. Additional theoretical work is clearly needed to model the effect of devitrification on crack growth and crack nucleation. In addition, microscopic studies will be needed to elucidate the importance of nucleation and of subcritical crack growth to the failure process.

5. Summary

This paper presents the results of an investigation of the creep and creep rupture of a commercial grade of glass-bonded aluminum oxide. Analytical electron

microscopy was used to evaluate the chemical composition of glass at the grain boundaries, and the variation of the composition of the glass with exposure to elevated temperature and creep deformation. The type and degree of devitrification that occurred during creep clearly appeared to be stress-dependent. The glass at grain boundaries in the tensile cross-section of the test specimens was approximately three times as viscous as the glass in the compressive section of the test specimen. This finding is consistent with the pattern of devitrification observed in these specimens. Devitrification was greatest at the tensile surface, which suggests an embrittlement of the surface compared with the rest of the specimen cross-section.

The viscosity of the glass at the grain boundaries was estimated from its chemical composition and was used to compare the measured creep rates in the present study with models that have been developed to describe creep in two-phase ceramics. The creep mechanisms that most closely represent our results are the viscous flow (percolation) mechanism and the solute precipitation mechanism, both of which were suggested by a number of authors. Cavitation was discounted because of the lack of evidence for homogeneous cavitation in the tensile portions of the bend specimens. During later stages of creep, however, grain-boundary delaminations were observed at the tensile surfaces and are probably the origins of cracks that are eventually responsible for the failure of these specimens. Additional studies were recommended to clarify the relative importance of crack nucleation and crack growth to the creep-rupture process.

Acknowledgements

This work was jointly supported by the Department of Energy (Fossil Energy Program) and by the Department of Defense (Air Force Office of Scientific Research).

References

1. E. M. LENOE, R. N. KATZ and J. J. BURKE, (eds.), "Ceramics for High-Performance Applications III, Reliability" (Plenum Press, New York, 1983).
2. Proceedings of the Educational Symposium on Refractories in Slagging Environments, published in *Ceram. Eng. Sci. Proc.* 2(11-12) (1981).
3. F. F. LANGE, B. I. DAVIS and D. R. CLARKE, *J. Mater. Sci.* 15 (1980) 601.
4. *Idem, ibid.* 15 (1980) 616.
5. R. KOSSOWSKY, D. G. MILLER and E. S. DIAZ, *ibid.* 10 (1975) 983.
6. F. H. NORTON, *J. Amer. Ceram. Soc.* 19(5) (1936) 129.
7. C. D. HULSE and J. A. PASK, *ibid.* 49(6) (1966) 312.
8. K. JAMES and K. H. G. ASHBEE, *Prog. Mater. Sci.* 21 (1975) 1.
9. G. W. HOLLENBERG, G. R. TERWILLIGER and R. S. GORDON, *J. Amer. Ceram. Soc.* 54 (1971) 196.
10. G. QUINN and R. KATZ, *Amer. Ceram. Soc. Bull.* 57 (1978) 1057.
11. G. CLIFF and G. H. LORIMER, *J. Microsc.* 103 (1975) 203.
12. R. RAJ and F. F. LANGE, *Acta Metall.* 29 (1981) 1993.
13. M. H. LEWIS, B. S. B. KARUNARATNE, J. MERIDITH and C. PICKERING, in "Creep and Frac-

*This relation is obtained by assuming that creep and crack growth are independent processes, so that the time to failure t is given by $t = B\dot{\epsilon}^{-1}\sigma^{-p}$ [49] and the creep rate is given by Equation 1. By combining Equation 1 with the equation for t , the relation between $t\dot{\epsilon}$ and σ is obtained. The idea of simultaneous creep and crack growth was first presented by Lange [50].

- ture of Engineering Materials and Structures", edited by B. Whilshire and D. R. J. Owens (Pineridge Press, Swansea, 1981) p. 365.
14. J. E. MARION, A. G. EVANS, M. D. DRORY and D. R. CLARKE, *Acta Metall.* 31 (1983) 1445.
 15. N. J. TIGHE, S. M. WIEDERHORN, T.-J. CHUANG and C. L. McDANIEL, in "Deformation of Ceramic Materials II", Materials Science Research, Vol. 18, edited by R. E. Tressler and R. C. Bradt (Plenum Press, New York, 1984) p. 587.
 16. D. R. CLARKE, *J. Mater. Sci.* 20 (1985) 1321.
 17. F. C. MONKMAN and N. J. GRANT, *Proc. ASTM* 56 (1956) 593.
 18. R. W. HERTZBERG, "Deformation and Fracture Mechanics of Engineering Materials", (Wiley, New York, 1976) p. 164.
 19. G. URBAIN, F. CAMBIER, M. DELETTER and M. R. ANSEAU, *Trans. J. Br. Ceram. Soc.* 80 (1981) 139.
 20. R. C. STREETER, E. K. DIEHL and H. H. SCHOBERT, *Amer. Chem. Soc. Fuel Div. Repr.* 28(4) (1983) 174.
 21. J. R. HUTCHINS, III and R. V. HARRINGTON, in "Encyclopedia of Chemical Technology", 2nd edn, edited by Kirk and Othmer, Vol. 10, (Wiley, New York, 1966) p. 533.
 22. R. MORRELL and K. H. G. ASHBEE, *J. Mater. Sci.* 8 (1973) 1253.
 23. G. M. PHARR and M. F. ASHBY, *Acta Metall.* 31 (1983) 129.
 24. F. F. LANGE, in "Deformation of Ceramic Materials", edited by R. C. Bradt and R. E. Tressler (Plenum Press, New York, 1975) p. 361.
 25. O. REYNOLDS, *Phil. Mag.* 20 (1885) 469.
 26. F. C. FRANK, *Rev. Geophys.* 3 (1965) 485.
 27. D. C. DRUCKER, in "High Strength Materials", edited by V. F. Zackay (Wiley, New York, 1965) p. 795.
 28. R. RAJ, *J. Geophys. Res.* 87 (1982) 4731.
 29. R. RAJ and C. K. CHYUNG, *Acta Metall.* 29 (1981) 158.
 30. F. F. LANGE, D. R. CLARKE and B. I. DAVIS, *J. Mater. Sci.* 15 (1980) 611.
 31. N. J. TIGHE, unpublished data.
 32. D. W. DURNEY, *Nature* 235 (1972) 315.
 33. *Idem*, *Phil. Trans. R. Soc. A283* (1976) 229.
 34. E. H. RUTTER, *ibid.* A283 (1976) 203.
 35. R. L. STOCKER and M. F. ASHBY, *Rev. Geophys. Space Phys.* 11 (1973) 391.
 36. E. T. TURKDOGAN, "Physicochemical Properties of Molten Slags and Glasses" (The Metals Society, London, 1983).
 37. R. H. DOREMUS, in "Modern Aspects of the Vitreous State", Vol. 2, edited by J. D. Mackenzie, (Butterworths, London, 1962) p. 1.
 38. R. TERAJ and R. HAYANIC, *J. Non-Cryst. Solids* 18 (1975) 217.
 39. A. R. COOPER, Jr. and W. D. KINGERY, *J. Amer. Ceram. Soc.* 47(1) (1964) 37.
 40. L. PAULING, "Nature of the Chemical Bond", 3rd edn. (Cornell University Press, Ithaca, 1960) p. 514.
 41. F. H. CLEWS, H. M. RICHARDSON and A. T. GREEN, *Trans. Br. Ceram. Soc.* 15 (1945) 161.
 42. S. E. BOLD and G. W. GROVES, *J. Mater. Sci.* 13 (1978) 611.
 43. R. RAJ and P. E. D. MORGAN, *J. Amer. Ceram. Soc.* 64 (1981) C-143.
 44. J.-G. WANG and R. RAJ, *ibid.* 67 (1984) 399.
 45. A. G. EVANS and W. BLUMENTHAL, in "Fracture Mechanics of Ceramics", Vol. 6, edited by R. C. Bradt, A. G. Evans, D. P. H. Hasselman and F. F. Lange (Plenum Press, New York, 1983) p. 423.
 46. *Idem*, in "Deformation of Ceramic Materials II", Materials Science Research, Vol. 18, edited by R. E. Tressler and R. C. Bradt (Plenum Press, New York, 1984) p. 487.
 47. S. M. JOHNSON, B. J. DALGLEISH and A. G. EVANS, *J. Amer. Ceram. Soc.* 67 (1984) 759.
 48. R. L. TSAI and R. RAJ, *Acta Metall.* 30 (1982) 1043.
 49. J. E. RITTER, Jr., in "Fracture Mechanics of Ceramics", Vol. 4, edited by R. C. Bradt, D. P. H. Hasselman and F. F. Lange (Plenum Press, New York, 1978) p. 667.
 50. F. F. LANGE, *Int. J. Fract.* 12 (1976) 739.
 51. A. G. EVANS and A. RANA, *Acta Metall.* 28 (1980) 129.

Received 25 March
and accepted 22 April 1985

NUCLEATION AND GROWTH OF CRACKS IN VITREOUS BONDED ALUMINUM OXIDE
AT ELEVATED TEMPERATURES

K. Jakus
University of Massachusetts
Amherst, MA

S.M. Wiederhorn
B.J. Hockey
National Bureau of Standards
Gaithersburg, MD 20899

Abstract

The nucleation and growth of cracks was studied at elevated temperatures on a grade of vitreous-bonded aluminum oxide that contained approximately 8 volume percent glass at the grain boundaries. Cracks were observed to nucleate within the vitreous phase, close to the tensile surface of the flexural test specimens used in these experiments. Crack nucleation occurred at a strain of ≈ 0.08 to 0.12 percent, which corresponded to a crack nucleation time of ≈ 35 percent of the time to failure by creep rupture. Once nucleated, cracks propagated along grain boundaries, as long as the stress for crack propagation was maintained. The crack velocity for cracks that were nucleated by the creep process was found to be linearly proportional to the apparent stress intensity factor, whereas for cracks that were nucleated by indentation, the crack velocity was proportional to the fourth power of the apparent stress intensity factor.

1. Introduction

At the thermal limit of application of most high-temperature structural ceramics, creep deformation often precedes fracture. Because ceramics are not fully ductile even at the highest temperatures, cavities and micro-cracks are generated by the creep process, so that once a material starts to creep, the defects that eventually lead to failure arise as a natural consequence of creep [1]. Crack size and crack growth rate, which are the most important factors controlling lifetime at room temperature, are replaced in importance at elevated temperatures by nucleation, growth, and coalescence of micro-cracks and voids [1]. To develop high temperature techniques of assuring reliability, these events must be incorporated into the method of lifetime prediction.

In this paper, the results of a study to elucidate mechanisms of crack nucleation and crack growth in a commercial grade of vitreous-bonded aluminum oxide are presented. This material was chosen for study to simulate the microstructure of structural ceramics that contain glass at their grain boundaries. The importance of crack nucleation and crack growth to component lifetime is emphasized for this material. Data from this study are compared with data obtained on a commercial grade of hot-pressed aluminum oxide.

2. Experimental Procedure

Experiments were conducted on a grade of vitreous-bonded aluminum oxide (COORS AD-96)¹ that had been used earlier to characterize the creep and fracture behavior of vitreous-bonded materials [2]. The material has a nominal silica content of 4 percent by weight. Glass and porosity are each ≈ 8 percent by volume, and both are located primarily at three grain intersections. The mean grain size was approximately 8 μm , with a range of from approximately 3 to 20 μm .

Test specimens, 3x5x50 mm, were machined from plates that were cut by the manufacturer from a rectangular billet. Following machining, specimens were heat-treated in air at 1050°C for 96 hours to stabilize the microstructure. They were subsequently polished with 3 μm diamond paste on three adjacent sides to permit microscopic detection of cracks that formed during the creep tests. The choice of temperature and duration for the initial heat-treatment was dictated by the results of an earlier study [2] on the microstructure and creep characteristics of this material. In that study, it was found that prolonged high temperature exposure strongly affected the creep behavior of the material. Specifically, heat-treatment caused the creep rate to

decrease and the creep life to increase by two orders of magnitude. The cause of the change in creep behavior was related to the partial crystallization of the glassy intergranular phase.

In the "as-received" material, the grains were separated by a layer of glass that ranged in thickness from approximately 10 nm to approximately 500 nm. This represented only a fraction of the total glass content in the material; the bulk of the intergranular glass was located at three grain intersections, figure 1a. Heat-treatment caused considerable devitrification of the intergranular glass, figure 1b, particularly within the surface region. Based on the results of the earlier study, it was felt that the test duration in the present study was short enough compared to the heat-treatment time that further microstructural changes during the tests were minimal and therefore did not influence crack initiation and growth.

In the creep cracking experiments the test bars were subjected to "dead-weight" loads in four-point bending (40 mm outer, 10 mm inner spans) at nominal temperatures of 1000°C and 1050°C. All studies were conducted in air. At temperature, the material exhibited considerable creep deformation, and eventually failure occurred due to the nucleation and growth of cracks. In order to correlate the extent of creep with the process of crack growth, additional creep tests were made in which the tests were periodically interrupted by cooling the specimens to room temperature under load. Upon each interruption, the permanent deformation of the specimen was measured from the radius of

curvature of the deformed specimens. The accumulated creep strain was calculated from these measurements². In addition, all of the polished surfaces were searched for cracks, to establish the time for crack nucleation, and after nucleation, to measure the crack velocity as a function of crack size. If any cracks were found, their location and size were recorded and the average crack velocity was calculated from the amount of growth between observation periods.

Following the crack size measurements, the specimen was reheated under load to the operating temperature and the creep test was continued for another period of time. This interruption sequence was repeated until either the specimen broke, or the largest crack became comparable to the specimen size. It should be noted that during the creep tests, the loading point deflection was also monitored continuously giving an additional measure of the extent of creep deformation. Creep data (strain rate versus time and time-to-failure) obtained in this way did not differ significantly from those obtained earlier using uninterrupted creep tests [2]. For cracks that were nucleated by creep, the velocities of at least 10 cracks of equal size were used to obtain an average value of the crack velocity. Nucleation was considered to be complete when the cracks reached a size of approximately 3 grain diameters (30 μm) at which point cracks were generally stable and continued to grow, provided a sustained creep load was maintained on the specimen. Occasionally, cracks smaller than $\approx 100 \mu\text{m}$ were observed to heal, probably as a consequence of a localized reduction of the stresses during

creep. Some of the test bars were indented with a diamond pyramidal indenter prior to the start of the test so that the growth rates of indentation cracks could also be studied using the same interruption technique that was used to study the growth of creep nucleated cracks.

3. RESULTS

3.1 Crack Nucleation

Creep deformation of vitreous bonded aluminum oxide eventually results in the nucleation of intergranular cracks at the tensile surface of the specimen, [2]. These cracks gradually grow into the body of the test specimens causing failure. The details of the nucleation and growth process can best be studied by the use of a combination of optical and electron microscopy (TEM and SEM). Based on TEM examination of thin sections taken from various regions of the creep samples, cracks appear to nucleate at grain boundaries near the tensile surface. This is evidenced by the observation of grain boundary delaminations or clusters of voids within two grain junctions near the tensile surface, figure 2. Delaminations such as those shown in figure 2a are not observed at the compressive surface of the specimens, or at large distances from the tensile surface. At later stages of growth, figure 2b, these delaminations enlarge and clearly exhibit a crack-like character. They gradually spread along the tensile surface of the flexural test bars to form the cracks that

eventually lead to failure of the specimen. After failure, examination of the gauge-section of the flexural specimen by optical microscopy reveals many such cracks in various stages of development, figure 3. Some of these cracks had grown almost all the way across the tensile surface and had penetrated deeply into the body of the specimen, figure 3, before fracture occurred elsewhere.

As indicated above, creep nucleated cracks propagate only through the vitreous intergranular phase of the ceramic. The widths of these cracks were less than approximately $1\ \mu\text{m}$, even after considerable growth, figure 4. Of particular interest to the present study is the observation that as creep cracks grew, grain boundary segments of unbroken material remain behind the crack front, figure 5-6, partially binding the surfaces together. For relatively short cracks, less than $\approx 100\ \mu\text{m}$, the crack surfaces are attached by these unbroken segments, or ligaments, at many points along their entire length. Since these connecting segments must be separated by sliding and opening modes of displacement during crack growth, they are believed to retard crack advance by applying a closing force to the crack surfaces.

3.2 Creep Crack Growth

The manner in which cracks nucleated and grew in vitreous bonded aluminum oxide is illustrated in figure 7 for a specimen tested at 1000°C and an applied stress of 80 MPa. After creep for a

period of less than approximately 70 hours, no cracks were observed in the surface of the specimen, suggesting a minimum time for crack nucleation. Somewhere between 70 and 78 hours, cracks nucleated in the specimen and at 78 hours (corresponding to an estimated strain of 0.076 percent) 9 cracks with lengths of 300 μm or less were observed scattered at random within the gauge section of the specimen, figure 7a. With time these cracks grew, and additional cracks were generated, as can be seen by comparing figures 7b and 7c for exposure times of 82.5 and 87.5 hours, respectively. The crack size distributions at these times, figure 8, show that cracks as large as 600 or 700 μm were found in the specimen surface. However, most of the cracks were freshly nucleated and consequently had dimensions of the order of 100 μm or less.

Although the cracks shown in figure 7 are distributed throughout the gauge section, there are regions on the tensile surface that contain no cracks at all. Although this distribution of cracks may be entirely random, it is tempting to suggest that the crack distribution is, in fact, a consequence of heterogeneous deformation within the material. If deformation is much more severe along the boundaries that separate the crack free regions, then it is along these boundaries that stresses are high. As a consequence, nucleation and growth of cracks is expected to occur preferentially along these boundaries. Preferred deformation is also expected to result in microstructural damage, which decreases the resistance of the boundaries to crack growth, making them the preferred paths for fracture in later stages of

the deformation process. Linkage of the small cracks shown in figure 7, may also play a role in the final failure process.

The growth of both creep and indentation nucleated cracks was monitored at a temperature of 1050°C and an applied stress of 60 MPa. Ranging in size from ≈ 70 to ≈ 180 μm , the indentation cracks were formed by the loads given in table 1. As indicated in this table, 70 μm cracks do not seem to propagate when subjected to an applied stress of 60 MPa at 1050°C. By contrast, cracks larger than ≈ 100 μm do propagate under the same conditions. This behavior suggests the existence of a threshold stress for the growth of indentation cracks in this material. By contrast, cracks of an equivalent size, but nucleated by the creep process at the same temperature and stress, exhibited no threshold stress for crack growth. As long as the stress is maintained on the specimen, these cracks continue to grow, with few exceptions, until failure occurs. In figure 9, the crack velocity for both types of cracks is plotted as a function of applied stress intensity factor³. The $v-K_I$ plot determined from the indentation cracks has a slope of approximately 4, whereas the $v-K_I$ plot for the creep nucleated cracks has a slope of only 1. A comparison of the observed crack velocities in figure 9 shows creep cracks growing at a faster rate than indentation cracks for most of the range of applied stress intensity factors. Thus, the two types of cracks exhibit a substantial difference in their response to applied stress.

3.3 Creep Strain for Crack Nucleation

Because the time required for crack nucleation can account for a considerable fraction of the failure time, [3], the strain at which crack nucleation first occurs is a relevant experimental variable for high temperature structural reliability. Creep strain results of this study are summarized in figure 10, which presents creep strain as a function of creep time. For all four sets of data, crack nucleation occurred somewhere between 0.075 and 0.115 percent strain. For the data taken at 60 MPa and 1050°C this strain corresponded to a range of between 15 and 35 hours of creep as indicated on figure 10. These values are approximately one-third of the time required for failure at this applied stress and temperature, i.e. 50 to 90 hours. For the specimen tested at 1000°C and 80 MPa, the points labelled A, B, and C represent the strain of the crack nucleation data given in figure 7. Prior to crack nucleation, the creep curves the creep curves in figure 10 exhibit the characteristic shape of primary creep. In this regime, the creep rate continues to diminish as the material "work hardens." Crack nucleation occurs during the later stages of primary creep, after the apparent creep resistance of the material has increased substantially.

4. DISCUSSION OF RESULTS

4.1 Creep and Nucleation

The results presented above can be best understood in terms of the microstructure of the aluminum oxide selected for study. In principle, creep can occur in this two phase material by deformation of both the aluminum oxide grains, and the intergranular phase. Because of the low temperatures of the experiments relative to those required to deform the aluminum oxide, creep is expected to occur mainly in the intergranular phase of the material, so that the aluminum oxide grains behave as elastic particles in a viscous matrix. This expectation was supported by microstructural analyses of the test specimens. An examination of the aluminum oxide grains by transmission electron microscopy after deformation gave little evidence of dislocation activity within the grains (by comparison with the as received material), suggesting that the aluminum oxide grains did not deform plastically at the temperatures and stresses of investigation. Diffusional processes also do not appear to contribute to the creep process, since the measured creep rate [2] is approximately two orders of magnitude greater than that obtained from a deformation mechanism map on 10 μm aluminum oxide [8] for the same test conditions. By contrast, estimates of the glass viscosity of the intergranular vitreous phase in this material [2], showed the viscosity to be less than approximately 10^7 Pa·s over the entire range of study. Since this viscosity lies close to the softening point ($10^{6.65}$ Pa·s) of the glass, the

glass is expected to deform readily when subjected to applied stresses and to play the dominant role in determining the deformation and fracture behavior of this material. At temperatures $>1000^{\circ}\text{C}$ the crystalline silicate intergranular phases are also expected to be highly ductile relative to the $\alpha\text{-Al}_2\text{O}_3$ granular phase. Thus, at 1000°C and 1050°C , creep in this material is almost exclusively controlled by deformation of the intergranular phase whether vitreous or crystalline.

Crack nucleation and growth in vitreous-bonded materials can be understood in terms of the deformation that occurs in these materials when they undergo creep. As discussed above, creep occurs primarily by deformation of the vitreous intergranular phase of the material, and is relatively easy as long as the grains of the solid do not interlock. However, as the grains begin to interlock, work hardening occurs and the ease of creep decreases as the amount of strain increases. For creep to continue, the grains must slide over one another, causing a localized volume expansion of the material, i.e. a dilation in the vicinity of the deformation [4,5]. This dilation results in large localized stresses between the grains as deformation continues. Dilation is accommodated by the flow of the viscous intergranular phase from grain boundaries and triple junctions where the local pressure is high to boundaries where the pressure is low. Known as percolation, this process of creep is highly non-linear, so that specimens that are subjected to this type of creep also exhibit nonlinear creep behavior [6,7].

Other processes are also activated to assist the deformation. Solution precipitation is one such process, which relieves local stress concentrations by the dissolution and diffusive transport of material from portions of the grain boundaries where the pressure is high to portions on the grain boundary where the pressure is low [9-14]⁴. In the present study, the material dissolved in this process can be the aluminum oxide grains themselves, or the devitrified precipitates in the intergranular phase. Stresses can also be redistributed by microcracking and cavitation in both the compressive and tensile regions of the bend specimens [15-20]. In an earlier study, it was concluded that both solution precipitation and percolation were important processes in the creep of the AD-96. It was also concluded that cavitation and void formation throughout the body of the solid played little role in the deformation process. However, at the tensile surface where localized stresses and dilational strains are probably greatest, grain boundary delamination or void formation probably accounts for the microscopic observations of crack nucleation described in the present paper⁵.

Based on the observations presented here and in reference 2, we conclude that crack nucleation in vitreous-bonded ceramics is a process of cavity formation and growth within the vitreous phase of the material [21,22]. Crack nucleation is driven by the average stress distribution that develops within the bend

specimen as a consequence of creep. When "work hardening" occurs and grains interlock, this average creep stress is magnified, so that the local, internal stresses that cause crack nucleation in the grain boundary phase are larger than the average creep stress.

Once conditions for cavitation have been achieved, voids that nucleate within the vitreous phase are forced to grow between the aluminum oxide grains into crack-like cavities [1, 21, 22]. These cavities eventually extend into the cracks that are the major cause of failure in this material. The results of this paper suggest that cracks do not grow from internally nucleated cavities, or from the 10 μm pores that are present within the material. Instead they nucleate from grain boundaries that are close to or at the specimen surface, which suggests that conditions for crack nucleation are most favorable at the tensile surface. The grain boundaries that cavitate always lie perpendicular to the applied stress, figure 5, and nucleation appears to occur by the recession of the glass into the intergranular space. The fact that devitrification is greater at the tensile surface than in the bulk of the material also assists the process of microcrack initiation by embrittlement of the surface [2].

4.2 Crack Growth

Once cracks have been nucleated, the lifetime of structural components is determined by the time it takes for one of the cracks to reach a critical size. In the present study, two types of cracks were studied, one was introduced by indentation at room temperature, the other was introduced by the creep process. The $v-K_I$ plots for these two types of cracks indicate that the curve for the creep nucleated cracks had a slope of approximately one-quarter that of the curve for the indentation nucleated cracks. Furthermore, at any given value of K_I , the velocity of the creep cracks was greater than that of the indentation cracks. Although the explanation for this difference in behavior is not immediately obvious, it is possible that the damage resulting from the creep process plays an important role in determining the response of crack motion to the applied load. The fact that creep cracks are nucleated by the flow field resulting from the creep, suggests that the microstructural damage and stresses that are generated by this field are responsible for the difference in the crack growth behavior. In effect, after extensive creep, the structure of the ceramic has been modified by the structural damage and, as a consequence, the fracture behavior of the ceramic is also modified by the damage.

The microstructural observations of the crack tip structure and the crack growth data obtained on indentation cracks are consistent with the model of creep crack growth suggested by Tsai and Raj [21], who assumed that the crack opens by a combination

of shear and opening mode failure. Shear ligaments are formed behind the crack tip offering resistance to the crack motion, and these ligaments must be overcome for the crack to continue its motion. The model predicts a $v-K_I$ curve with a slope of 4 in the high velocity range of crack growth data, a value that is close to that obtained in the present study for the growth of indentation cracks. The microstructure of the crack tip is also similar to that assumed by Tsai and Raj and it may well be that this model can be used to explain crack growth data for indentation cracks. The model, however, sheds little light on the crack-growth behavior of creep nucleated cracks.

The threshold for sub-critical crack growth can be calculated from the data in table 1 by assuming that the crack advances by the flow of viscous glass between the grains of aluminum oxide. This threshold is estimated from the condition $G = 2\Gamma$, where G is the strain energy release rate and Γ is the surface tension of the molten glass. Since the indentation cracks were semi-circular, $G=4\sigma^2a/(\pi E)$, where a is the crack radius and E is Young's modulus. For aluminum oxide, $E=380$ GPa, for silica glass, $\Gamma=0.3$ J/m² [23], yielding a threshold stress of 71 MPa for a 70 μm ($a=35$ μm) crack. This stress is slightly greater than the 60 MPa stress applied to the specimen in the present experiment. Hence, crack propagation is not expected for this crack. Using the same approximation, the 100 μm crack is at the fatigue threshold. These findings are consistent with the data discussed in the present paper.

4.3 Comparison with Other Creep-Rupture Studies

Closely related to the data presented in the present paper are the data published by Dalglish et al. [24], Blumenthal and Evans [25] and Johnson et al. [26] on fine grained (2 and 4 μm), hot-pressed aluminum oxide. The material studied by these authors contained no glass at the grain boundaries and thus differed considerably from the vitreous-bonded material studied in the present paper. Studies were conducted by these investigators at temperatures ranging from 1300°C to 1400°C, and failure was characterized by the nucleation of cracks from chemical or microstructural heterogeneities. Crack nucleation was followed by a short period of crack growth that was terminated by crack arrest and crack tip blunting, in which shear bands generated and propagated as side lobes from the tip of the crack [25]. Failure finally occurred by the nucleation and coalescence of cracks along the shear bands of several of the initial blunted cracks resulting in a serrated fracture surface that followed the initial cracks and the shear bands.

Their study also showed that when specimens containing indentation cracks were stressed below the threshold for crack growth, the same kind of shear bands formed around crack tips as were observed for the creep nucleated cracks. Above the threshold, crack propagation occurred along grain boundaries. In contrast to the arrested cracks, cracks remained relatively sharp as they propagated. The tips of these cracks were, in fact, similar in appearance to those reported in the present paper for

vitreous-bonded aluminum oxide. Although the cracks were more open than those of the present study, the same kind of ligament formation was observed behind the crack tip. Finally, they also found that crack growth from creep nucleated cracks occurred at values of K_I that were less than that required for the growth of indentation cracks.

A comparison of the creep behavior of hot-pressed and vitreous-bonded aluminum oxide reveals a number of differences between the two materials. As discussed in an earlier section of the paper, creep deformation in the vitreous-bonded material is not homogeneous. Therefore, crack nucleation depends more on the details of the creep process than on the presence of microstructural or chemical heterogeneities in the material. Once nucleated, cracks in the vitreous material tend to propagate until failure occurs, indicating that nucleation and growth are related processes in the sense that both are driven by the localized stresses arising from the creep. Crack blunting and shear band formation of the type discussed by Blumenthal and Evans [25] are not observed in the vitreous-bonded material. Cracks are narrow, $< 1 \mu\text{m}$, figure 4, and neither blunting, nor shear band formation was observed even when indentation cracks are loaded below the crack growth threshold.

These differences in behavior between the vitreous bonded and hot-pressed material probably result from the fact that higher temperatures were used in the study of the hot-pressed aluminum oxide. At these higher temperatures deformation of aluminum

oxide occurs by a number of mechanisms including: grain boundary sliding, bulk and grain boundary diffusion, and activated slip and climb [8]. Thus, the stresses in the vicinity of crack tips can be relieved by a number of mechanisms, and as a consequence, crack tip blunting can occur. At lower temperatures aluminum oxide grains are expected to remain rigid, so that the blunting of cracks would have to be accommodated only within the intergranular phase by cavitation, viscous flow or by solution reprecipitation. The fact that blunting and shear band formation did not occur indicates that the kinetics of these processes were too slow at the temperature selected for study to accommodate the crack tip stresses. The study by Clarke [20] suggests that microstructural features similar to those observed in hot-pressed aluminum oxide are probable in the vitreous-bonded materials at higher temperatures. Additional studies will be needed to test this point.

Acknowledgement: Support of the Department of Energy, Fossil Energy Program is gratefully acknowledged by S.M.W. and B.J.H.; K.J. is pleased to acknowledge the support of the National Science Foundation.

Footnotes:

1. The use of this material does not constitute endorsement by the National Bureau of Standards.
2. This procedure was different from that used in reference 1, wherein the creep strain was calculated from the load point displacement. Significant differences were obtained between these two measurement procedures.
3. The stress intensity factors used in figure 9 were calculated from the formula for a circular crack of radius a in a uniform stress field of magnitude σ : $K_I = (2/\sqrt{\pi})\sigma\sqrt{a}$. For various reasons [1], these values of the stress intensity factor can only be considered approximate measures of the driving force for fracture.
4. This assumes a positive pressure and a net decrease in volume when solution occurs within the intergranular phase.
5. It is worth emphasizing that the cavitation discussed in this paper does not occur throughout the volume of the material, but only at 2 grain boundaries close to the tensile surface. The discussion of crack nucleation refers only to these near surface cavities or voids.

Figure Captions

1. Intergranular phase in vitreous bonded aluminum oxide (AD-96): (a) In the as-received material, the bonding phase is amorphous consisting of an aluminosilicate glass which also contains calcium, magnesium and potassium as network modifiers; (b) After heating at 1050°C for 96 hours, the bonding phase crystallizes into a number of silicate minerals (see reference 2 for details of the composition and crystal structure of this material).

2. Delamination occurring at grain boundaries as a consequence of stresses resulting from creep at 1050°C: (a) Initiation of cavities in the intergranular phase. The cavities are located between grain boundary facets, and the geometry of the cavities appears to be dictated by the size of the facets and the thickness of the grain boundary; (b) Cavities after propagation. The boundary of the cavity looks much like the cavity boundary in 2(a); the center has opened sufficiently to observe the spacing between the two surfaces.

3. Tensile surface of a flexural test specimen just prior to failure. Cracks have grown almost completely across the tensile surface (middle micrograph) and half-way through the thickness (top and bottom micrographs) of the specimen. The total specimen width (≈ 5 mm), and the total specimen thickness (≈ 3 mm) are shown in this figure.

4. Optical micrograph from cross-section through flexural creep sample (top edge of micrograph corresponds to intersection with tensile surface). Relief polishing reveals distribution of binder phase, M, and Porosity, P, between aluminum oxide grains, A. View also shows portions of creep crack, C, that developed at the tensile surface. Note, crack growth occurs only within the intergranular binder phase; relatively narrow crack opening displacements are maintained.

5. Scanning electron micrograph of surface crack at an early stage of propagation. Note that the crack is not completely open, but is joined across its faces by unbroken ligaments, L, that must also break for crack propagation to proceed.

6. Unbroken ligament joining the surfaces of a creep crack. The dislocations in the aluminum oxide grains are a consequence of surface polishing and do not result from the process of creep. Specimens taken from locations that lie further from the surface show no evidence of dislocations within the alumina grains, see figure 2 for example. This transmission electron micrograph shows the ligament separation occurring by shear deformation.

7. Sequence of fracture and the distribution of cracks formed in the vitreous bonded aluminum oxide as a consequence of creep at 1000°C and 80 MPa applied stress: (a) 78 hours and 0.076 percent strain; (b) 82.5 hours and 0.077 percent strain; (c) 87.5 hours and 0.078 percent strain. Note that some areas within the gauge section are completely free of microcracks, suggesting the absence of plastic deformation in these regions during creep. Also, once cavitation starts, very little extra strain is needed to open a much larger set of cracks: ≈ 0.076 percent strain for crack pattern shown in (a); ≈ 0.078 percent strain for the crack pattern shown in (c).

8. Histogram of crack size distribution established in vitreous bonded aluminum oxide by creep. Note that most of the cracks lay at the small end of the crack size distribution, indicating more recent nucleation and less crack growth.

9. Crack propagation curves for both creep nucleated and indentation nucleated cracks in vitreous bonded aluminum oxide. The slope of the curve for the indentation nucleated cracks is about four times that of the curve for creep nucleated cracks. The standard deviation of the slope was approximately 0.3 for both curves.

10. Creep curves for vitreous bonded aluminum oxide demonstrating the time required for crack nucleation. Note that all curves are still in the primary stage of creep, and that crack nucleation for all runs occurred at between 0.075 and 0.115 percent strain.

Table 1: Crack size (μm) as a function of exposure time at 1050°C and an initial applied stress of 60 MPa.

Indentation Load (N)	Exposure Time (hrs.)			
	0	6.2	12.2	17.6
10	70 \pm 11*	74 \pm 10	81 \pm 18	78 \pm 17
20	101 \pm 17	112 \pm 14	130 \pm 18	365 \pm 200
40	184 \pm 32	227 \pm 23	330 \pm 123	802 \pm 200
Strain (%)	0	0.049	0.062	0.082

* The crack size presented here is the full length of the indentation crack intersecting the tensile surface of the flexure specimen.

REFERENCES

1. A.G. Evans and W. Blumenthal, "High Temperature Failure in Ceramics," pp.423-448 in *Fracture Mechanics of Ceramics*, Vol. 6, Measurements, Transformations and High-Temperature Fracture, R.C. Bradt, A.G. Evans, D.P.H. Hasselman and F.F. Lange, eds. Plenum Press, New York (1985).
2. S.M. Wiederhorn, B.J. Hockey, R.F. Krause, Jr. and K. Jakus, "Creep and Fracture of Vitreous Bonded Aluminum Oxide, *J. Mater. Sci.*, 21, 810-824 (1986).
3. A.G. Evans, "Structural Reliability of Ceramics: A Processing Dependent Phenomenon," *J. Am. Ceram. Soc.* 54, 127-37 (1982).
4. O. Reynolds, "On the Dilatancy of Media Composed of Rigid Particles in Contact. With Experimental Illustrations," *Phil. Mag.* 20, 469-489 (1885).
5. F.C. Frank, "On Dilatancy in Relation to Seismic Sources," *Rev. Geophysics*, 3, 485-503 (1965).
6. D.C. Drucker, "Engineering and Continuum Aspects of High-Strength Materials," pp.795-833 in *High Strength Materials*, V.F. Zackay, ed., John Wiley and Sons, Inc., New York (1965).
7. F.F. Lange, "Non-Elastic Deformation of Polycrystals with a Liquid Boundary Phase," pp.361-381 in *Deformation of Ceramic Materials*, R.C. Bradt and R.E. Tressler, eds. Plenum Press, New York (1972).
8. H. J. Frost and M. F. Ashby, *Deformation-Mechanism Maps: The Plasticity and Creep of Metals and Ceramics*, Pergamon Press, New York (1982).
9. D.W. Durney, "Solution-transfer, and Important Geological Deformation Mechanism," *Nature*, 235, 315-16 (1972).
10. D.W. Durney, "Pressure Solution and Crystallization Deformation," *Phil. Trans. R. Soc.* A283, 229-40 (1976).
11. E.H. Rutter, "The Kinetics of Rock Deformation by Pressure Solution," *Phil. Trans. R. Soc. Lond.* A283, 203-219 (1976).
12. R.L. Stocker and M.F. Ashby, "on the Rheology of the Upper Mantle," *Rev. Geophys. and Space Phys.* 11, 391-421 (1973)
13. R. Raj, "Creep in Polycrystalline Aggregates by Matter Transport Through a Liquid Phase," *J. Geophys. Res.* 87 [B6], 4731-35 (1982).
14. R. Raj and C.K. Chyung, "Solution-Precipitation Creep in Glass Ceramics," *Acta Met.* 29, 159-66 (1981).

15. R. Kossowsky, D. G. Miller and E.S. Diaz, "Tensile and Creep Strengths of Hot-Pressed Si_3N_4 ," J. Mater. Sci. 15, 983-97 (1975).

16. F.F. Lange, B.I. Davis and D.R. Clarke, "Compressive Creep of $\text{Si}_3\text{N}_4\text{MgO}$ Alloys: Pt. 1 Effect of Composition," J. Mater. Sci. 15, 601-10 (1980).

17. M.H. Lewis, B.S.B. Karunaratne, J. Meridith and C. Pickering, pp. 365 in Creep and Fracture of Engineering Materials and Structures, B. Whilshire and D.R.J. Owens, eds. Pineridge Press, Swansea (1981).

18. J.E. Marion, A.G. Evans, M.D. Drory and D.R. Clarke, "High Temperature Failure Initiation in Liquid Phase Sintered Materials," Acta Met. 31, 1445-57 (1983).

19. N.J. Tighe. S.M. Wiederhorn T.-J. Chuang and C.L. McDaniel, "Creep Cavitation and Crack Growth in Silicon Nitride," pp. 587-604 in Deformation of Ceramic Materials II, Materials Science Research, Vol. 18, R.E Tressler and R.C. Bradt, eds. Plenum Press, New York (1984).

20. D.R. Clarke, "High Temperature Deformation of a Polycrystalline Alumina Containing an Intergranular Glass Phase," J. Mater. Sci. 20, 1321-32 (1985).

21. R.L. Tsai and R. Raj., "Creep Fracture in Ceramics containing Small Amounts of a Liquid Phase," Acta Met. 30, 1043-58 (1982).

22. M.D. Drory and A.G. Evans, "Effects of Voids at Three-Grain Junctions on Sintering and Creep Damage," J. Am. Ceram. Soc. 67, 721-7 (1984).

23. W.D. Kingery, H.K. Bowen and D.R. Uhlmann, Introduction to Cermics, 2nd Edition, John Wiley and Sons, New York (1976)

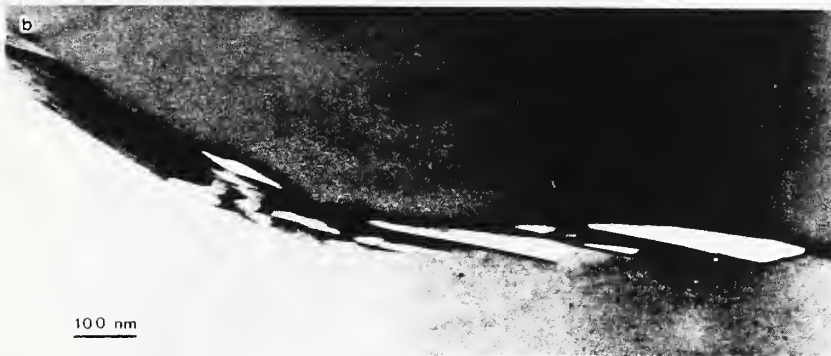
24. B.J. Dalgleish, S.M. Johnson and A.G. Evans, "High-Temperature Failure of Polycrystalline Alumina: I, Crack Nucleation," J. Am. Ceram. Soc. 67, 741-50 (1984).

25. W. Blumenthal and A.G. Evans, "High-Temperature Failure of Polycrystalline Alumina: II, Creep Crack Growth and Blunting," J. Am. Ceram. Soc. 67, 751-59 (1984).

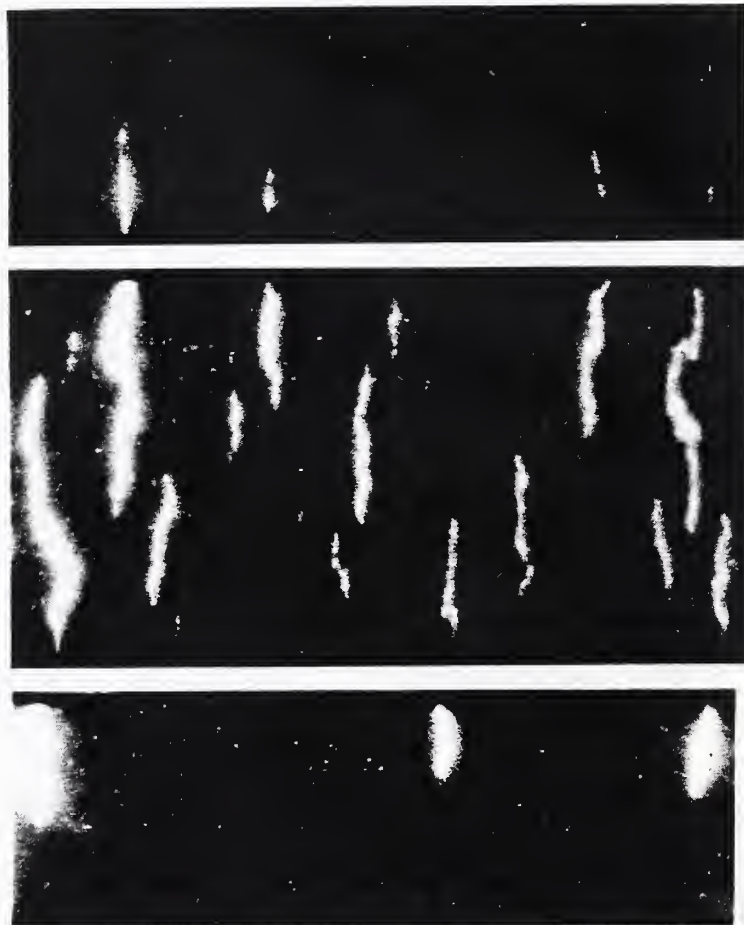
26. S.M. Johnson, B.J. Dalgleish and A.G. Evans, "High-Temperature Failure of Polycrystalline Alumina: III, Failure Times" J. Am. Ceram. Soc. 67, 759-63 (1984).



1. Intergranular phase in vitreous bonded aluminum oxide (AD-96): (a) In the as-received material, the bonding phase is amorphous consisting of an aluminosilicate glass which also contains calcium, magnesium and potassium as network modifiers; (b) After heating at 1050°C for 96 hours, the bonding phase crystallizes into a number of silicate minerals (see reference 2 for details of the composition and crystal structure of this material).



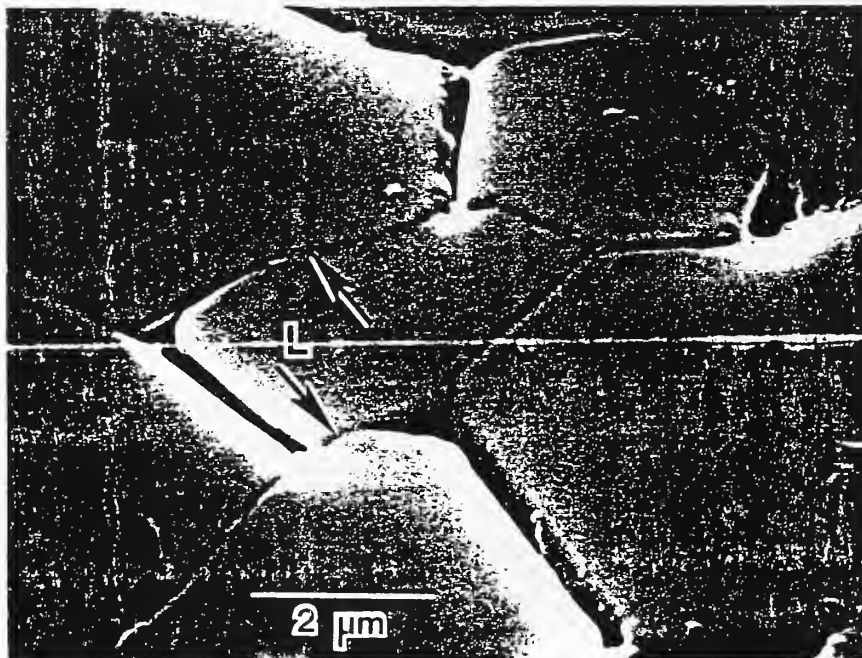
2. Delamination occurring at grain boundaries as a consequence of stresses resulting from creep at 1050°C : (a) Initiation of cavities in the intergranular phase. The cavities are located between grain boundary facets, and the geometry of the cavities appears to be dictated by the size of the facets and the thickness of the grain boundary; (b) Cavities after propagation. The boundary of the cavity looks much like the cavity boundary in 2(a); the center has opened sufficiently to observe the spacing between the two surfaces.



3. Tensile surface of a flexural test specimen just prior to failure. Cracks have grown almost completely across the tensile surface (middle micrograph) and half-way through the thickness (top and bottom micrographs) of the specimen. The total specimen width (≈ 5 mm), and the total specimen thickness (≈ 3 mm) are shown in this figure.



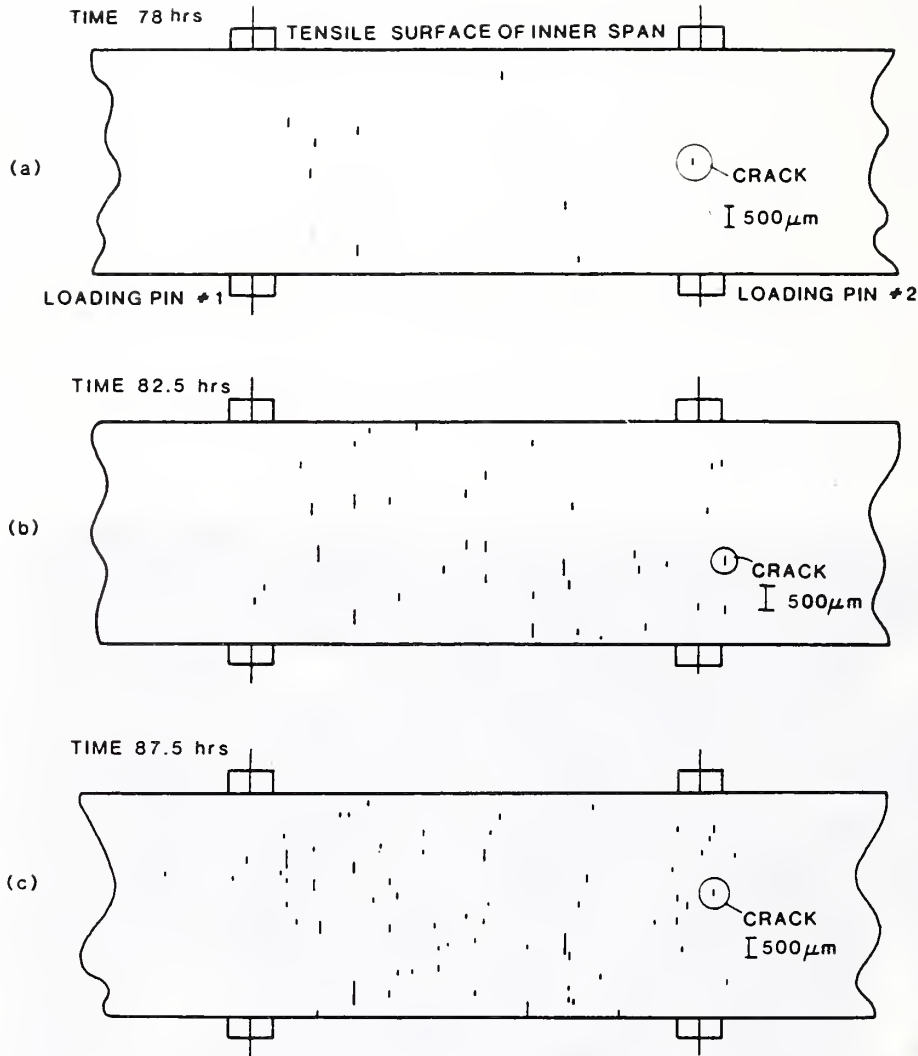
4. Optical micrograph from cross-section through flexural creep sample (top edge of micrograph corresponds to intersection with tensile surface). Relief polishing reveals distribution of binder phase, M, and Porosity, P, between aluminum oxide grains, A. View also shows portions of creep crack, C, that developed at the tensile surface. Note, crack growth occurs only within the intergranular binder phase; relatively narrow crack opening displacements are maintained.



5. Scanning electron micrograph of surface crack at an early stage of propagation. Note that the crack is not completely open, but is joined across its faces by unbroken ligaments, L, that must also break for crack propagation to proceed.

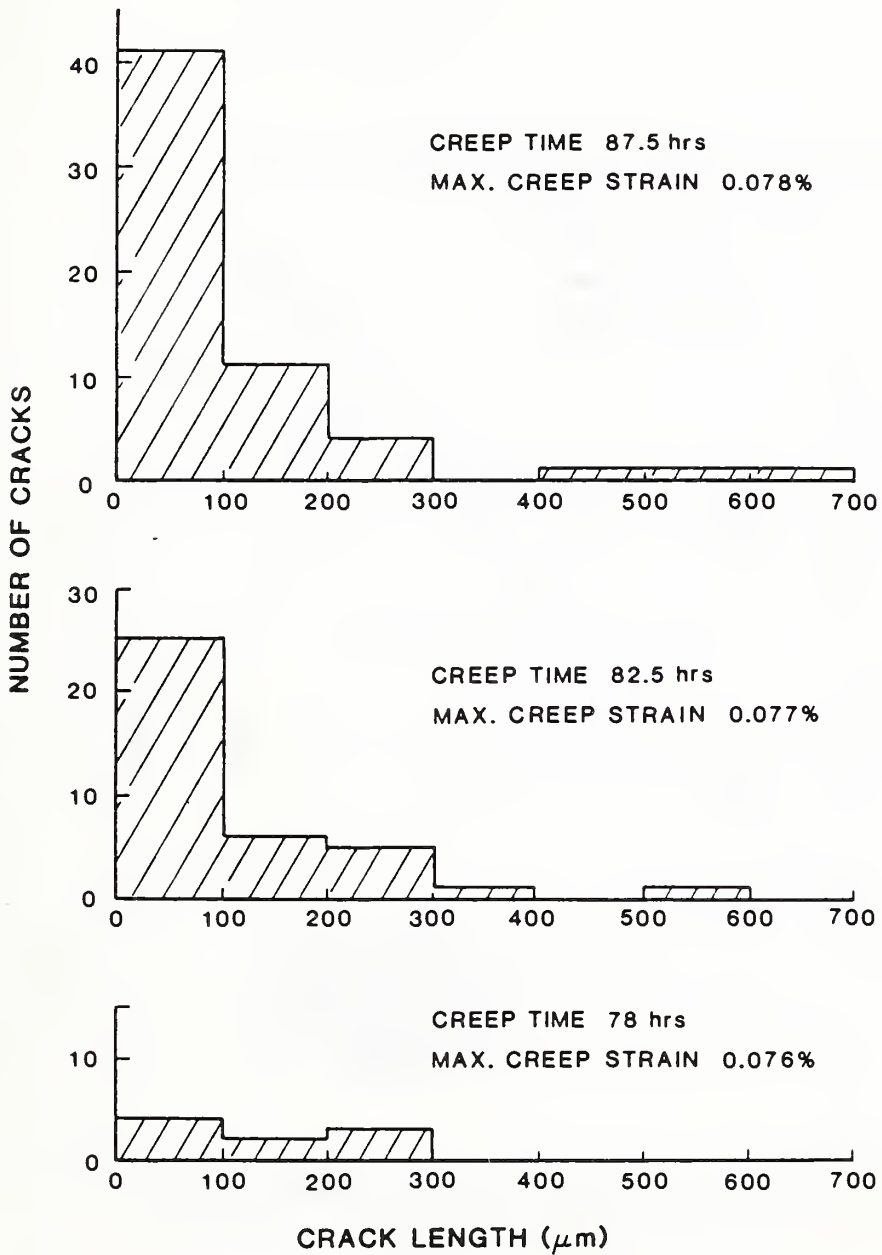


6. Unbroken ligament joining the surfaces of a creep crack. The dislocations in the aluminum oxide grains are a consequence of surface polishing and do not result from the process of creep. Specimens taken from locations that lie further from the surface show no evidence of dislocations within the alumina grains, see figure 2 for example. This transmission electron micrograph shows the ligament separation occurring by shear deformation.

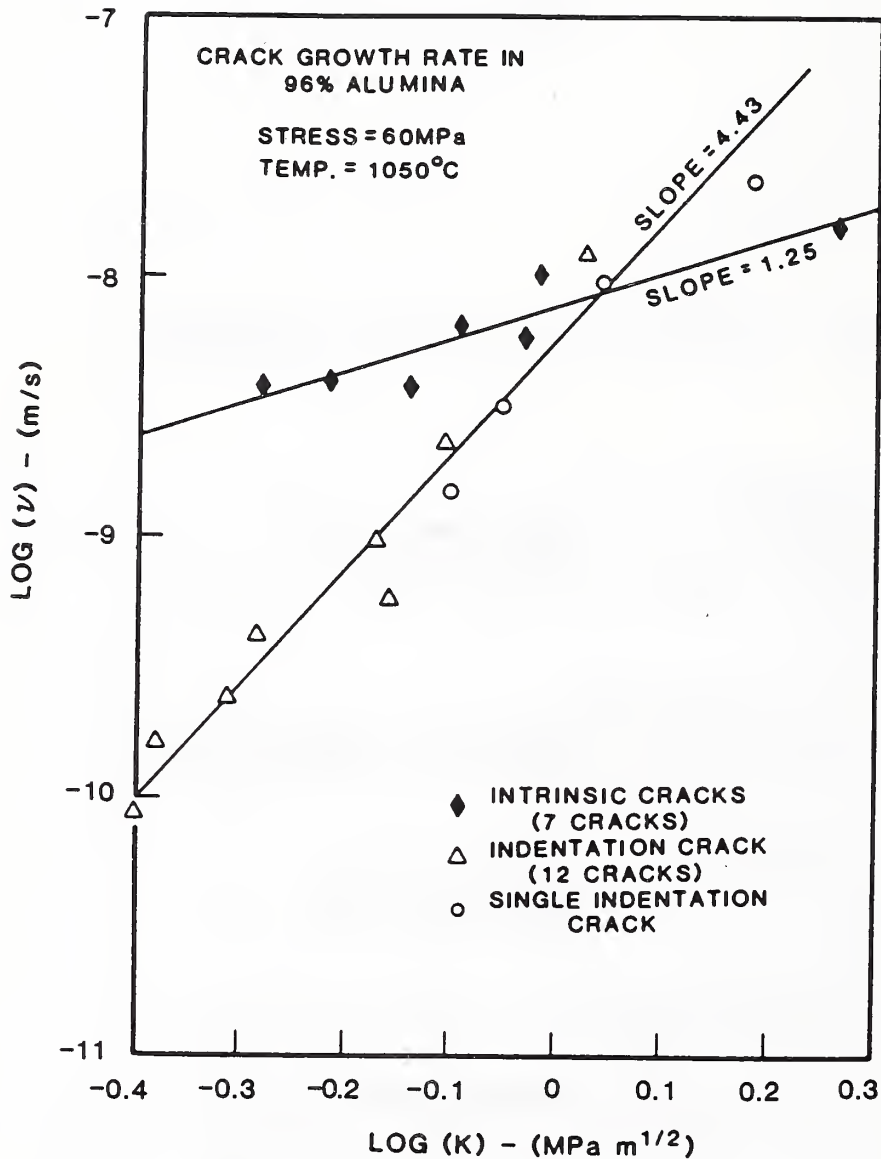


7. Sequence of fracture and the distribution of cracks formed in the vitreous bonded aluminum oxide as a consequence of creep at 1000°C and 80 MPa applied stress: (a) 78 hours and 0.076 percent strain; (b) 82.5 hours and 0.077 percent strain; (c) 87.5 hours and 0.078 percent strain. Note that some areas within the gauge section are completely free of microcracks, suggesting the absence of plastic deformation in these regions during creep. Also, once cavitation starts, very little extra strain is needed to open a much larger set of cracks: ≈ 0.076 percent strain for crack pattern shown in (a); ≈ 0.078 percent strain for the crack pattern shown in (c).

EVOLUTION OF CREEP CRACK DISTRIBUTION IN 96% ALUMINA
(80 MPa/ 1000°C)

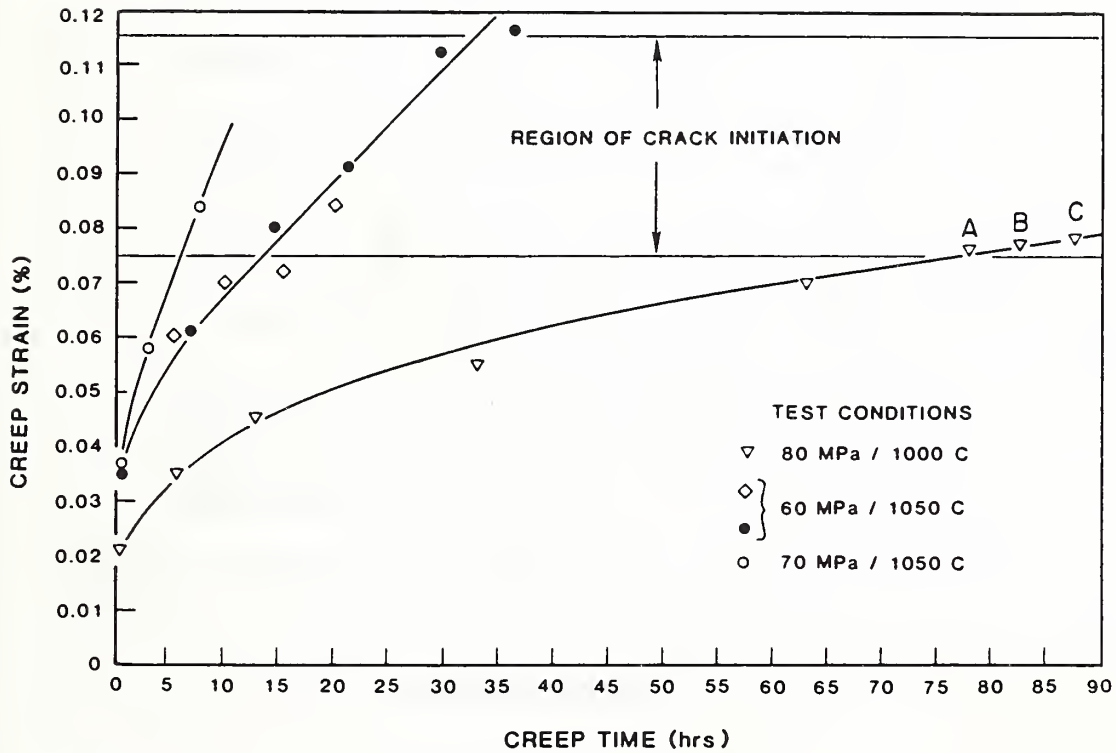


8. Histogram of crack size distribution established in vitreous bonded aluminum oxide by creep. Note that most of the cracks lay at the small end of the crack size distribution, indicating more recent nucleation and less crack growth.



9. Crack propagation curves for both creep nucleated and indentation nucleated cracks in vitreous bonded aluminum oxide. The slope of the curve for the indentation nucleated cracks is about four times that of the curve for creep nucleated cracks. The standard deviation of the slope was approximately 0.3 for both curves.

CREEP STRAIN OF 96% ALUMINA IN 4-PT. BENDING



10. Creep curves for vitreous bonded aluminum oxide demonstrating the time required for crack nucleation. Note that all curves are still in the primary stage of creep, and that crack nucleation for all runs occurred at between 0.075 and 0.115 percent strain.

Rising Fracture Toughness of an Alumina Ceramic
Using the Bending Strength of Indented Specimens

Ralph F. Krause, Jr.
National Bureau of Standards
Gaithersburg, MD 20899

The fracture toughness of a vitreous-bonded 96 percent alumina ceramic was determined to increase as a power function of crack extension. Controlled flaw sizes were produced by Vickers indentation loading between 3 and 300 N and were placed in the center of polished, prospective tensile surfaces of respective four-point bend specimens, previously annealed. The corresponding surface cracks were measured by a shadow technique of optical microscopy. The log of the bending strength was observed to be a linear function of the log of indentation load in two series of experiments: (I) including the residual stress due to indentation and (II) having the residual stress annealed at an elevated temperature. The plots of these functions for both series of experiments yielded within the precision of measurement the same slope, being about 32 percent less than the $-1/3$ slope which a fracture toughness independent of crack extension would indicate. Considering the criterion for crack extension and the criterion for specimen failure, solutions were derived to accord with the respective conditions of the two series of experiments, and both of these methods gave the same value within the precision of measurements for the rising fracture toughness of the alumina ceramic.

Keywords: Alumina ceramic, bending stress, crack extension, indentation load, fracture toughness, residual stress, stress intensity factor.

Nomenclature

- a Crack depth (Fig. 1).
- a_0 Initial notch depth.
- a_1 Crack depth produced by an indentation load.
- a_t Crack depth when crack growth becomes unstable.
- A Coefficient evaluated by a least squares fit of eq 18.
- b Half-width of specimen (Fig. 1).
- B,C Coefficients evaluated by a least squares fit of eq 15.
- c Half-length of surface crack (Fig 1).
- c_1 Half-length of surface crack produced by an indentation load.
- E Modulus of elasticity for a given material.
- F Load required to rupture a specimen.
- k Coefficient of fracture toughness
(Subscript 0 denotes $a_0 = 0$, and subscript 1 denotes $a_0 = a_1$ in eq 2).
- K Applied stress-intensity factor (plane strain).
- K_b Stress-intensity factor due to a bending stress.
- K_c Critical stress-intensity factor (fracture toughness) for a given material.
- K_r Residual stress-intensity factor due to an indentation load cycle on a specimen.
- l_1 Major span for loading a bend specimen.
- l_2 Minor span for loading a bend specimen.
- m Crack-depth exponent of fracture toughness.
- M Bending moment on a specimen.
- P Indentation load.
- R Crack-growth resistance (energy per unit of cracked surface) of a given material.
- S Bending strength, stress on the outer fiber required to rupture a specimen.

- t Thickness of specimen in direction of crack depth (Fig. 1).
- X Coefficient of residual stress-intensity factor.
- Y Configuration coefficient for bending stress-intensity factor.
- v Poisson's ratio.
- σ Bending stress on the outer fiber of a specimen.
- ϕ The angle which defines a point on the crack front of a semi-elliptical surface crack (Fig. 1).

I. Introduction

Recently, Cook, Lawn and Fairbanks [1] used controlled indentation flaws to study the strength characteristics of ceramics as a function of crack size relative to grain size. They observed that the strengths of several ceramics first showed a steady increase on diminishing the indentation load, but subsequently tended to a plateau as the contact size began to approach the characteristic grain size. They postulated the existence of a microstructural driving force, analogous to the residual indentation driving force, to describe a tendency for the strength to become somewhat smaller than one would expect from a macroscopic toughness value as the flaw size gets smaller. This interpretation is the converse of the concept of fracture toughness of a material increasing as a function of crack extension except that the authors advocated that their calculated values of rising fracture toughness be specified by two limiting parameters. The indentation-controlled region of large-scale crack behavior would define the first limit as the conventional macroscopic fracture toughness response, where $[d \log (S)/d \log (P) = -1/3]$ corresponds to a maximum value of fracture toughness independent of crack extension. The microstructure-controlled region of small cracks would define the second limit where the strength is no

longer dependent on indentation load, but the authors acknowledged a suggestion by others that the observed toughness would not drop below the value appropriate to either single-crystal or grain-boundary fracture.

The property of fracture toughness increasing as a function of crack extension has been shown to exist for some materials which consist of irregular-shaped aggregates that are joined together in a matrix of another phase. Krause and Fuller [2] determined the fracture toughness of a polymer concrete material to increase with crack extension which was controlled by various chevron-notched configurations. Using a compliance method, Steinbrech, Knehans, and Schaarwachter [3] performed fracture experiments under conditions of slow crack growth with prenotched, three point bend specimens of polycrystalline alumina. They examined the influence of grain size on crack-growth resistance; coarser grained material showed less resistance initially for small cracks, but the increase of resistance in the coarse-grained material was greater with crack propagation than a fine-grained material.

The concept of crack growth resistance rising with crack extension represents the situation that as a crack propagates, more energy per unit of cracked surface is required, perhaps due to the tractions of aggregate interlock and pullout or to the increase of multiple fine cracks at the main crack tip. While the calculated crack area is generally assumed planar, the fact that the actual crack path is tortuous, possibly along grain boundaries, would merely constitute a roughly constant factor systematic error. As a matter of convenience the present work will address this phenomenon in terms of plane-strain fracture toughness (K_{Ic}), which is proportional to the square-root of crack-growth resistance (R)

$$K_c = [E R / (1 - \nu^2)]^{1/2} \quad (1)$$

A derivation of a function for rising (R) has been presented [4] and is adapted here in terms of (K_c). A rising (R or K_c) is assumed to be a function of crack extension ($a - a_0$) only and to be invariant with the initial notch depth (a_0). The simple condition for the derivation is that the critical crack depth is approximately proportional to the initial notch depth. The general solution follows

$$K_c = k (a - a_0)^m \quad (2)$$

where (k) and (m) are constants. The basis for the derivation of eq 2 follows from the criterion for slow, stable crack extension

$$K = K_c \quad (3)$$

and from the criterion for rupture which is the point of tangency

$$dK/da = dK_c/da \quad (4)$$

where (K) is the applied stress-intensity factor.

In the following presentation expressions will be derived based on eqs 2, 3, and 4 to relate observed bending strength data as a function of indentation load in two series of experiments: (I) including the residual stress due to indentation and (II) having the residual stress annealed at an elevated temperature. Through a least-squares method these expressions will be fitted to evaluate the coefficients (k) and (m) for an alumina ceramic.

II. Experimental

The indentation-strength measurements were carried out on a vitreous-bonded ceramic of 96 weight percent Al_2O_3 . The microstructure and chemical composition of this commercially manufactured ceramic was characterized extensively in an earlier investigation of its creep and creep rupture properties [5]. Originally, the irregular-shaped grains of Al_2O_3 , having dimensions from 3 to 20 μm in any direction, were bonded by a vitreous phase consisting of SiO_2 , Al_2O_3 , and MgO . Flexure specimens were cut to a nominal size of 3 mm x 5 mm x 50 mm with a metal-bonded 60 μm diamond blade. The prospective tensile and compressive surfaces were ground flat and parallel and the edges slightly chamfered by a resinoid-bonded 30 μm diamond wheel. The prospective tensile surface was in addition polished with 9 μm diamond paste to produce a finish for subsequent optical microscopic examination. The finished specimens were annealed 4 da at 1050°C to make them less susceptible to creep rupture. Following this annealing process some devitrification occurred in the bonding phase [5].

A series of three uniform flaw sizes were produced 2 mm apart in the center of the prospective tensile surface of each flexure specimen by a Vickers diamond pyramid. Care was taken to orient one set of radial cracks of an indentation flaw to be parallel to the cross-section of the specimen where the prospective rupture would occur. Flaw sizes were controlled with indentation loads ranging from 3 to 300 N. All indentations were made at room temperature in air with a displacement rate of approximately 0.4 mm/sec. The pyramid was allowed to contact the specimen surface for about 30 sec; then the loaded pyramid was withdrawn to complete the load cycle.

Surface cracks in the direction of prospective rupture were measured immediately after the indentations by a shadow technique of optical microscopy. Illumination of a small area alongside the surface crack cast a shadow over the slightly raised edges of the crack. The photographed image was compared to that of a calibrated scale of the same magnification, ranging from 140 to 310 times for large to small cracks, respectively.

Strength tests were conducted at room temperature in two series of experiments: (I) including the residual stress due to indentation and (II) having the residual stress annealed at an elevated temperature. While Series I experiments were performed immediately following indentation, the specimens used in the Series II experiments were annealed approximately 1 h at 1050°C following indentation. Heating and cooling rates were approximately 20 deg/min. All specimens ruptured at an indentation. A universal testing machine was used to produce the load (F) required to rupture a specimen under 4 point bending. The gear-driven crosshead of the machine was operated at a constant speed of 0.5 mm/min, and the load was transmitted through a semi-spherical block with fixed loading rods of 3 mm diameter. Loading was indicated by a linear strain gauge and was recorded on a constant speed chart. The gauge was calibrated at the full scale of the chart with a known 10 kg mass and the local 9.801 m/s² acceleration of gravity. The bending moment (M) and bending strength (S) were calculated respectively from

$$M = (F/2)(\ell_1 - \ell_2)/2 \quad (5)$$

and

$$S = 6M/2 b t^2 \quad (6)$$

in which $l_1 = 40$ mm, $l_2 = 10$ mm, $b = 2.5$ mm, and $t = 3$ mm were the nominal dimensions as shown in Figure 1.

III. Analysis

When a significant load (P) is applied to a sharp indenter in contact with a test material and the indenter is then unloaded, semi-circular radial cracks will develop to their final lengths in the test material [7]. The driving force of the crack system may be characterized by a residual stress-intensity factor

$$K_r = X P/a^{3/2} \quad (7)$$

where (X) is a constant characteristic of the material. The crack will grow as long as ($K_r > K_c$), and an equilibrium position will be attained when ($K_r = K_c$), which is the criterion of eq 3. This phenomenon is described by the (K_r) curve and point I in Figure 2. When eq 2 with ($a_0 = 0$), is equated to eq 7, the crack depth at indentation equilibrium becomes

$$a_1 = (P/A)^{2/(3+2m)} \quad (8)$$

Where $A = k_0/X$ is a constant.

Consider that in the Series I experiments a freshly indented test specimen which has a controlled flaw of size (a_1) is subjected to a small bending stress (σ). A stress-intensity factor due to this bending stress

will be superposed upon (K_r), the crack system will grow as long as ($K > K_c$), and an equilibrium position will again be attained when ($K = K_c$). The bending stress-intensity factor may be expressed as

$$K_b = Y\sigma a^{1/2} \quad (9)$$

where (Y) is a configuration coefficient that is dependent on relative crack parameters. Catastrophic failure ensues when the criterion of eq 4 is satisfied. Figure 2 shows (K) corresponding to ($\sigma = S$), the bending strength of a specimen with an original flaw size (a_1). The point of tangency, point T of Figure 2, defines the crack depth (a_t) at rupture.

The crack depth at rupture can be determined by substituting the appropriate forms of eqs 2, 7, and 9 in eqs 3 and 4 to give

$$k_o a_t^m = Y S a_t^{1/2} + X P a_t^{-3/2} \quad (10)$$

and

$$m k_o a_t^{(m-1)} = 1/2 Y S a_t^{-1/2} - 3/2 X P a_t^{-5/2} \quad (11)$$

respectively.

Solution of eqs 10 and 11 yields

$$a_t = [4P/A(1-2m)]^{2/(3+2m)} \quad (12)$$

Dividing eq 12 by eq 3 gives the rupture to indent crack depth ratio

$$a_t/a_1 = [4/(1-2m)]^{2/(3+2m)} \quad (13)$$

The coefficient of fracture toughness (k_0) has the subscript zero to denote that (K_0) is defined by assuming ($a_0 = 0$). This means that extending the crack from (a_1) to (a_t) includes the history of any tractions which might exist up to (a_1). An alternative definition of (K_0) corresponds to ($a_0 = a_1$) where the prior history of any tractions is neglected. In this second definition the coefficient of fracture toughness has the subscript one and is simply related to the former by

$$k_1 = k_0 / (1 - a_1/a_t)^m \quad (14)$$

Experimentally, the bending strength (S) is measured as a function of indentation load (P). When eq 12 is substituted for (a_t) in eq 10, the result may be rearranged to the general form of

$$\log (S) = B \log (P) + \log (C) \quad (15)$$

Accordingly, the crack-depth exponent of fracture toughness is given by

$$\bar{m} = (1 + 3B) / (2 - 2B) \quad (16)$$

and the coefficient of fracture toughness is given by

$$k_0 = YC(-AB)^B (1-B)^{(1-B)} \quad (17)$$

The coefficients (B) and (C) can be evaluated by a least-squares-fit of eq 15 for the observed (P) and (S) data of the series I experiments. Rearrangement of eq. 8 in which eq 16 is substituted for (m) gives the coefficient

$$A = P/a_1^{2/(1-B)} \quad (18)$$

Using the observed (P) and (a_1) data in eq 18, a mean value of (A) can be calculated.

Now consider that in the Series II experiments a test specimen is annealed at an elevated temperature to relieve the residual stress resulting from an indentation load. If fracture toughness is defined by ($a_0 = 0$) in eq 2, application of a small bending stress (σ) to the specimen would produce no further crack extension until (σ) is increased to (S) to satisfy the criterion of eq. 3. But since the criterion of eq 4 is already satisfied at this point, catastrophic failure occurs ($a_t = a_1$). Combining the appropriate forms of eqs 2 and 9 to solve for (a_t) and equating it to eq 8 give

$$(YS/k_0)^{-2/(1-2m)} = (P/A)^{2/(3+2m)} \quad (19)$$

When eq 19 is rearranged to the general form of eq 15, the exponent of crack extension (m) is again given by eq 16; but the coefficient of fracture toughness is determined as

$$k_0 = YCA^B \quad (20)$$

The coefficients (B) and (C) can be evaluated by a least-squares-fit of eq 15 for the observed (P) and (S) data of the Series II experiments.

If the alternative definition of fracture toughness ($a_0 = a_1$) is assumed for the Series II experiments, the crack would extend somewhat beyond (a_1) before rupturing. Substituting the appropriate forms of eqs 2 and 9 into eqs 3 and 4 gives

$$k_1 (a_t - a_1)^m = Y S a_t^{1/2} \quad (21)$$

and

$$m k_1 (a_t - a_1)^{m-1} = 1/2 Y S a_t^{-1/2} \quad (22)$$

respectively. Solution of eqs 21 and 22 gives

$$a_t = [(2m)^m k_1 / Y S]^{2/(1-2m)} \quad (23)$$

When eqs 21 and 23 are combined to eliminate $(Y S / k_1)$, the rupture to indent crack depth ratio is given by

$$a_t / a_1 = 1 / (1 - 2m) \quad (24)$$

Substituting eq 23 for (a_t) in eq 21 results in the general form of eq 15.

The exponent of crack extension (m) is again given by eq 16, but the coefficient of fracture toughness for the alternative definition is given by

$$k_1 = k_0 / [(2m)^{2m(1-2m)} (1-2m)]^{(3+2m)/8} \quad (25)$$

where (k_0) is given by eq 20.

IV. Results

Figure 3 shows plots of the observed bending strength versus indentation load in the two series of experiments on the vitreous-bonded 96 percent alumina ceramic. The indentation load covered the range between 3 and 300 N in the Series I experiments, but only between 25 and 300 N in the Series II experiments. The coefficients (B) and (C) were evaluated by a least-squares method to fit the general form of eq 15 to the respective sets of data. These values and their respective standard deviation^s are given in Table 1. While the imprecision of the Series II experiments is approximately twice as large as that for the Series I experiments, both series of experiments yield the same slope [$B = d \log (S) / d \log (P)$] within the precision of measurements. The exponent of crack extension (m) was calculated from (B) by eq 16. The parameter log (C) is the log (S, Pa) intercept at log (P, N) = 0. The standard error of (S) was approximately the same in both series of experiments.

The coefficient (A) was determined from eq 18 in which (a_1) was assumed the same as (c_1). The half-length surface cracks were measured with $\pm 5 \mu\text{m}$ in the direction of prospective rupture at nominal indentation loads of 30, 100, 170, and 300 N, respectively. No systematic trend of (A) was evident over this range of loads. The mean value and standard error of log (A) is 7.991 ± 0.036 for these 4 measurements in SI units.

The configuration coefficient (Y) was calculated from published [9] stress-intensity factor equations for the surface crack on a specimen subject to a bending stress. The stress-intensity factor at any point along the

crack front depends on the parameters (a/t , a/c , c/b , and ϕ) which are defined in Fig 1. The calculations are valid for $0 \leq a/t < 1$, $0 < a/c \leq 1$, $c/b < 0.5$, and $0 \leq \phi \leq \pi$ radians. Figure 4 shows that the calculated value of (Y) is from 10 to 20 percent greater at the surface than at $\phi = \pi/2$ radians for the range of semi-circular cracks ($a_1 = c_1$) generated by indentation loading. Consequently, if a bending stress were applied, the crack front would tend to develop initially more at the surface than depth-wise to make the crack front become semi-elliptical. The special case where the stress-intensity factor is approximately uniform along the crack front as it grows was found to exist at

$$(a/c) = -1.5 (a/t) + 0.95 \quad (26)$$

Considering that

$$(c/b) = (a/t)(a/c)^{-1} t b^{-1} \quad (27)$$

the (Y) for this special case can be expressed simply as a function of (a/t) as shown by curve 1 in Fig 4. Individual values of (Y) were calculated at (a_1) and (a_t) for all the values of (P) in the Series I experiments, except ($P = 300$ N) which gave ($c_t/b > 0.5$). As the crack-depth varies over the range from (a_1) to (a_t), the calculated (Y) decreases approximately 0.6 percent at the lowest (P) and decreases approximately 5 percent at the highest (P). The mean and standard deviation of the calculated (Y) at the midpoint of the respective 8 ranges is 1.174 ± 0.024 . Curve 4 in Fig 4 gives (Y) calculated for a straight-through crack [10] for comparison.

Table 1 gives the values of the coefficient of fracture toughness (k_0) that were determined from eqs 17 and 20 for the Series I and II experiments, respectively. The values are surprisingly close despite the imprecision of the two sets of measurements. When the (k_1) and (k_0) values from the Series I experiments are compared, the difference can not be distinguished within the precision of measurements. Thus, any tractions that might exist on the cracked surface up to (a_1) are negligible compared to those existing between (a_1) and (a_t). Just the inverse appears, however, in the Series II experiments. If the tractions which exist on the indentation cracks were ignored in the Series II experiments, the coefficient of fracture toughness would be over-estimated by 28 percent.

Figure 5 shows fracture toughness increasing as the power function of crack extension expressed by eq 2. The Series I experiments correspond to (K_c) increasing from 3.36 to 4.83 $\text{MPa}\cdot\text{m}^{1/2}$ while covering the observed range of rupture cracks from 67 to 1140 μm , respectively. The Series II experiments correspond to (K_c) increasing from 3.48 to 4.23 $\text{MPa}\cdot\text{m}^{1/2}$ while covering the observed range of rupture cracks from 88 to 405 μm , respectively.

V. Discussion

The present work provides an alternative method for determining rising fracture toughness, but it differs in several respects with that of Cook, Lawn, and Fairbanks [1]. Essentially the formulation in the present work is based on the assumption that the rupture-crack depth (a_t) is proportional to the indent-crack depth (a_1). Alternatively, the formulation in the earlier

work is based on the assertion that a microstructural driving force may be regarded to account for the apparent decline in the fracture toughness on entering the domain of low contact loads.

The experimental results of the two methods differ remarkably. Neither of the two limiting parameters which were advocated by Cook et al. were observed in the present work. Instead, the log of bending strength was interpreted in the present work to be a linear function of the log of indentation load. The slope of this function was found approximately 32 percent smaller than the $-1/3$ slope which corresponds to a fracture toughness independent of crack extension ($m = 0$). Cook et al. contended that a slope of $-1/3$ was characteristic of the large crack domain, which was the same in both investigations; and they advocated that the corresponding macroscopic fracture toughness was one of the limiting parameters. Incidentally, the belief that the macroscopic fracture toughness was independent of crack extension no doubt encouraged Cook et al. to adopt the condition that (dK/da) be zero for the criterion of crack-growth instability; but the formulation in the present work was based on the more general condition of eq 4.

The other limiting parameter, which Cook et al. advocated would account for the apparent decline in fracture toughness, is based on the appearance that strength is invariant in the small-crack domain. The lower limit of indentation load used in the present work was slightly above a published [6] threshold load of 2 N for an alumina material. The spatial scale of the contact for a smaller load was believed insufficient to extend crack nuclei [6]. If smaller indentation loads were to induce cracks, they would be roughly the size of the grains of the alumina material used in the present work. It is conceivable that some grains would not be vitreous-bonded and

that these breaches would constitute inherent flaws in the microstructure. Consequently, the "plateau" of maximum strength would reflect the inherent flaw-size which should dominate over a smaller crack due to indentation. In fact, the success of contact-source failures in the earlier work [1] diminished markedly at the lower loads. Any apparent success could easily be attributed to chance. The correlation of an invariant strength and indentation loading in the small-crack domain to give a decline in fracture toughness is regarded with suspicion.

References

1. R.F. Cook, B.R. Lawn, and C.J. Fairbanks, "Microstructure-Strength Properties in Ceramics: I, Effect of Crack Size on Toughness," J. Amer. Ceramic Soc., 68 [11] 604-615 (1985).
2. R.F. Krause, Jr. and E.R. Fuller, Jr., "Fracture Toughness of Polymer Concrete Materials Using Various Chevron-Notched Configurations," Chevron-Notched Specimens: Testing and Stress Analysis, ASTM STP 855, J.H. Underwood, S.W. Freiman, and F.I. Baratta, Editors, American Society for Testing and Materials, Philadelphia, 1984, pp. 309-323.
3. R. Steinbrech, R. Khehans, and W. Schaarwachter, "Increase of Crack Resistance During Slow Crack Growth in Al_2O_3 Bend Specimens," J. Materials Science, 18, 265-270 (1983).
4. D. Broek, Elementary Engineering Fracture Mechanics, Noordhoff International Publishing, Leyden, The Netherlands, 1974, pp. 122-126, 185-191.

5. S.M. Wiederhorn, B.J. Hockey, R.F. Krause, Jr., and K. Jakus, "Creep and Fracture of Vitreous-Bonded Aluminum Oxide," J. Materials Science, 21, (1986).
6. B.R. Lawn and D.B. Marshall, "Hardness, Toughness, and Brittleness: An Indentation Analysis," J. Amer. Ceramic Soc., 62 [7] 347-350 (1979).
7. G.R. Anstis, P. Chantikul, B.R. Lawn, and D.B. Marshall, "A Critical Evaluation of Indentation Techniques for Measuring Fracture Toughness: I, Direct Crack Measurements," J. Amer. Ceramic Soc., 64 [9] 533-538 (1981).
8. P. Chantikul, G.R. Anstis, B.R. Lawn, and D.B. Marshall, "A Critical Evaluation of Indentation Techniques for Measuring Fracture Toughness: II, Strength Method," J. Amer. Ceramic Soc., 64 [9] 539-543 (1981).
9. J.C. Newman, Jr. and I.S. Raju, "An Empirical Stress-Intensity Factor Equation for the Surface Crack," Engineering Fracture Mechanics, 15, 185-192 (1981).
10. J.E. Srawley and B. Gross, Cracks and Fracture, ASTM STP 601, American Society for Testing Materials, Philadelphia, 1976, pp. 559-579.

Table 1. Experimental values of parameters that define fracture toughness of a vitreous-bonded 96 percent alumina ceramic. The uncertainty for each value is its standard deviation.

Parameter	Series I $K_C = K_r + K_b$	Series II $K_C = K_b$
log (C)	8.5601 ± 0.0101	8.7340 ± 0.0248
B	-0.2284 ± 0.0063	-0.2177 ± 0.0124
m	0.1281 ± 0.0083	0.1424 ± 0.0167
$10^{-6} k_0^a$	11.50 ± 0.76	11.59 ± 1.62
k_1/k_0	1.058	1.278
Standard Error of S (percent)	±0.94	±1.09
Number of experiments	27	10

^aBased on values of (A) and (Y) given in the text.

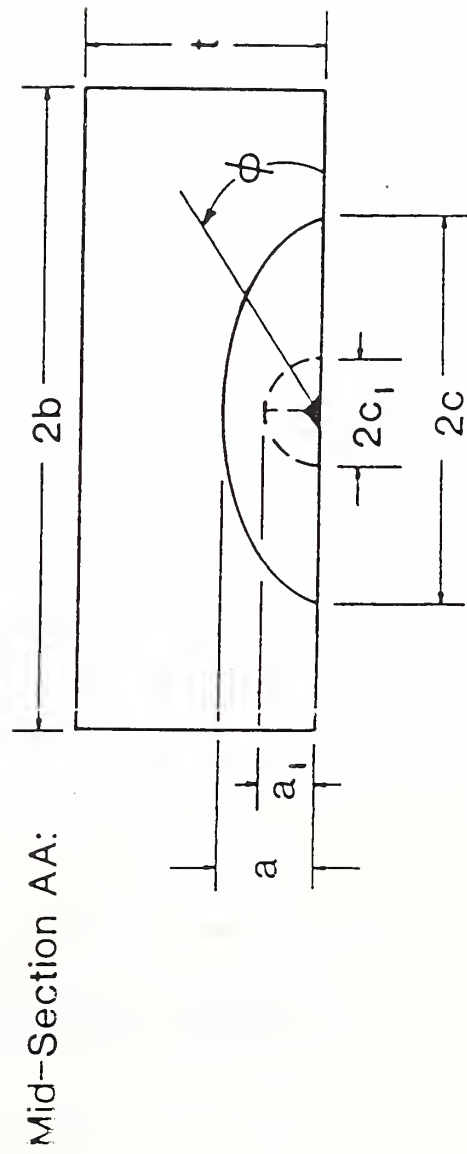
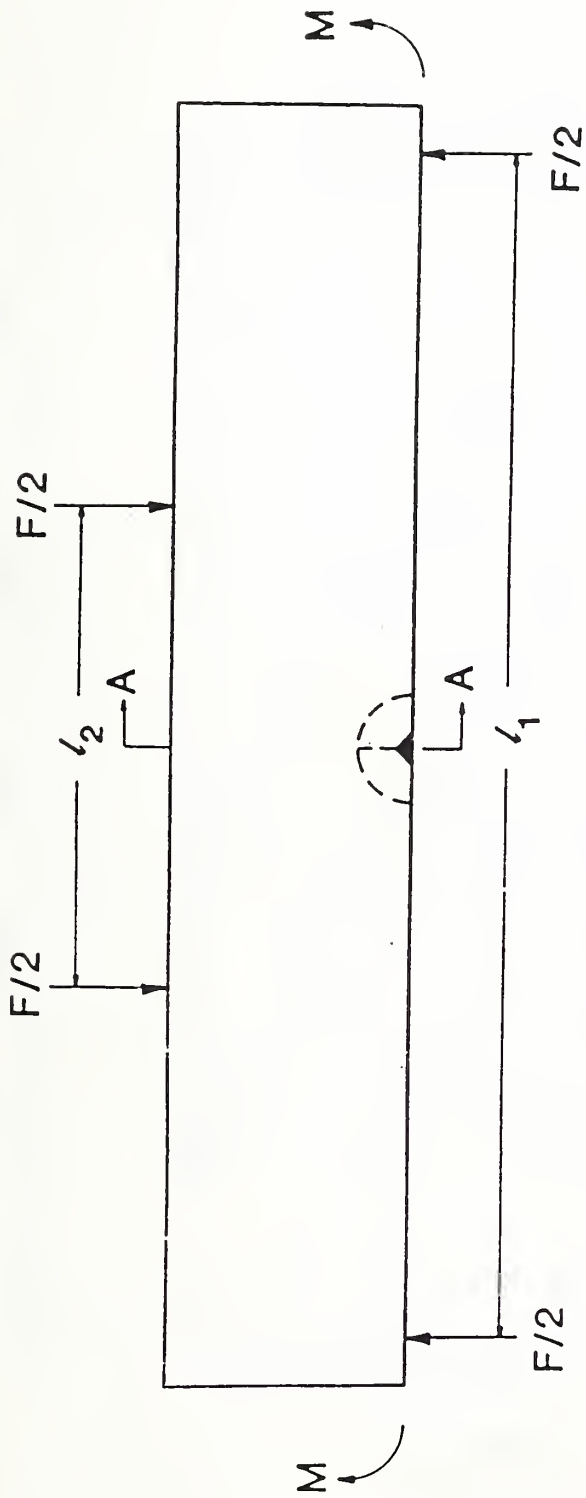


Figure 1. Schematic of surface crack by Vickers indentation at the center of the tensile surface of a bar specimen subject to a bending moment.

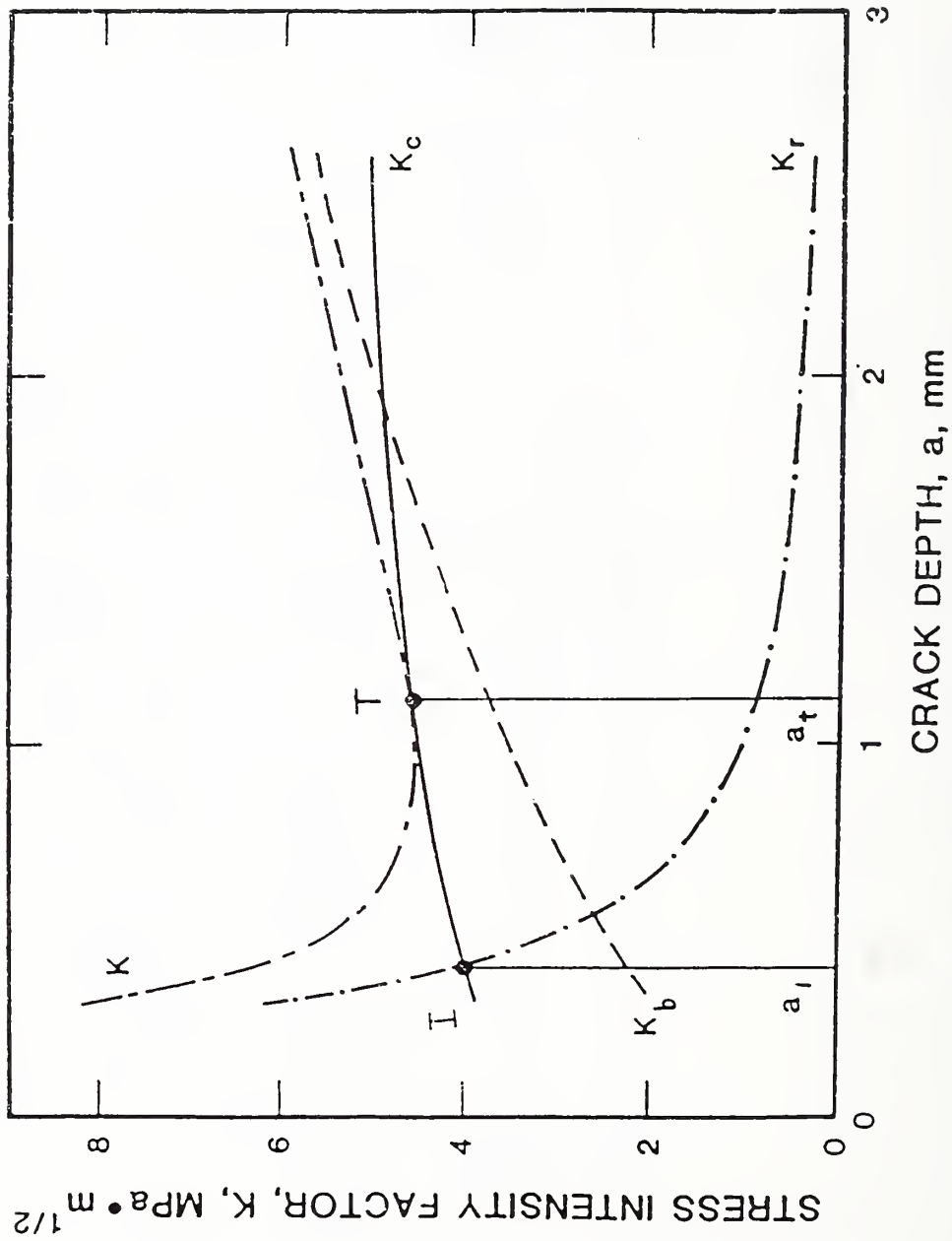


Figure 2. Typical example of stress-Intensity factor as a function of crack depth. Point I represents completion of initial crack damage due to indentation load cycle (167 N in this example). Point T represents crack extension at rupture due to superposition of the

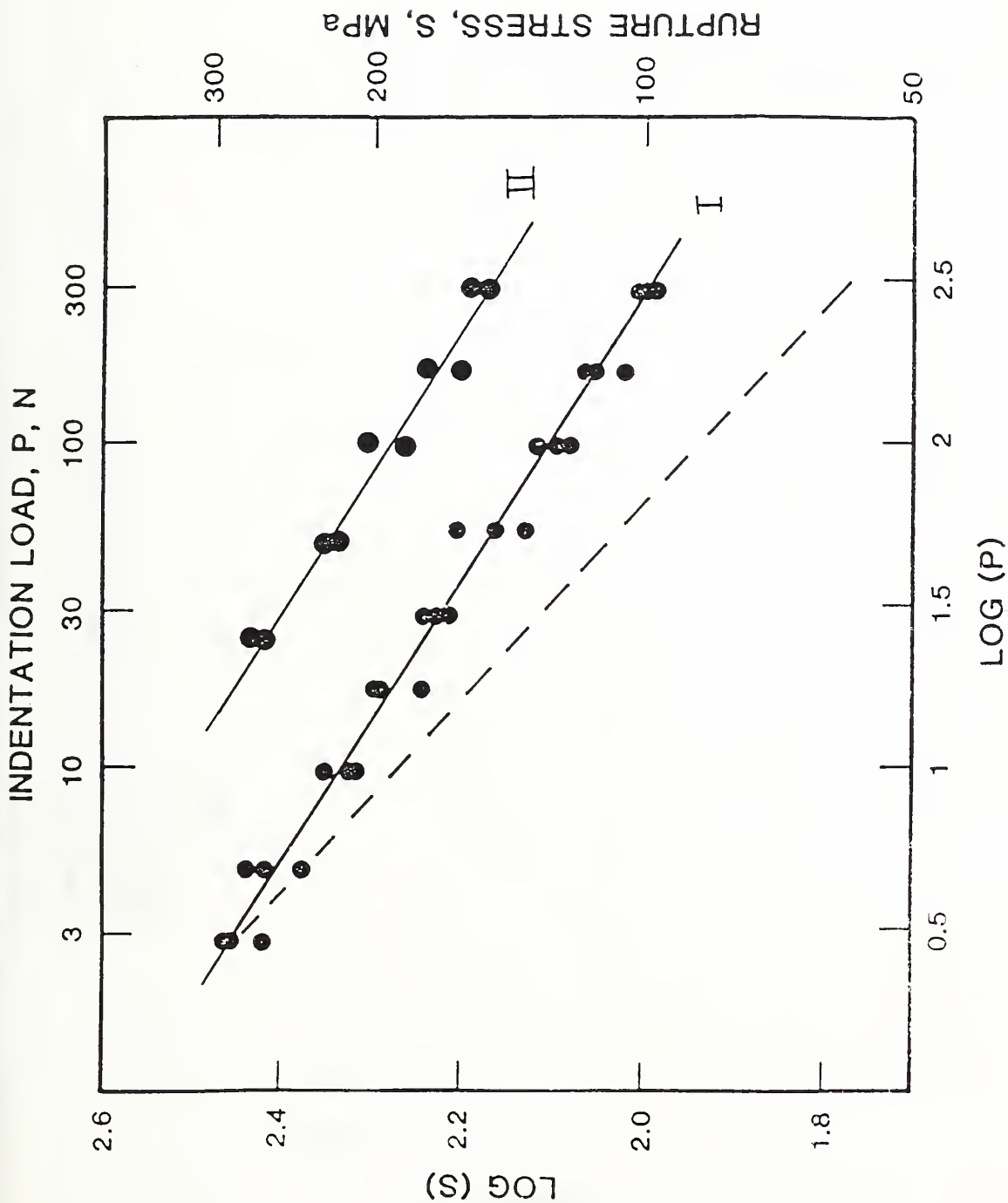


Figure 3. Log of observed bending strength as a function of the log of indentation load in two series of experiments: (I) including the residual stress due to indentation and (II) having the residual stress annealed at an elevated temperature. The solid lines are least-square-fits of eq 15, and the dashed line has a slope of $-1/3$ which a fracture toughness independent of crack extension would indicate ($m = 0$ in eq 2).

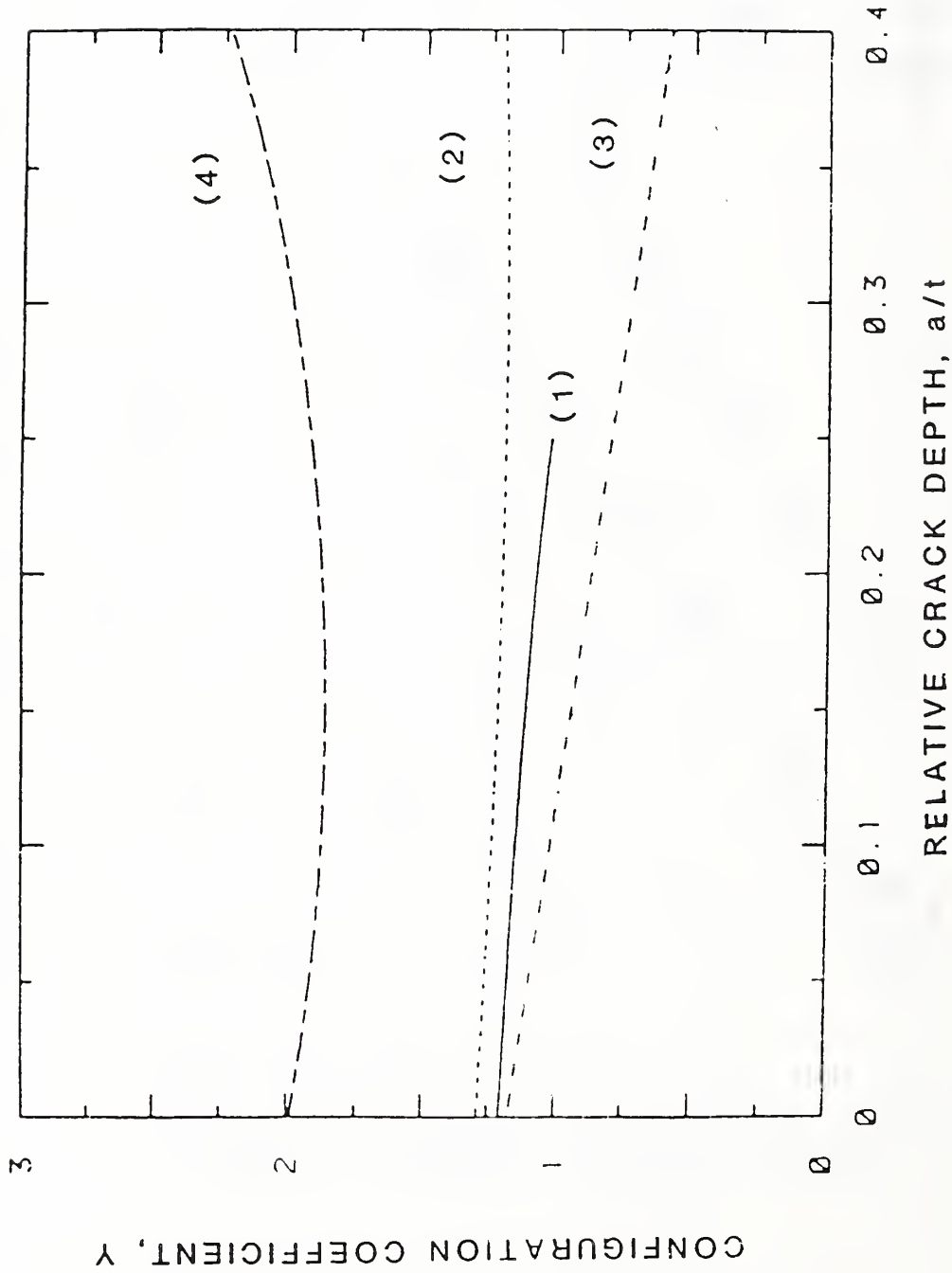


Figure 4. Calculated configuration coefficient as a function of relative crack depth in a bar specimen subject to a bending load. Curve (1) corresponds to a semi-elliptical crack having uniform stress-intensity factor along its crack front. Curves (2) and (3) correspond to the points on the crack front of a semi-circular crack at $\phi = 0$ and $\pi/2$ radians, respectively. Curve (4) corresponds to a straight through crack.

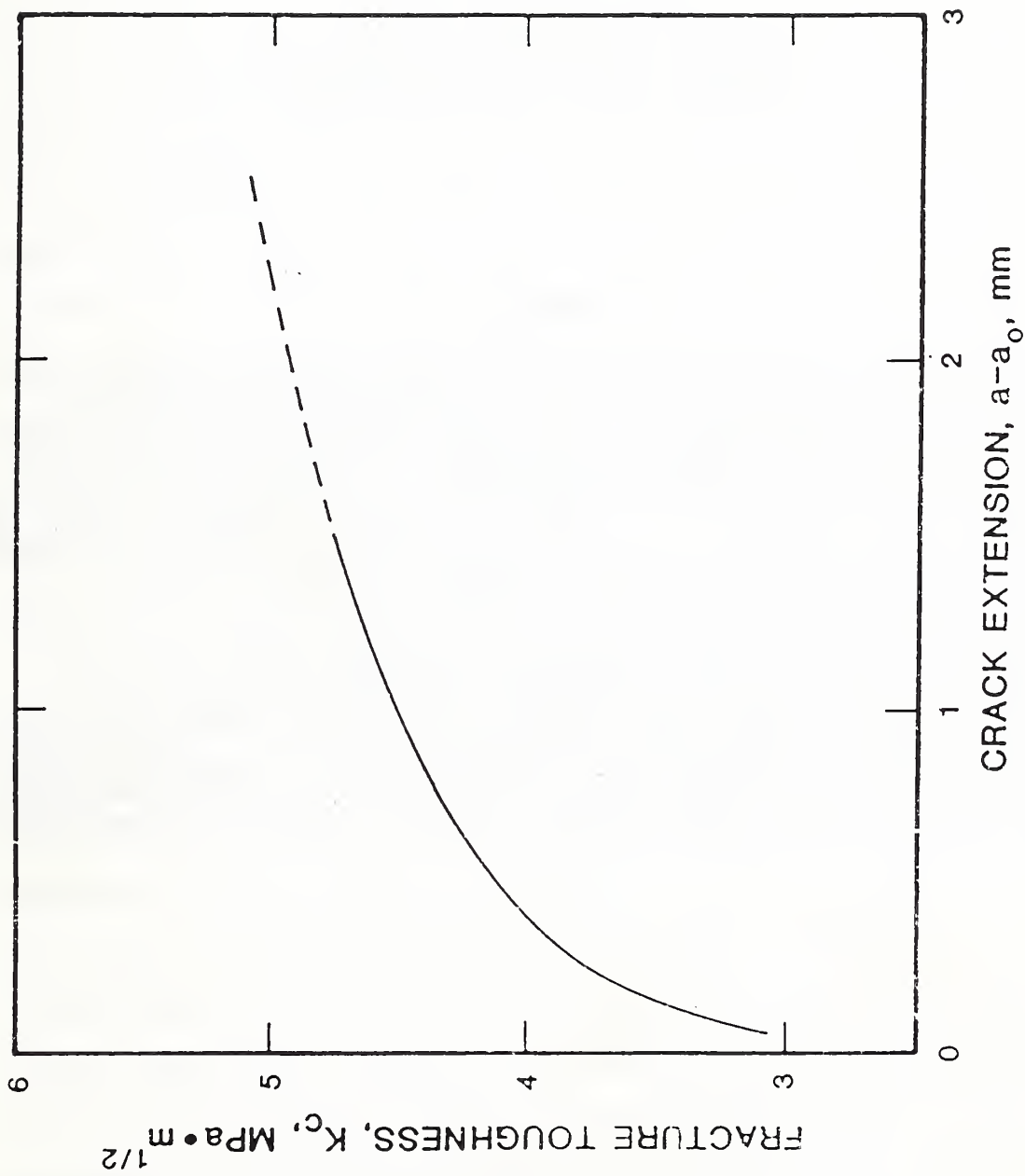


Figure 5. Fracture toughness as a function of crack extension in a vitreous-bonded 96 percent alumina ceramic, having irregularly shaped grains of 3 to 20 μm in size.

COAL SLAG PENETRATION IN A MAGNESIUM CHROMITE REFRACTORY

S.M. Wiederhorn and R.F. Krause, Jr.
Institute for Materials Research and Engineering
National Bureau of Standards
Gaithersburg, MD 20899

Jing Sun
Shanghai Institute of Ceramics
Shanghai, Peoples Republic of China

ABSTRACT

The effect of coal slag on the microstructure and creep behavior of a MgCr_2O_4 refractory was evaluated. As the slag penetrated the refractory, ion exchange between the refractory and the slag changed the composition of the slag from anorthite-like to diopside-like. This modification of the slag composition is believed to have reduced its viscosity and enhanced its reactivity. The creep rate of the refractory brick increased by a factor of ≈ 3 when slag penetrated into the brick. Creep behavior was rationalized in terms of the spacing and size of the aggregate particles within the refractory, and the structure and composition of the material bonding the aggregate particles together. It is suggested that refractory disintegration involves creep deformation at the hot face of the brick caused by mechanical loading and stresses due to ion exchange within the brick. The results of this paper suggest that refractory performance can be improved by chemical modification of the brick so as to prevent a reduction of slag viscosity during penetration. This improvement of performance might be achieved by the replacement of MgO in the brick by a network former such as Al_2O_3 .

1. INTRODUCTION

Magnesium chromite refractories are prime candidates for use as linings at the hot face of slagging coal gasifiers. Indeed, this type of refractory is currently being used in pilot plants and in full size coal gasification plants in the United States and Europe [1]. Experience in the field indicates that these refractories are resistant to high temperature dissolution by the types of slags that are present in slagging gasifiers. This field experience is consistent with earlier laboratory studies that suggested high chromia refractories as likely candidates for slagging gasifiers [2-4]. Despite their promise, however, these refractories do exhibit cracking and spalling near the hot face under some conditions [5]. The cracking seems to result from the penetration of the slag into the hot surface of the refractory with subsequent reaction to destroy the structural integrity of the refractory.

To improve the performance of refractories in slagging gasifiers, a deeper understanding of the penetration process and its role in controlling creep and rupture of these refractories is needed. In this paper, the results of an investigation of the role of coal slag composition on penetration and creep behavior of a MgCr_2O_4 refractory is presented. The data suggest a strong correlation between structural stability of the refractory and the viscosity of the intergranular vitreous phase that forms in the refractory as a consequence of slag penetration. The lower the viscosity of the vitreous phase, the more readily the surface of the refractory disintegrates. The chemical processes that control the viscosity of the vitreous phase and the effect that this vitreous phase has on creep and creep rupture are discussed.

2. EXPERIMENTAL PROCEDURE

The material selected for study was a MgCr_2O_4 refractory composed of approximately 20 weight percent MgO and 80 weight percent Cr_2O_3 . The refractory consisted almost entirely of the spinel crystal structure, but since the material was chromia rich, corundum grains of Cr_2O_3 were found scattered as precipitates in the spinel. Samples of the material were from two sources: a new brick obtained directly from the manufacturer; and a section of a brick obtained from a gasifier plant. The latter had been cycled from ambient to approximately 1200°C - 1600°C at least 11 times and had been in service for at least 475 hours under a variety of coal residues before being removed for testing.

In order to simulate the creep behavior of the material in service and to investigate the cause of the spalling observed in the hot face of the refractory, it was important to duplicate the structure of the refractory taken from the slagging gasifier plant. Hence, specimens from the newly manufactured refractory brick were impregnated with several synthetic slags, the compositions of which are given in Table 1. The synthetic coal slag, which was similar to that from a Western coal, has been used extensively at Argonne National Laboratories in studies of the corrosion of ceramic refractories exposed to coal slag [6]. The anorthite slag, which has only three major components of the synthetic coal slag, was selected as a simplified version of this slag. The diopside slag was included because its composition resembles that found by a microchemical analysis of the vitreous phase inside the MgCr_2O_4 refractory from the coal gasifier. The slags in Table 1 were synthesized from weighed portions of reagent grade

CaCO₃, Al₂O₃, SiO₂, Fe₂O₃, MgO, K₂CO₃ and Na₂CO₃ powders. After each mixture of powders was blended, a small amount was melted in the temperature range 1500°C to 1600°C in a platinum vessel. The remainder was then added slowly until the total batch of 200 to 600 g formed a melt. The melt was stirred with a platinum propeller for about 2 hours.

Creep measurements on the newly manufactured brick were conducted on specimens nominally 12 by 12 by 35 mm. Specimens were diamond-sawed to the nominal size and their surfaces diamond-ground flat and parallel to a 30 μm finish. Specimens were either tested without further preparation, or were preheated to 1500°C and soaked for a period of 24 hours in a volume of slag (Table 1) that was ≈30 times the volume of the specimen. After withdrawal from the slag, specimens were annealed at 600°C for several hours before cooling to room temperature. They were then reground to final dimensions for high temperature creep studies. Because the thickness of the section of brick from the gasifier was only ≈ 10 mm, it was sawed into smaller specimens, 8 by 8 by 16 mm, than those from the new brick.

Creep studies were conducted in a gas tight furnace where a 500 ml/min flow of 99.99% pure nitrogen gas maintained a low partial pressure of oxygen in the environment; this environment limited decomposition of the MgCr₂O₄ during each creep test. To protect the furnace interior from contamination, a muffle tube of Al₂O₃ surrounded each specimen. Specimens were separated from the silicon carbide push rods by 99.9 percent Al₂O₃ loading platens, 6 mm thick, and alignment was maintained during testing by a hemispherical silicon carbide cap located between the upper push rod and the alumina platen. New platens used for each creep test were easily separated from the push rods afterwards.

Slag-free specimens were tested in compressive creep without further preparation. Slag penetrated specimens, however, had to be protected and sealed in order to prevent reaction of the slag within the specimens with the Al_2O_3 platens and the silicon carbide push rods¹. To retain the slag within the refractory during the test, specimens were wrapped around their sides with platinum foil, 0.09 mm thick. Both loading ends were covered with platinum foil 0.03 mm thick. The side seam of the foil was welded closed at room temperature, whereas the bottom and top seams self-welded at the test temperature. Experiments using the same techniques on a vitreous-bonded Al_2O_3 indicated little difference in creep behavior between wrapped and unwrapped specimens, suggesting that the platinum foil has a negligible effect on the creep rate of these specimens at the test temperature.

Creep studies were conducted in the temperature range 1350°C to 1550°C. Specimens were soaked at temperature for at least one hour before testing; then a constant load was applied to the specimen by setting the load cycle control of a universal testing machine to narrow limits [7]. Displacements were measured using a linear variable differential transformer to determine the position of the cross-head of the test machine. Experiments were terminated generally at 0.02 to 0.04 percent maximum strain. The true value of the strain was used to calculate the creep rate of this material at a given stress and temperature.

The microstructure of the refractory was evaluated by both optical and scanning electron microscopy. Specimens taken from various positions in the brick were vacuum impregnated with epoxy resin to avoid microstructural damage and pull-out during polishing. Standard diamond polishing techniques were used to prepare specimens for microscopic examination. Chemical compositions of both the slag within the refractory, and the grains of the refractory were determined using x-ray energy dispersive spectroscopy. To attain a high degree of accuracy in the analysis, specimens of known composition were used to calibrate the principal elements (Ca, Mg, Al, Cr, Fe) found in the refractory. Finally, the crystalline structure of all phases present were confirmed by x-ray diffraction analysis.

3. RESULTS

3.1 Microstructural Analysis

3.1.1 Brick from the Gasifier

A section of the brick from the coal gasifier is shown in figure 1. As can be seen, the slag from the gasifier penetrated to a depth of ≈ 55 mm from the hot face, and cracks developed at depths of up to ≈ 15 mm from the hot face of the brick. The section of the brick shown in figure 1 was sectioned to obtain specimens for microstructural analysis. Specimens were taken from the hot face, from the boundary determined by the limits of slag penetration and from the unpenetrated portion of the brick.

The microstructure of the unpenetrated portion of the brick, figure 2, is similar to that of the freshly manufactured brick. The brick contained MgCr_2O_4 aggregate particles 1 to 3 mm in dimensions, bonded in a matrix of much finer grains of MgCr_2O_4 . The black area in figure 2 represents the finer grains of the brick, which were not easily penetrated by the epoxy resin used to mount the specimens. The scanning electron micrograph of figure 3 shows the dark region to consist of submicron size particles of MgCr_2O_4 . As only slight traces of SiO_2 were detected in the unpenetrated portion of the brick, the MgCr_2O_4 grains may have been directly bonded, or, as is more likely considering recent studies of the structure of grain boundaries in oxide and nitride ceramics [8-9], were bonded by a thin layer ($\approx 1-2$ nm) of an amorphous phase. The fact that many of the MgCr_2O_4 (spinel) grains contain plate-like Cr_2O_3 (corundum structure) precipitate particles, figure 4, indicates a chromium rich composition in the newly manufactured brick. The measured bulk density of the newly manufactured brick suggested a porosity of ≈ 19 volume percent. Since the brick appears to be readily penetrated by slag, this porosity is largely interconnected, and permits easy access of the slag to the interior of the brick during high temperature exposure.

The appearance of the penetrated portion of the brick, figure 5, is in sharp contrast to that of the unpenetrated portion of the brick. The region between the large aggregate particles now contains grains that are much larger (≈ 10 to $100 \mu\text{m}$) than the original submicron size grains, suggesting considerable growth of these grains as a consequence of the slag penetration. Slag shows up between the spinel particles as the dark grey areas in figure 5, and forms about 6 volume percent of the inter-aggregate region in the penetrated portion of the brick. The black areas in figure 5

are voids, which form ≈ 20 volume percent of the inter-aggregate region. These voids appear to be unconnected and, therefore, do not form a continuous path through the penetrated portion of the brick. The connected porosity of the original brick is apparently filled by the slag, leaving behind remnant, isolated voids in the brick after penetration.

Micrographs of the cracks that appear near the hot face of the brick show that these are not cracks at all, but blunted, elongated cavities, figure 6. The roots of these crack-like cavities were slag filled with small $\approx 50 \mu\text{m}$ grains of magnesium chromite floating in the slag. The rounded shape of the cavities suggests a flow process as an important factor in their formation. These crack-like cavities undoubtedly were formed at elevated temperatures as a result of creep deformation at the hot face of the refractory.

The principal elements in the spinel grains near the hot face of the brick were chromium, magnesium and iron², figure 7. The concentration of iron at the hot face was approximately 18 weight percent. The iron concentration diminished rapidly with distance from the hot face so that at 2.5 mm from the hot face, the concentration of iron was nearly zero. Apparently iron does not travel with the slag into the brick, but is absorbed by the MgCr_2O_4 spinel grains at the hot face. The spinel effectively getters the iron from the slag that penetrates the brick. At depths greater than ≈ 3 mm from the hot face, the composition of the grains of the brick approach that of the unreacted brick, which is slightly rich in chromium sesquioxide (0.515 moles of Cr_2O_3 to 0.485 moles of MgO). Thus, only the spinel grains in the immediate vicinity of the coal-slag, refractory interface are altered by reaction with the slag. The iron that

is normally present in the slag is apparently leached from the slag at the hot face and does not penetrate beneath the surface of the brick.

The chemical composition of the vitreous phase within the refractory brick was also determined as a function of distance from the hot face, Table 2. Beyond the 25 mm limit of this table, the vitreous phase was present in quantities that were too low for accurate chemical analysis by the techniques used³. Despite the presence of iron within the spinel grains at distances less than 2.5 mm from the hot face, figure 7, iron was not detected in the vitreous phase within this distance. As no iron was found in the vitreous phase, iron probably penetrated into the brick by solid state diffusion. Because Cr_2O_3 is slightly soluble in the slag, it remained at the ≈ 3 percent level in all measurements⁴. The Al_2O_3 penetrated a distance of ≈ 15 mm from the hot face of the brick, but was not present in measurable quantity beyond this distance. Finally, as the distance from the hot face increased, the MgO concentration in the slag increased. Since the only source of MgO was the MgCr_2O_4 of the brick, these results suggest that during high temperature exposure, MgO was leached from the brick by the slag. The MgO then migrated through the vitreous phase to the hot face of the brick where it was removed by the slag running down the wall of the gasifier. These observations are consistent with phase diagrams [10-11] which indicate a limited solubility of Cr_2O_3 in a $\text{MgO}\cdot\text{CaO}\cdot\text{SiO}_2$ melt at 1500° . They are also consistent with earlier data by Kennedy et al. [2-4] on the same subject. Apparently, when MgCr_2O_4 is placed in contact with slag, the MgO can readily leave the spinel phase, whereas the Cr_2O_3 cannot.

3.1.2 Bricks Impregnated by Slag in the Laboratory

The composition of the intergranular vitreous phase in the refractory specimens that were slag penetrated in the laboratory is given in Table 3. Analyses were conducted on material located both at the surface and at the center of each test specimen. The intergranular vitreous phase was formed by penetration of the slag through the porous bonding matrix of the refractory. In the present study, approximately the same composition of MgO, CaO, SiO₂ and Cr₂O₃ was found in the intergranular vitreous phase for all slags and exposures. Significantly, these compositions were essentially identical to that found in the brick from the slagging gasifier.

Although the synthetic coal slag contained both iron oxide and aluminum oxide in substantial concentrations, table 1, neither of these are found in the vitreous phase at the center of test specimens, indicating that these oxides are leached from the slag at the surface of the refractory during impregnation. These findings confirm those reached after examination of the brick from the coal gasifier: neither iron oxide, nor aluminum oxide penetrated much beyond the slag-refractory interface. Finally, the leaching of MgO from the MgCr₂O₄ grains of the refractory is also confirmed by the fact that MgO is found in the intergranular vitreous phase formed by penetration of anorthite slag into the MgCr₂O₄ specimens. Since the anorthite slag originally contained no MgO, the MgO had to come from the refractory brick.

Chemical analyses of the MgCr₂O₄ grains in test specimens exposed to the laboratory slags are summarized in Table 4. These results complement those obtained on the vitreous phase, Table 3. Iron and aluminum oxide that

leave the slag are found only in the surface grains of the refractory which are now depleted of magnesium oxide. By contrast, the grains at the interior of the specimens contain only Cr_2O_3 and MgO , a finding that is consistent with the iron and aluminum oxide being leached from the slag primarily at the external surface of the specimen. The general reduction of MgO concentration in the specimen interior also suggests a general migration of the MgO from the interior of the refractory to the slag-refractory interface.

Microstructural modification of the refractory depends on the slag to which the refractory is exposed. Exposure to the synthetic coal slag resulted in a dense spinel coat at the external surface of the specimen, figure 8a. Contained within this coat were fine precipitate particles of Cr_2O_3 . Although penetrated by the slag, the microstructure of the interior of the specimen, figure 8b appeared to be much denser and better integrated than that of specimens taken from the hot face of the slagging gasifier, figure 2. The much higher concentration of Cr_2O_3 (bright phase in figure 8b) in the interior is consistent with a general loss of MgO from the specimens. An extreme example of this behavior is illustrated by the specimen exposed to the anorthite slag, figure 9, which showed a ring of corundum grains around the entire surface of the specimen. Apparently, leaching of the MgO was sufficiently complete as to convert all of the spinel phase to corundum. The interior of these specimens were similar in appearance to that of the specimen exposed to the synthetic coal slag.

Of the three synthetic slags tested, the most aggressive one was the diopside slag. When exposed to this slag for 24 hours at 1500°C , the MgCr_2O_4 refractory completely disintegrated. Similar exposure to the other

slags left the specimens in tact with relatively good microstructural integrity. To obtain some idea of the mechanism of attack, an exposure of only 4 hours at 1500°C was used with the diopside slag. At this exposure, the initiation of disintegration is apparent from the microstructure in figure 10. Although some areas of the microstructure were similar in appearance to that obtained from the synthetic coal slag exposed refractory, figure 10a, other areas figure 10b, suggest that penetration of the diopside slag through the fine aggregate particles forced the grains apart leaving large pools of slag between the grains. Deep crack-like cavities were observed along the route of slag penetration. This microstructure resembled that of specimens taken from the hot face of the slagging gasifier, suggesting an important role for diopside in the process of refractory degeneration.

3.2 Creep Measurements

Typical creep tests conducted on specimens taken from the slagging gasifier and from specimens prepared in the laboratory are illustrated in figures 11 and 12, respectively. The creep strain, ϵ , at a given applied stress, σ , and temperature, T , was represented by the following function of time, t :

$$\epsilon = A \cdot t^m \quad (1)$$

where the coefficient, A , is a function of σ and T . The coefficient A and the time exponent, m , were evaluated by a least squares fit of equation 1 to the observed creep data. Since tertiary creep behavior occurs prior to failure, the equation was fitted only to the point of inflection of the

data. The mean value and standard deviation of the time exponent, m , are summarized in Table 5 for all test conditions. The value of this parameter, ≈ 0.6 to ≈ 0.7 , indicates a work hardening behavior for most of the specimen lifetime. The deviation of the observed creep behavior (circles) from equation 1 (solid line) indicates incipient failure in compressive creep⁵; hence, the point of inflection of these curves was taken as the strain-to-failure.

The creep data for the slag-impregnated MgCr_2O_4 refractory taken from the coal gasifier (solid curves) are compared in figure 11 with creep data from newly produced refractory [7] (dashed curves). At each temperature and stress, the creep strain of the slag impregnated refractory exceeds that of the newly produced refractory. This increase in the strain at a given time was also typical of the refractory that was penetrated in the laboratory.

The strain rates of the impregnated refractories can also be compared with that of the newly manufactured refractory by differentiating equation 1 to obtain the strain rate as a function of creep strain:

$$d\epsilon/dt = m \cdot A^{1/m} \cdot \epsilon^{(1-1/m)} \quad (2)$$

Table 6 gives the strain rates calculated from equation 2 at 1 percent strain for selected temperatures and applied stresses. The table presents data for: (A) newly produced refractory; (B) slag impregnated refractory made in the laboratory; and (C) slag impregnated refractory from the coal gasification plant. These data are compared in Table 6 with creep data published earlier on another sample of newly produced refractory. The results from Table 6 indicate little difference between the creep rate

measurements in the two lots of freshly manufactured refractory. By contrast, slag appears to enhance the creep rate by a factor of ≈ 3 .

4. DISCUSSION

4.1 Slag Penetration

In this paper the effect of coal slag on the structural integrity of a MgCr_2O_4 refractory was investigated. By exposing specimens of this refractory to different compositions of synthetic slag, it was possible to elucidate the microstructural changes that resulted from slag exposure at elevated temperatures. These changes were related to physical and chemical processes that occurred at the hot face of the refractory brick. On initial contact with the hot surface, molten slag penetrates the brick by capillarity and travels to a depth that is determined by the temperature of the brick [12]. As the temperature decreases from the hot face, the slag viscosity increases and eventually the slag becomes too viscous to flow perceptibly further into the brick. Viscosity is also important as a measure of the rate of diffusive transport within the refractory after penetration by the slag. In keeping with the Stokes-Einstein equation [13-14], ionic diffusion within the slag is inversely proportional to viscosity, so that changes in composition that reduce viscosity also enhance transport within the slag, and hence accelerate degradation processes that depend on diffusive transport.

In the present experiment, acceleration of transport processes occurs as a consequence of chemical modifications of the slag during penetration. At the hot face of the refractory brick, Al^{+3} and $\text{Fe}^{+2}/\text{Fe}^{+3}$ leave the slag

and enter into the spinel structure of the MgCr_2O_4 refractory grains⁶, while Mg^{+2} leaves the grains and enters the slag, figure 13. The net effect of this exchange process is to change the composition of the coal slag from one that lies in the anorthite phase field of the $\text{CaO-Al}_2\text{O}_3\text{-SiO}_2$ phase diagram, to one that lies in the diopside phase field of the CaO-MgO-SiO_2 phase diagram. Since Al^{+3} and Fe^{+3} are both network formers, their elimination from the slag reduces its viscosity. Such a reduction in viscosity as a function of composition is observed in mixtures of anorthite and diopside glasses [15], for which the viscosity decreases as the composition is changed from anorthite to diopside. Based on this result, the vitreous phase that forms in the intergranular space of the refractory as a consequence of slag penetration is expected to have a lower viscosity than the slag in the gasifier, and therefore should provide a more active medium for chemical reaction and degradation of the refractory brick.

The loss of integrity of refractory bricks in slagging gasifiers probably involves both enhanced dissolution, and swelling and disruption of the bricks at the hot face [1-6]. The increase in dissolution rate is a consequence of lowering the melting point of the spinel phase due to the presence of iron and aluminum oxides in the coal slag [10, 11]. As the melting point is lowered, grains are dissolved at their boundaries and eventually detach from the walls of the refractory to be carried away with the flowing slag [1, 6]. This mechanism of dissolution is consistent with the appearance of the hot face of the refractory at the slag refractory interface, figure 5. Although it is an important mechanism for loss of refractory, dissolution by itself cannot be used in a simple way to explain the appearance of cracks within the hot face of the brick. Furthermore, the fact that refractories often wear out more rapidly in the field than is

predicted by laboratory measurements of dissolution rate, suggests that other processes contribute to refractory failure [1, 5]. Swelling of the hot face and subsequent spalling is one such cause of accelerated failure of refractories in slagging gasifiers. [1, 5].

A number of physical and chemical processes may be envisioned to explain the swelling that eventually results in cavitation and spalling of the hot face of the gasifier walls. As noted earlier by Bakker [1], failure probably occurs as a consequence of creep during which cavities and voids are generated at high temperature⁷. Stresses driving the creep arise either from chemical instabilities and reactions at the hot face of the refractory, or from mechanical forces that develop as a consequence of the wall construction. Mechanical forces are mainly due to the weight of the wall and to thermal expansion within the wall when the gasifier is cycled between room temperature and the operating temperature. Because the temperature of the refractory wall is greatest at the hot face, creep strains from these stresses are also greatest at the hot face. The importance of thermal expansion and structural loading to wall design has been discussed in some detail by Chen and Buyukozturk [16-17], who note that with proper design these mechanical causes of structural failure can be minimized.

Stresses at the hot face of the gasifier walls are also caused by processes that are more chemical in nature. As a consequence, differences in solubility or in rates of diffusion within the various phases of the refractory brick can lead to osmotic type of pressures that also cause the refractory to creep. The absorption of $\text{FeO/Fe}_2\text{O}_3$ and Al_2O_3 into the spinel phase of the brick, for example, is equivalent to a net transport of

matter from the slag to the hot face of the brick, resulting in an increase in the volume of this phase. Under the physical constraints existing at the hot face, this increase in volume results in creep of the brick towards the center of the gasifier [1, 5] thereby providing a mechanism for cavitation at the hot face⁸. In this regard, it may be significant that cavitation at the hot face occurs over the same 15 mm depth that is observed for the absorption of the Al_2O_3 . Creep at the hot face of the brick can also result from differential dissolution of the MgO from the MgCr_2O_4 . Because crystals usually expand their volume upon dissolving or melting, the dissolution of the MgO from the MgCr_2O_4 results in a volume expansion of the vitreous phase within the refractory brick. If the microstructure of the brick is sufficiently restrictive and the viscosity of the vitreous phase is sufficiently high to prevent the free flow of the vitreous phase between the interior and exterior of the brick, a build-up of pressure due to dissolution will also lead to creep at the hot face of the refractory.

4.2 Creep and Creep Rupture

Whatever the driving force for creep, refractory failure occurs only when a critical creep strain is exceeded, so that the development of a useful theory for creep induced spalling of refractories requires an understanding of microstructural and environmental factors that determine the critical strain for creep rupture. In particular, an understanding of void generation and cavity growth within refractories is needed. Despite recent experimental and theoretical advances on creep rupture of ceramics [18-19], the level of understanding needed for the development of a useful theory of creep rupture of refractory materials has not yet been achieved.

However, in the absence of a detailed understanding of failure mechanisms, empirical relations, such as the Monkman-Grant relation [20], may be useful for the development of failure models. The Monkman-Grant relation suggests an inverse linear relation between the failure time and the minimum creep rate; ceramics such as hot-pressed silicon nitride [21], dense fine-grain Al_2O_3 [22] and vitreous bonded Al_2O_3 [23] all obey this type of equation. Furthermore, unpublished data by the present authors indicate that a zirconia-alumina-silica refractory also obeys this relation. If a Monkman-Grant relation is also applicable to the failure of MgCr_2O_4 refractory, then an increase in creep rate of ≈ 3 as a consequence of slag penetration, would lead to a factor of 3 decrease in lifetime of the slag penetrated refractory.

Results from the present study on the creep of slag impregnated MgCr_2O_4 indicate a low sensitivity of the creep rate to slag penetration. Although the inter-aggregate space in the refractory was completely filled with slag, creep rates increased by only a factor of ≈ 3 over that for the as-manufactured brick [7]. This modest increase in creep rate can be traced to changes in microstructure when slag penetrates the brick. Because of their large size, 1 to 5 mm, the aggregate particles of the MgCr_2O_4 refractory may be considered rigid with regard to the binder or inter-aggregate microstructure that holds the aggregate particles together, so that resistance to deformation is solely determined by this fine grained microstructure. When slag enters into the fine grained inter-aggregate microstructure, it effectively lubricates the grain boundaries of this structure by providing an easy path for mass transport and dissolution, both of which enhance creep in two phase ceramics. This enhancement of creep rate is opposed by the grain growth that occurs within the

inter-aggregate microstructure when penetrated by slag. Thus, two opposing factors influence the creep behavior of this structure and the effect of slag penetration on creep will depend on the balance of these two factors.

Using current theories of two phase creep, these ideas can be expressed in more quantitative terms. The creep of rigid particles in creeping matrix can be expressed in terms of the size, D , of the aggregate particles, the spacing, W , between the aggregate particles, and the effective viscosity, μ' , of the bonding phase, figure 14. For most theories, the creep rate is inversely proportional to the viscosity and is related to W and D through a simple power function of these two variables. Creep equations for percolation [24] (eq. 4), and transport controlled solution-precipitation [25, 26] (eq. 5) are presented here as examples of the role of microstructure on creep:

$$d\varepsilon/dt \propto (\sigma/\mu') \cdot (W/D)^3 \quad (4)$$

$$d\varepsilon/dt \propto (\sigma/\mu') \cdot (W/D)D^{-2} \quad (5)$$

The creep rate depends on the structure of the material primarily through the parameters W and D , and, since the inter-aggregate bonding phase also has structure, through the effective viscosity, μ' , of the inter-aggregate phase. Because the aggregate particle size and spacing are unaffected by slag penetration, the influence of slag on the creep behavior of these materials will occur almost entirely through the role that slag plays in determining the effective viscosity of the inter-aggregate phase.

If one defines the viscosity of the inter-aggregate phase as the ratio of local stress driving the creep of this phase, to the creep rate of the inter-aggregate phase, then the viscosity, μ' , depends on microstructure as is illustrated by the following three equations: eq. 6 for transport controlled solution-precipitation creep [25-27]; eq.7 for interface controlled solution-precipitation creep [25-27]; and eq.8 for percolation [24]:

$$1/\mu' \propto (1/\mu) \cdot (w/d) d^{-2} \quad (6)$$

$$1/\mu' \propto (1/\mu) \cdot (w/d) \quad (7)$$

$$1/\mu' \propto (1/\mu) \cdot (w/d)^3 \quad (8)$$

w and d are the intergranular spacing, and grain size of the inter-aggregate phase, and μ is the viscosity of the glass in the inter-aggregate phase, figure 14.

As the ratio w/d increases, each of these equations predicts an increase in the creep rate at a given temperature and applied stress. For dilute slag concentrations, w/d is proportional to the volume fraction of slag, so that when creep is determined by interface controlled solution precipitation or percolation, the creep rate depends only on the volume fraction of slag. When creep is determined by transport controlled solution precipitation, the creep rate also depends independently on the grain size of the inter-aggregate particles. Regardless of the particular

theory considered, the ratio w/d in the slag penetrated brick will have to be greater than that in the newly manufactured brick in order to explain the enhancement of the creep rate as a consequence of slag penetration.

From the micrographs of the present study, semi-quantitative estimates of w/d can be obtained. For the impregnated brick $w/d \approx 0.1$ (from figure 5); for the as-manufactured brick w/d ranges between 0.1 and 0.001. The upper value for the as-manufactured brick was determined from scanning electron micrographs which suggest a grain boundary width, w , of less than ≈ 100 nm. The lower value is based on observations (using transmission electron microscopy) that most polycrystalline ceramic materials have amorphous grain boundaries with thicknesses greater than ≈ 1 nm [8-9].

Using the above estimates of the grain boundary thickness of the inter-aggregate phase, the following estimates of creep acceleration due to slag penetration are obtained: solution-precipitation (transport controlled), 0.01 to 1; solution-precipitation (interface controlled), 1 to 100; percolation, 1 to 10^6 . From these estimates, it is concluded that transport controlled solution precipitation is probably not a controlling mechanism for creep. By contrast, interface controlled solution-precipitation and percolation are both consistent with the creep data provided the grain boundary thickness, w , of the inter-aggregate phase is ≈ 100 nm. Further investigations of the microstructure of these refractory materials will be necessary to distinguish between these two mechanisms.

4.3 Refractory Lifetime

Penetration of slag into the refractory not only provides a mechanism for spalling of the hot face of the refractory, but also reduces the resistance of the refractory to creep, thereby decreasing its lifetime. Since increasing slag viscosity decreases both slag reactivity and creep rate, the present study suggests that refractory lifetime can be improved by increasing the viscosity of the vitreous phase formed by the penetration of slag into the hot face of the refractory. In the MgCr_2O_4 refractories, viscosity is reduced by ion transfer of magnesium from the spinel structure to the slag. Elimination of the MgO from the refractory or reducing its concentration should help to reverse this process. The addition of a network former, such as Al_2O_3 , to the brick should also help to increase slag viscosity by reducing the driving force for Al_2O_3 absorption from the slag. Methods such as these are currently being explored to increase the durability of chromite refractories in slagging gasifiers [28].

5. CONCLUSIONS

In this paper, the effect of slag penetration on the microstructure and creep behavior of a MgCr_2O_4 refractory was evaluated. The most interesting and significant finding relates to changes observed in chemical composition of the slag as it penetrated the refractory. Ionic reactions at the surface of the brick produced an intergranular vitreous phase with a diopside like ($\text{CaO}\cdot\text{MgO}\cdot 2\text{SiO}_2$) composition in contrast to the usual anorthite like ($\text{CaO}\cdot\text{Al}_2\text{O}_3\cdot 2\text{SiO}_2$) compositions found in western coal slags. Because of this change in composition, the viscosity of the intergranular vitreous phase formed in the refractory is probably lower and hence more

reactive than that of the original coal slag. These results suggest that refractory performance can be improved by chemical modification of the brick to prevent the reduction of slag viscosity during penetration, as by the addition of a network former such as Al_2O_3 to the refractory

The process of refractory disintegration is believed to involve creep deformation of the hot face of the brick, caused either by mechanically induced stresses, or by stresses that arise as a consequence of ion exchange reactions between the slag and the refractory brick. Mechanical stresses arise from the weight of the refractory wall, or from differential thermal expansion of the refractory. Stresses due to ion exchange reactions arise as a consequence of transport of Al_2O_3 and $\text{FeO}/\text{Fe}_2\text{O}_3$ from the slag to the spinel phase of the refractory brick, which results in a volume expansion of the hot face of refractory. Because of mechanical constraints at the hot face, this volume expansion also causes creep of the refractory brick.

As an increase in the creep rate of a factor of ≈ 3 occurred when slag was present in the refractory brick, creep of the refractory brick was found to be sensitive to penetration by slag. Creep of this refractory depends on the microstructure of the inter-aggregate bonding phase, in particular on the ratio, w/d , of the grain boundary width to the grain size of this phase. For the creep rate to increase as the refractory is impregnated with slag, w/d has to increase. More detailed experimental data on the microstructure will be needed for a quantitative comparison of these creep data with theory.

Footnotes:

1. In earlier experiments no protection was provided, and the slag reacted with the pure alumina loading platens and the ends of the silicon carbide push rods, whose deterioration indicated an erroneously high creep rate for the refractory specimen.
2. Although aluminum oxide is also present in the surface grains of the spinel phase, its concentration is less than $\approx 2\%$ and therefore is not shown in figure 7. As with ironoxide, the aluminum oxide is restricted to the surface of the refractory brick.
3. The precision of the analysis is determined by electron-beam spreading and interference of signals from the picrochromite grains with those from the glassy phase.
4. This slight solubility of the Cr_2O_3 in the slag at the temperature of operation of the gasifier is the primary reason that picrochromite refractories are resistant to coal slags.
5. Several specimens tested in the course of this study failed shortly after the strain exceeded the point of inflection on the stress-strain curve.
6. At the low oxygen pressures typical of gasifiers [2], iron will be present mainly in the +2 state.
7. Crack evolution by gas generation (e.g. iron bursting) is not believed to be a factor in the present study because of the absence of iron in the brick and because of the lack of evidence of other chemical reactions that might lead to gas evolution.
8. The simultaneous loss of MgO from the hot face provides a mechanism for a volume decrease, however, since the spinel phase is largely maintained at the hot face, the loss of MgO is accommodated by defects in the spinel structure. Therefore, the total volume loss should be minimal.

Table 1. Chemical composition (weight %) of selected slags used in laboratory studies.

Slag	CaO	Al ₂ O ₃	SiO ₂	FeO	MgO	Na ₂ O
synthetic coal slag	16	17	53	6	4	3
anorthite	22	22	56			
diopside	26		55		19	

Table 2. Composition of the intergranular vitreous phase in a Mg_2O_4 refractory from a coal gasifier plant, weight %.

Distance from hot face. (mm)	MgO	Al_2O_3	SiO_2	K_2O	CaO	Cr_2O_3
5	3.9	7.6	59.6	1.6	23.2	3.1
10	5.6	6.5	63.5	2.1	19.0	2.5
15	8.5	1.8	62.9	2.2	18.7	4.3
20	9.4	---	66.8	1.9	15.8	5.5
25	11.9	---	66.2	2.1	15.5	2.9

Table 3. Weight percent composition of the intergranular vitreous phase at the interior of MgCr_2O_4 refractory specimens after exposure to slag at 1500°C .

Vitreous phase	MgO	Cr_2O_3	CaO	SiO_2
Synthetic coal slag	8	4	20	68
Anorthite slag	9	2	24	65
Diopside slag	9	3	23	65

Table 4. Weight percent composition of MgCr_2O_4 grains in refractory impregnated with slag at 1500°C .

Location of Grains	MgO	Cr_2O_3	Al_2O_3	FeO
Original grains	20	80		
Coal gasifier slag				
Hot face	10	70	1	18
Specimen interior (>2 cm)	18	82		
Synthetic coal slag				
Specimen edge	11	69	5	15
Specimen interior	14	86		
Anorthite slag				
Specimen edge		94	6	
Specimen interior	15	85		
Diopside slag ^a				
Specimen edge	15	85		
Specimen interior	15	85		

^a Specimen exposed only 4 hours instead of the 24 hour period used for the synthetic coal slag and anorthite slag exposures.

Table 5. Time exponent for the creep of a MgCr_2O_4 refractory before and after impregnation by slag. The creep strain, ϵ , is characterized by a power function in time, t : $\epsilon = A \cdot t^m$, where A and m are empirical constants for the fit [7].

Test specimen	number of tests	m	(s.d.)
Before Impregnation:			
Series I ^a	9	0.74	(0.16)
Series II	6	0.64	(0.09)
After Impregnation:			
Slag impregnated in gasifier	4	0.65	(0.06)
Series II synthetic slag	5	0.60	(0.09)

^a Reference 7.

Table 6. Compressive creep strain rates calculated at 1 percent strain for MgCr₂O₄ refractory.

T/(°C)	σ /(MPa)	$10^5 (d\epsilon/dt)/h^{-1}$	Relative Creep Rate ^a
(A) Series II, Newly Produced			
1350	5.06	16.0	1.1
1400	2.25	5.73	0.6
	5.08	36.1	0.5
1450	1.52	5.04	1.7
	2.27	12.5	1.0
	5.09	77.4	<u>0.8</u>
			Mean 0.95 ±0.43
(B) Impregnated by synthetic coal slag.			
1450	0.75	2.9	2.9
	1.5	10.0	2.0
	3.02	26.2	1.1
1550	0.75	13.3	3.2
	1.50	90.3	<u>4.6</u>
			Mean 2.76 ±1.32
(C) Impregnated by coal gasifier slag.			
1400	3.01	19.9	1.8
	4.25	40.6	1.7
1500	0.65	6.3	4.2
	1.5	50.2	<u>5.0</u>
			Mean 3.18 ±1.68

^a Relative to Series I fit in reference 7.

Figure Captions:

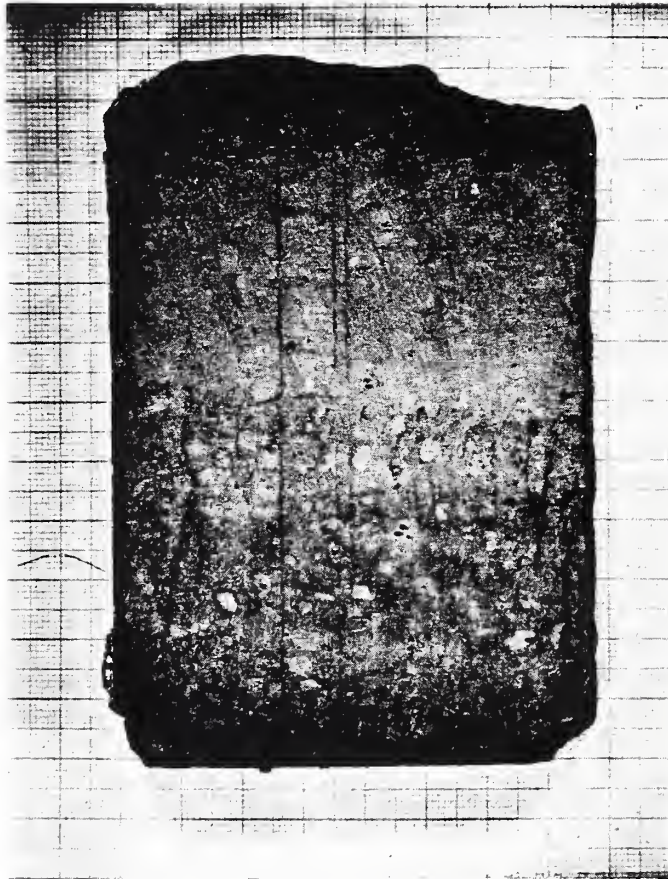
1. View of the sample of MgCr_2O_4 refractory brick from the coal gasifier plant. Crack like cavities are clearly visible near the exposed surface (right hand portion) of the brick. Slag penetration is indicated by the lighter shade of the brick towards the exposed surface. The major divisions of the graph in the background are in 1 cm units.
2. Microscopic view of an unpenetrated portion of the MgCr_2O_4 refractory brick that had been exposed in the gasifier plant. This portion of the brick was furthest from the hot face, and therefore was not penetrated by the slag. The dark areas in these micrographs are not void space, but regions of the microstructure that were not penetrated by the epoxy resin used to prepare polished section.
3. Scanning electron micrograph of one of the dark regions shown in figure 2. X-ray energy dispersive spectroscopy indicates these submicron grains to consist largely of MgCr_2O_4 . Traces of calcium, aluminum and silicon are also observed in these areas.
4. Plate-like Cr_2O_3 (corundum structure) particles in the MgCr_2O_4 aggregate indicates a chromium rich structure. The observation of this precipitate is consistent with reported and measured average compositions of the refractory brick.
5. Microscopic view of a slag penetrated portion of the refractory brick that had been exposed in the gasifier plant. (a) Regions between the large fused aggregate particles that were formerly the dark areas of figure 2 now consist of MgCr_2O_4 grains $\approx 10 \mu\text{m}$ in size, indicating considerable grain growth during exposure. (b) Grains near the hot face of the brick show an increase in the amount of intergranular vitreous phase.
6. Slag-filled, crack-like cavities in the slag impregnated hot face of the refractory from the gasifier. These are the same features that look like cracks in figure 1. The rounded shape of these cavities indicate a slow deformation process in their formation, probably caused by internal stresses in the hot face of the refractory.
7. Chemical analysis of the spinel grains in the penetrated portion of the brick obtained by using a scanning electron microscope with an x-ray energy dispersive spectroscopy attachment. Although aluminum was also detected close to the hot face, its concentration was less than 2 % and hence was not included on the figure.
8. Effect of a synthetic coal slag on the microstructure of an MgCr_2O_4 refractory brick specimen: (a) dense spinel coat on the external specimen surface indicates the transfer of aluminum and iron oxide from the slag to the surface of the specimen; (b) interior of the specimen indicates full penetration by slag. The specimen appears to be denser than a similar slag penetrated section from the coal gasifier.

9. Effect of anorthite slag on the microstructure of MgCr_2O_4 refractory brick: Coating of Cr_2O_3 (corundum) grains is found around the exterior surface of the specimen. Leaching of the MgO was sufficiently complete as to convert the spinel phase to corundum. The interior of the specimen was similar to figure 8b.
10. Effect of diopside slag on the microstructure of MgCr_2O_4 refractory brick. (a) Portion of slag-penetrated specimen wherein structural integrity has been maintained. Considerable grain growth has occurred within the inter-aggregate region; (b) Slag penetrated area of the specimen wherein the structure has been disrupted by the slag. Note the long crack-like cavities near the specimen surface.
11. Compressive creep strain of a MgCr_2O_4 refractory impregnated with slag from a coal gasifier. Observed strain (circles) was determined for specimens subjected to applied stresses of (a) 3.01 MPa and (b) 4.25 MPa in nitrogen gas at 1400°C . A solid curve is a least squares fit of equation 1 while a dashed curve predicts [7] the strain of the newly produced refractory under the same stress and temperature.
12. Compressive creep strain of a MgCr_2O_4 refractory impregnated with synthetic coal slag. Observed strain (circles) and least squares fits of equation 1 for work-hardened creep (solid line) are plotted for tests conducted in nitrogen gas at 1450°C under applied stress of 1.5 and 3.0 MPa respectively.
13. Schematic diagram of mechanisms of slag attack on MgCr_2O_4 refractories. Al^{+3} and $\text{Fe}^{+2}/\text{Fe}^{+3}$ enter into the spinel structure at the hot face, while Mg^{+2} and Cr^{+3} leave the surface grains of the refractory. The iron and the aluminum reduce the melting point of the spinel grains, a consequence of which is enhanced solution of the refractory in the slag. Within the refractory, the aluminum and iron leave the slag to be replaced by chromium and magnesium, which changes the composition from one similar to an anorthite melt to one similar to a diopside melt. At the same time, the submicron grains that lie between the larger aggregate particles grow in size. This grain growth coupled with transport of matter from the melt to the spinel grains of the brick cause the hot face to bloat, crack and eventually spall from the main body of the refractory brick.
14. Schematic diagram of the microstructure of a refractory brick. The spacing and size of the large aggregate grains is given by W and D respectively. The aggregate particles are bonded together by a much finer grain microstructure, in which small grains of refractory of size d are bonded by a vitreous matrix. The spacing between the finer grain particles is w . Because deformation occurs more easily within the finer grain bonding microstructure, the creep rate of the refractory is largely determined by this inter-aggregate microstructure.

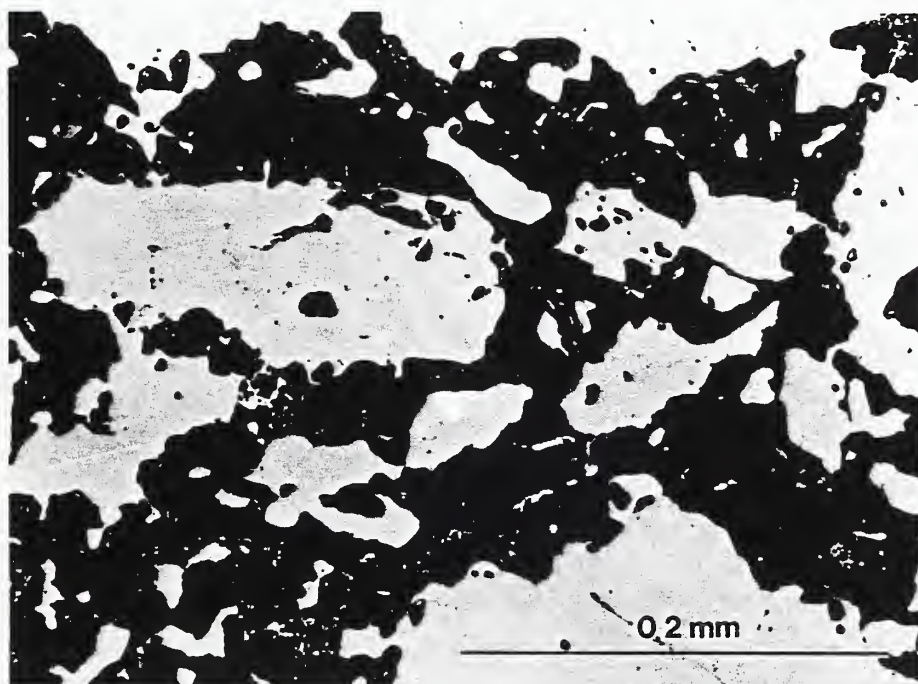
References:

1. W.T. Bakker, S. Greenberg, M. Trondt and U. Gerhardus, "Refractory Practice in Slagging Gasifiers," Am. Ceram. Soc. Bull., 63 [7], 870-76 (1984).
2. C.R. Kennedy, "Coal Slag - Refractory Compatibility Studies Progress to Date," Am. Ceram. Soc. Proc., 2[11-12], 1156-70 (1981).
3. C.R. Kennedy, "Refractories for Application in Slagging Gasifiers," Proc. Fourth An. Conf. on Mat. for Coal Conv. and Util., Gaithersburg, MD, Oct. (1979), DOE Rep. CONF 791014, 1979.
4. C.R. Kennedy, "Compatibility of Water-Cooled Chromia-Containing Refractories with a High Iron Oxide Acidic Coal-Ash Slag at 1575°C," Mat. for Energy Systems, 3[3], 39-47 (1981).
5. W.T. Bakker, "Design Aspects of Refractory Wear by Slag Erosion/Corrosion," Am. Ceram. Soc. Proc., 2[11-12], 1202-8 (1981).
6. S. Greenberg and R.B. Poeppe, "The Corrosion of Ceramic Refractories Exposed to Synthetic Coal Slags by Means of the Rotating-Cylinder Technique: Final Report," Tech. Report No. ANL/FE-85-15, Argonne National Lab., Argonne, IL, April, 1986.
7. R.F. Krause, Jr., "Compressive Strength and Creep Behavior of a Magnesium Chromite Refractory," Ceramic Eng. and Science Proc. 7, [1-2], 220-228 (1986).
8. D.R. Clarke, "On the Detection of Thin Intergranular Films by Electron Microscopy," Ultramicroscopy, 4[1], 33-44 (1979)
9. D.R. Clarke, "On the Equilibrium Thickness of Intergranular Glass Phases in Ceramic Materials," J. Am. Ceram. Soc., in press.
10. R.M. El-Shahat and J. White, "Phase Equilibrium relationships in Spinel-Silicate Systems," Trans. Brit. Ceramic Soc. 65, 309-36, (1966).
11. R.M. El-Shahat and J. White, "The systems $MgAl_2O_4 \cdot MgCr_2O_4 \cdot Ca_2SiO_4$ and $MgFe_2O_4 \cdot MgCr_2O_4 \cdot Ca_2SiO_4$," Trans. Brit. Ceramic Soc. 63, 313-30 (1964).
12. E-S Chen and O. Buyukozturk, "Modeling of Long Term Corrosion Behavior of Refractory Linings in Slagging Gasifiers," Am. Ceram. Soc. Bull. 54[7], 995-1000 (1985).
13. W.J. Moore, Physical Chemistry, Prentice-Hall In., Englewood Cliffs, NJ (1972).
14. R. Terai and R. Hayanic, "Ionic Diffusion in Glasses," J. Non-Cryst. Solids, 18, 217-64 (1975).

15. C.M. Scarfe, D.J. Cronin, J.T. Wenzel and D.A. Kauffman, "Viscosity-Temperature Relationships at 1 atm in the System Diopside-Anorthite," *Am. Mineralogist*, 68, 1083-88 (1983).
16. E.-S. Chen and O. Buyukozturk, "Methodology for Thermomechanical Analysis of Brittle Systems," *Am. Ceram. Soc. Bull.* 54[7], 982-988 (1985).
17. E.-S. Chen and O. Buyukozturk, "Thermomechanical Behavior and Design of Refractory Linings for Slagging Gasifiers," *Am. Ceram. Soc. Bull.* 54[7], 988-94 (1985).
18. A.G. Evans and W. Blumenthal, "High Temperature Failure in Ceramics," pp.423-448 in *Fracture Mechanics of Ceramics, Vol. 6, Measurements, Transformations and High-Temperature Fracture*, R.C. Bradt, A.G. Evans, D.P.H. Hasselman and F.F. Lange, eds. Plenum Press, New York (1983).
19. A.G. Evans and W. Blumenthal, "High Temperature Failure Mechanisms in Ceramic Polycrystals," pp. 487-505 in *Deformation of Ceramic Materials II: Materials Science Research, Vol. 18*, R.E. Tressler and R.C. Bradt, eds., Plenum Press, New York (1984).
20. F.C. Monkman and N.J. Grant, "An Empirical Relationship between Rupture Life and Minimum Creep Rate in Creep-Rupture Tests," *Proc. ASTM* 56, 593-620 (1956).
21. R. Kossowsky, D. G. Miller and E.S. Diaz, "Tensile and Creep Strengths of Hot-Pressed Si_3N_4 ," *J. Mater. Sci.* 15, 983-97 (1975).
22. S.M. Johnson, B.J. Dalgleish and A.G. Evans, "High-Temperature Failure of Polycrystalline Alumina: III, Failure Times" *J. Am. Ceram. Soc.* 67, 759-63 (1984).
23. S.M. Wiederhorn, B.J. Hockey, R.F. Krause, Jr. and K. Jakus, "Creep and Fracture of a Vitreous-Bonded Aluminum Oxide," *J. Mater. Sci.* 21, 810-824 (1986).
24. D.C. Drucker, "Engineering and Continuum Aspects of High-Strength Materials," pp. 795-833 in *High Strength Materials*, V.F. Zackay, ed., John Wiley and Sons, Inc., New York (1965).
25. R. Raj, "Creep in Polycrystalline Aggregates by Matter Transport Through a Liquid Phase," *J. Geophys. Res.* 87 [B6], 4731-39 (1982).
26. R. Raj and C.K. Chyung, "Solution-Precipitation Creep in Glass Ceramics," *Acta Met.* 29, 159-66 (1981).
27. J.-G. Wang and R. Raj, "Mechanisms of Superplastic Flow in a Fine-Grained Ceramic Containing some Liquid Phase," *J. Am. Ceram. Soc.* 67, 399-409 (1984).
28. L.J. Trostel, Jr., private communication, The Norton Company, Worcester, MA.



1. View of the sample of MgCr_2O_4 refractory brick from the coal gasifier plant. Crack like cavities are clearly visible near the exposed surface (right hand portion) of the brick. Slag penetration is indicated by the lighter shade of the brick towards the exposed surface. The major divisions of the graph in the background are in 1 cm units.



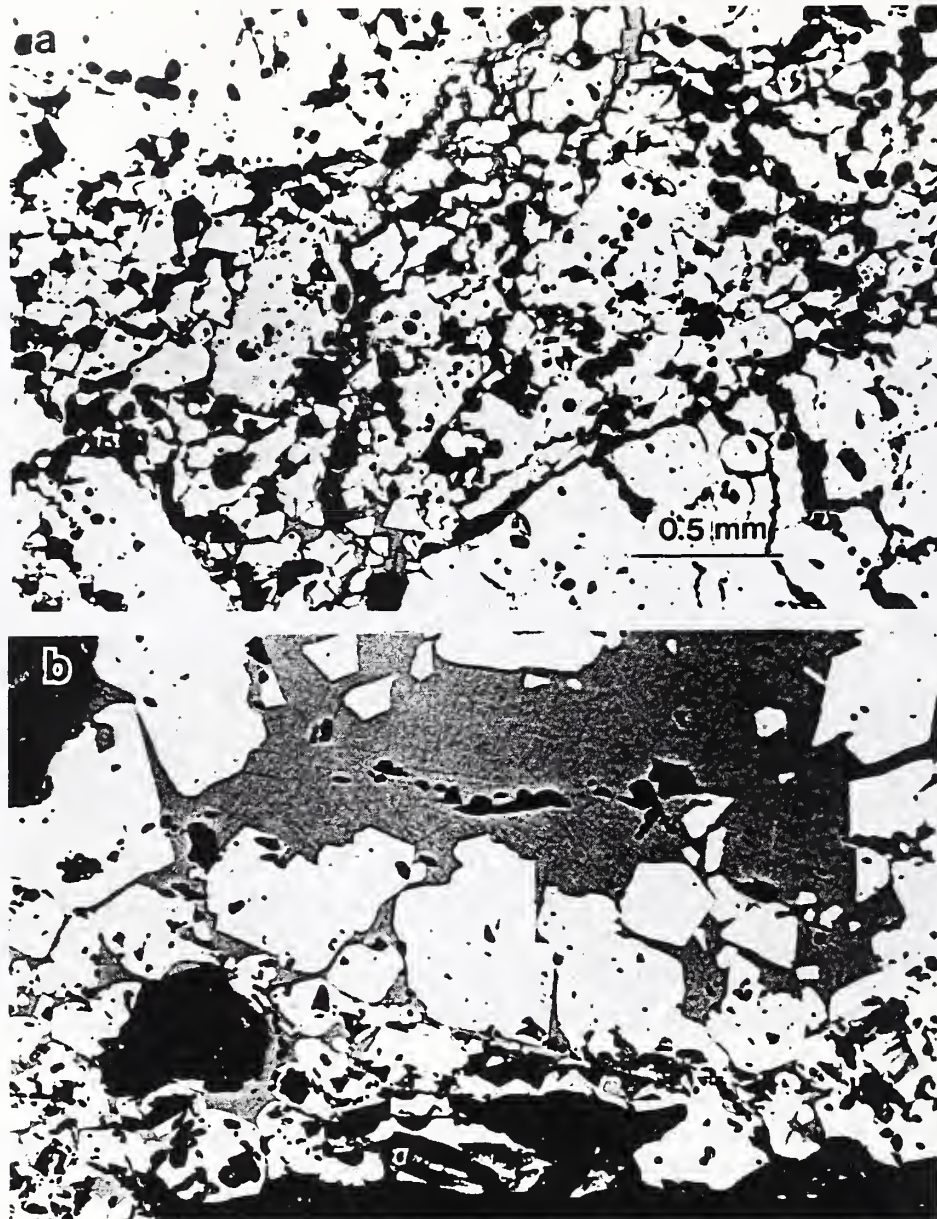
2. Microscopic view of an unpenetrated portion of the MgCr_2O_4 refractory brick that had been exposed in the gasifier plant. This portion of the brick was furthest from the hot face, and therefore was not penetrated by the slag. The dark areas in these micrographs are not void space, but regions of the microstructure that were not penetrated by the epoxy resin used to prepare polished section.



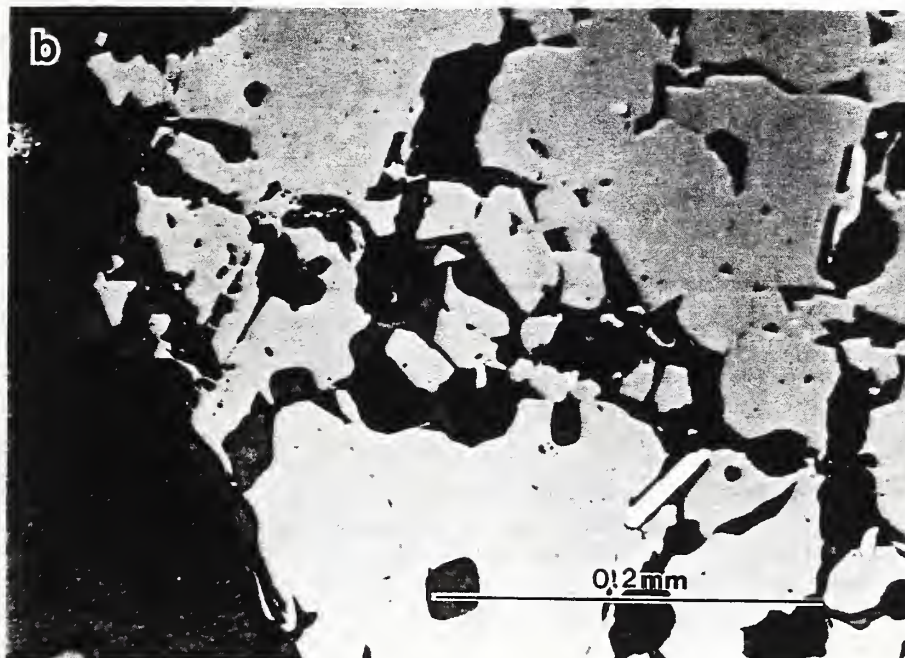
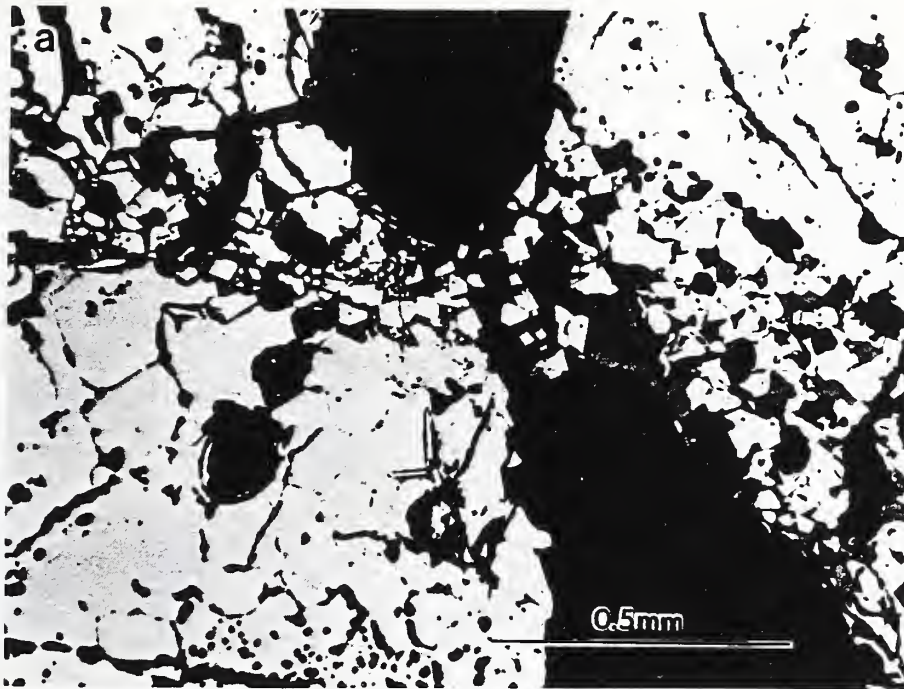
3. Scanning electron micrograph of one of the dark regions shown in figure 2. X-ray energy dispersive spectroscopy indicates these submicron grains to consist largely of MgCr_2O_4 . Traces of calcium, aluminum and silicon are also observed in these areas.



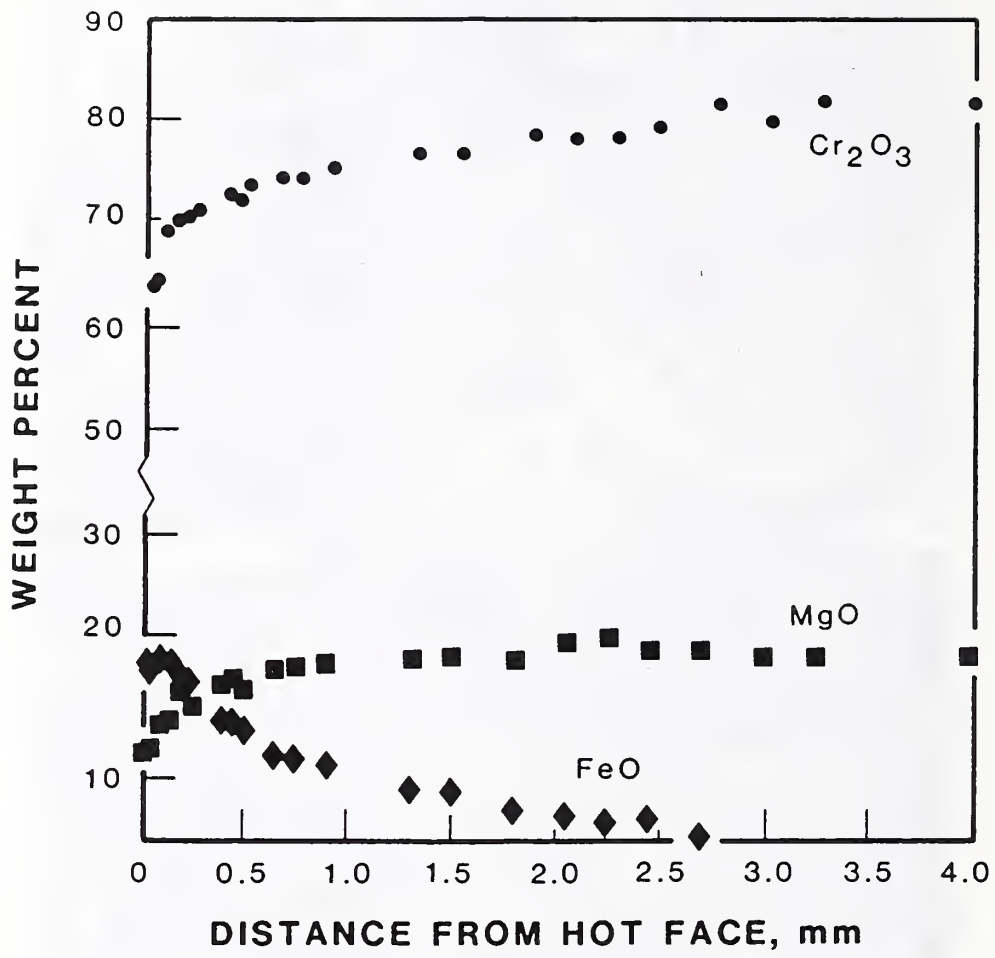
4. Plate-like Cr_2O_3 (corundum structure) particles in the MgCr_2O_4 aggregate indicates a chromium rich structure. The observation of this precipitate is consistent with reported and measured average compositions of the refractory brick.



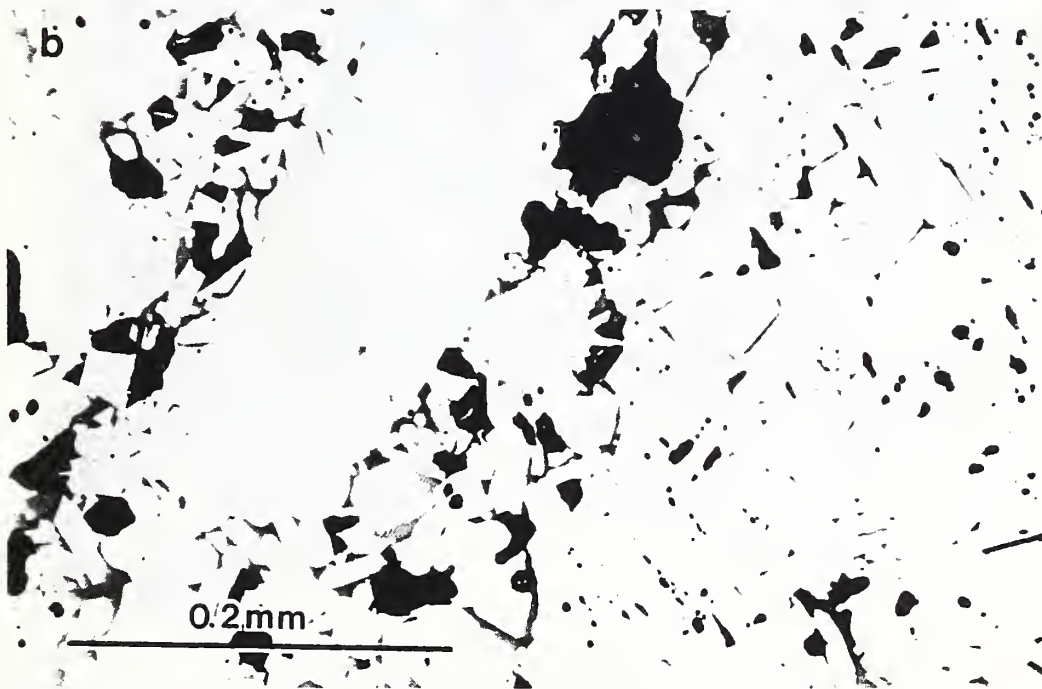
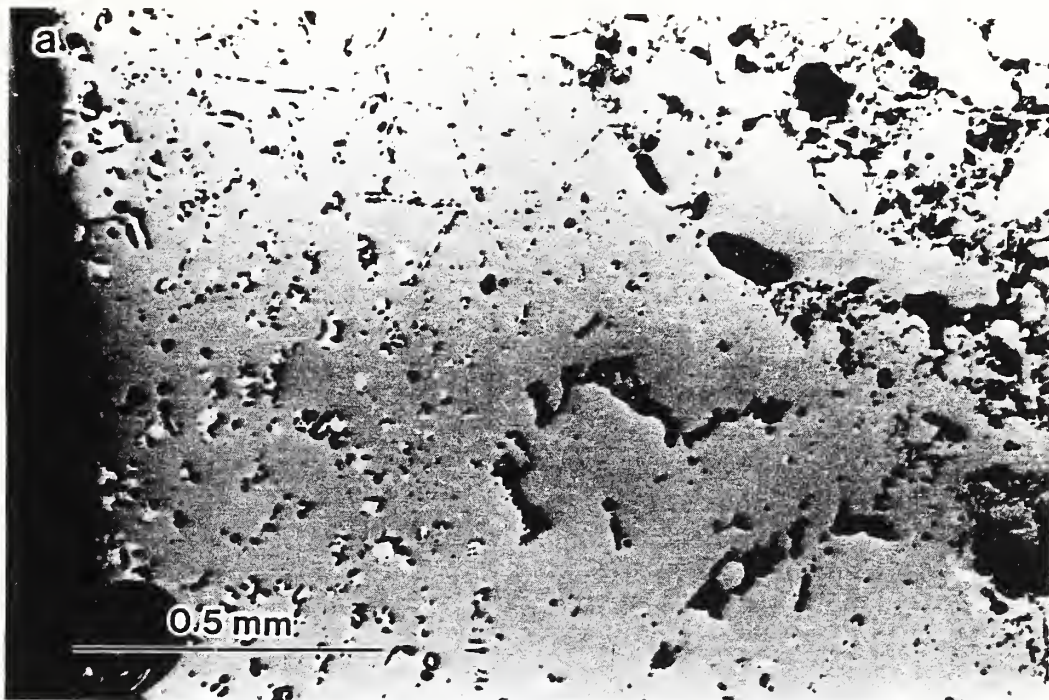
5. Microscopic view of a slag penetrated portion of the refractory brick that had been exposed in the gasifier plant. (a) Regions between the large fused aggregate particles that were formerly the dark areas of figure 2 now consist of MgCr_2O_4 grains $\approx 10 \mu\text{m}$ in size, indicating considerable grain growth during exposure. (b) Grains near the hot face of the brick show an increase in the amount of intergranular vitreous phase.



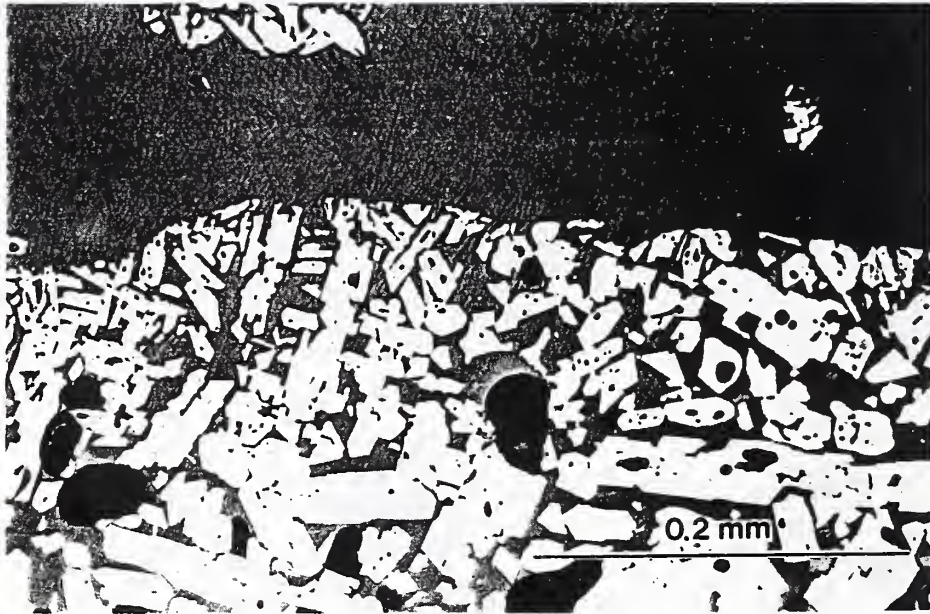
6. Slag-filled, crack-like cavities in the slag impregnated hot face of the refractory from the gasifier. These are the same features that look like cracks in figure 1. The rounded shape of these cavities indicate a slow deformation process in their formation, probably caused by internal stresses in the hot face of the refractory.



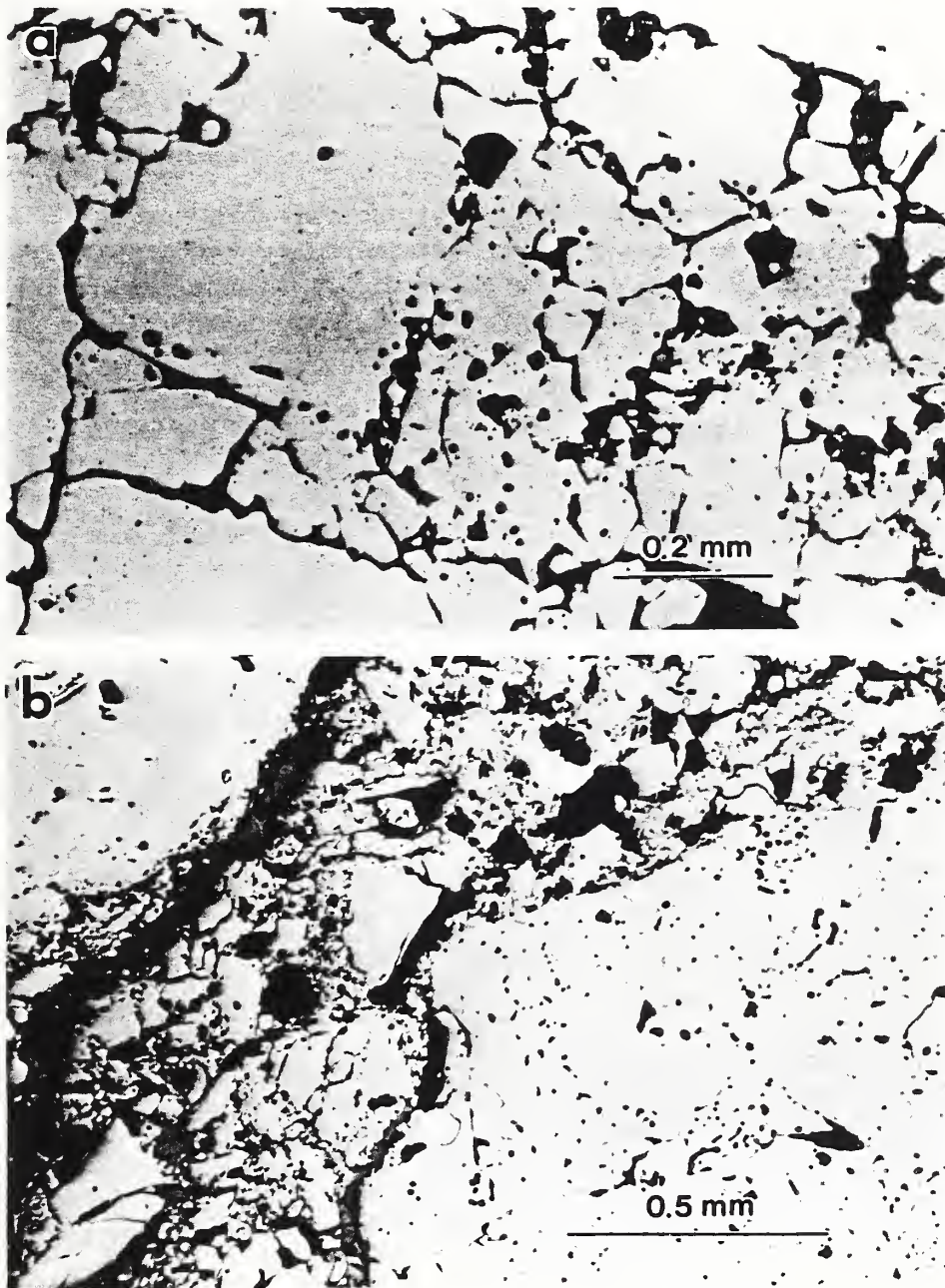
7. Chemical analysis of the spinel grains in the penetrated portion of the brick obtained by using a scanning electron microscope with an x-ray energy dispersive spectroscopy attachment. Although aluminum was also detected close to the hot face, its concentration was less than 2% and hence was not included on the figure.



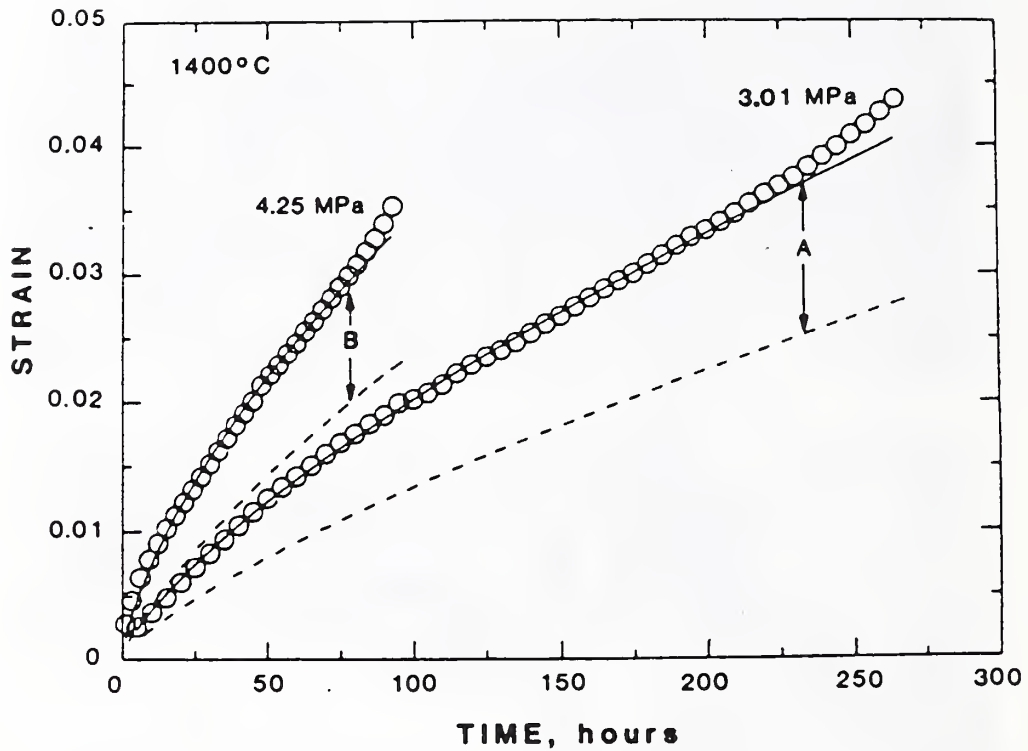
8. Effect of a synthetic coal slag on the microstructure of an MgCr_2O_4 refractory brick specimen: (a) dense spinel coat on the external specimen surface indicates the transfer of aluminum and iron oxide from the slag to the surface of the specimen; (b) interior of the specimen indicates full penetration by slag. The specimen appears to be denser than a similar slag penetrated section from the coal gasifier.



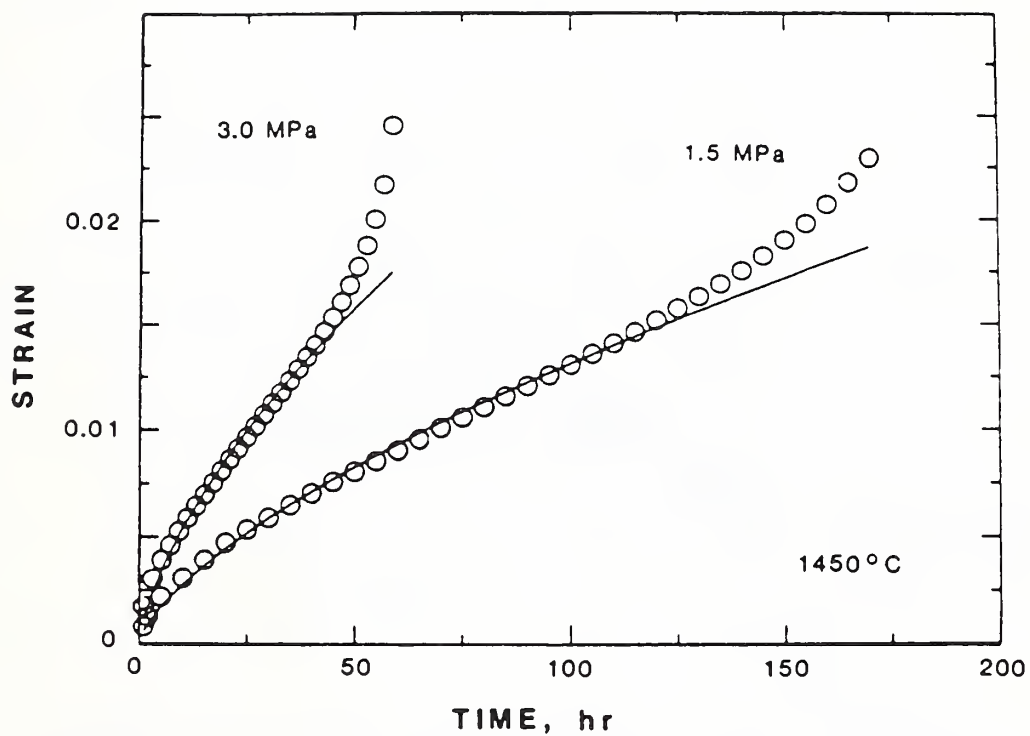
9. Effect of anorthite slag on the microstructure of MgCr_2O_4 refractory brick: Coating of Cr_2O_3 (corundum) grains is found around the exterior surface of the specimen. Leaching of the MgO was sufficiently complete as to convert the spinel phase to corundum. The interior of the specimen was similar to figure 8b.



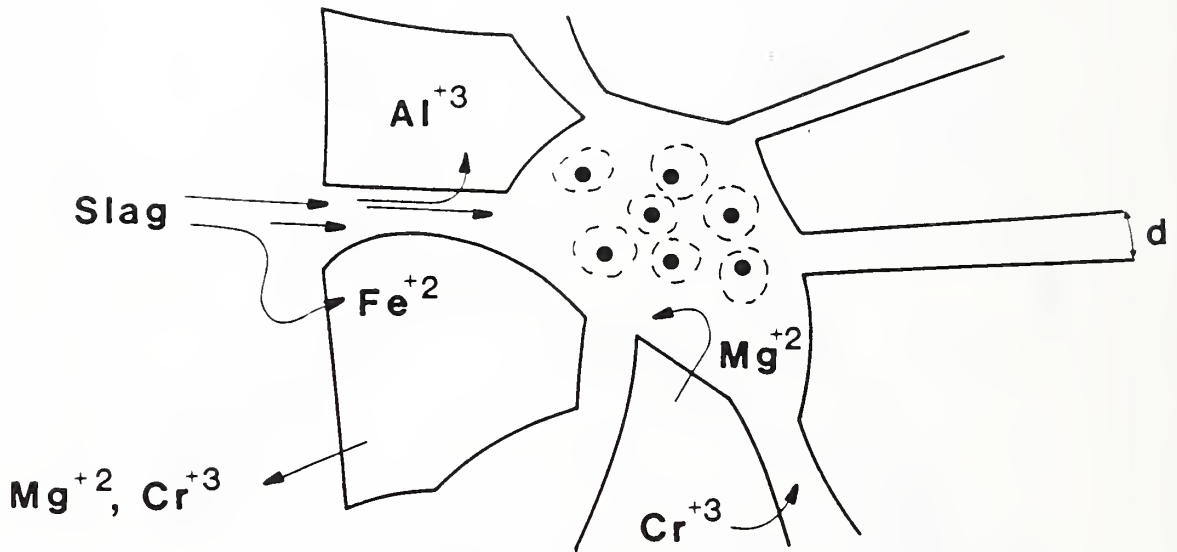
10. Effect of diopside slag on the microstructure of MgCr_2O_4 refractory brick. (a) Portion of slag-penetrated specimen wherein structural integrity has been maintained. Considerable grain growth has occurred within the inter-aggregate region; (b) Slag penetrated area of the specimen wherein the structure has been disrupted by the slag. Note the long crack-like cavities near the specimen surface.



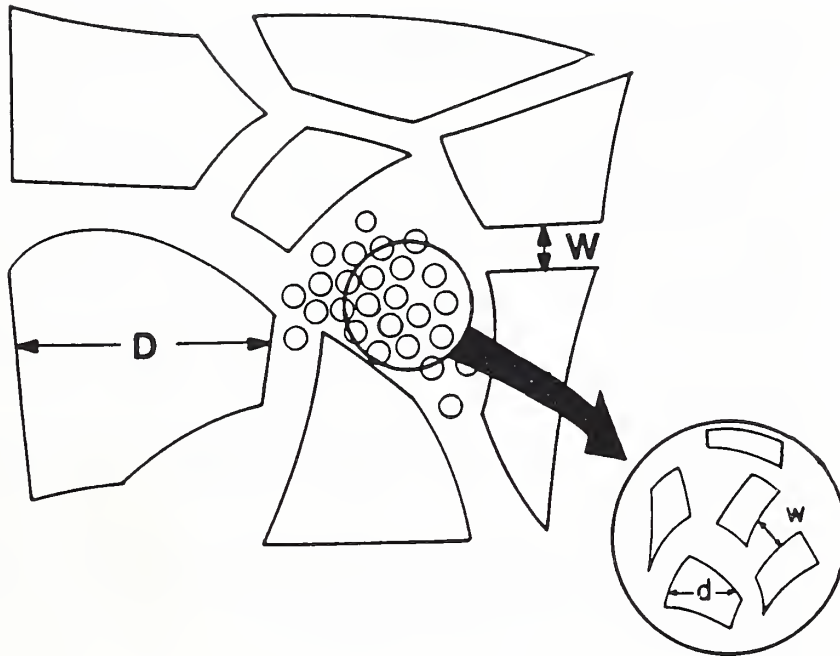
11. Compressive creep strain of a MgCr_2O_4 refractory impregnated with slag from a coal gasifier. Observed strain (circles) was determined for specimens subjected to applied stresses of (a) 3.01 MPa and (b) 4.25 MPa in nitrogen gas at 1400°C . A solid curve is a least squares fit of equation 1 while a dashed curve predicts [7] the strain of the newly produced refractory under the same stress and temperature.



12. Compressive creep strain of a $MgCr_2O_4$ refractory impregnated with synthetic coal slag. Observed strain (circles) and least squares fits of equation 1 for work-hardened creep (solid line) are plotted for tests conducted in nitrogen gas at $1450^\circ C$ under applied stress of 1.5 and 3.0 MPa respectively.



13. Schematic diagram of mechanisms of slag attack on $MgCr_2O_4$ refractories. Al^{+3} and Fe^{+2}/Fe^{+3} enter into the spinel structure at the hot face, while Mg^{+2} and Cr^{+3} leave the surface grains of the refractory. The iron and the aluminum reduce the melting point of the spinel grains, a consequence of which is enhanced solution of the refractory in the slag. Within the refractory, the aluminum and iron leave the slag to be replaced by chromium and magnesium, which changes the composition from one similar to anorthite melt to one similar to a diopside melt. At the same time, the submicron grains that lie between the larger aggregate particles grow in size. This grain growth coupled with transport of matter from the melt to the spinel grains of the brick cause the hot face to bloat, crack and eventually spall from the main body of the refractory brick.



14. Schematic diagram of the microstructure of a refractory brick. The spacing and size of the large aggregate grains is given by W and D respectively. The aggregate particles are bonded together by a much finer grain microstructure, in which small grains of refractory of size d are bonded by a vitreous matrix. The spacing between the finer grain particles is w . Because deformation occurs more easily within the finer grain bonding microstructure, the creep rate of the refractory is largely determined by this inter-aggregate microstructure.

DISTRIBUTION LIST

1. A. P. GREEN REFRACTORIES COMPANY, Green Blvd., Mexico,
Missouri 65265
J. L. Hill
2. ALLEGHENY LUDLUM STEEL CORPORATION, Brackenridge, PA 15014
G. L. Houze
3. ALLISON GAS TURBINE OPERATIONS, Mail Stop W-5, P. O. Box 420,
Indianapolis, Indiana 46206
P. Khandelwal
4. ARGONNE NATIONAL LABORATORY, 9700 S. Cass Avenue, Argonne, IL 60439
W. A. Ellingson
5. BABCOCK AND WILCOX, Fossil Power Generation Division, 20 South
Van Buren Avenue, Barberton, OH 44203
M. Gold
6. BETHLEHEM STEEL CORPORATION, Bethlehem, PA 18016
B. L. Bramfitt
7. CBI INDUSTRIES, 800 Jorie Blvd., Oak Brook, IL 60521
W. R. Mikesell
8. CANADA CENTER FOR MINERAL AND ENERGY TECHNOLOGY, 555 Booth Street,
Ottawa, Ontario, Canada K1A 0B1
Mahee Sahoo
9. CHEVRON CORPORATION, P. O. Box 4012, Richmond, CA 94804
A. G. Imgram
10. COMBUSTION ENGINEERING, INC., 1000 Prospect Hill Road, Windsor,
CT 06095
E. A. Steen
11. COMMISSION OF THE EUROPEAN COMMUNITIES, Petten Establishment,
Postbus 2, 1755 ZG Petten, The Netherlands
12. DOW CORNING CORPORATION, 3901 S. Saginaw Road, Midland, MI 48640
H. W. Foglesong
13. EG&G IDAHO, INC., Idaho National Engineering Laboratory,
P. O. Box 1625, Idaho Falls, ID 83415
A. D. Donaldson

- 14-15. ELECTRIC POWER RESEARCH INSTITUTE, 3412 Hillview Avenue,
P. O. Box 10412, Palo Alto, CA 94303
W. T. Bakker
J. T. Stringer
16. EXXON RESEARCH AND ENGINEERING COMPANY, P. O. Box 101,
Florham Park, NY 07932
M. J. Humphries
17. FOSTER WHEELER DEVELOPMENT CORPORATION, Materials Technology
Department, John Blizzard Research Center, 12 Peach Tree Hill Road,
Livingston, NY 07039
J. L. Blough
18. GAS RESEARCH INSTITUTE, 8600 West Bryn Mawr Avenue, Chicago,
IL 60631
H. S. Meyer
19. KENTUCKY CENTER FOR ENERGY RESEARCH, Iron Works Pike, P. O.
Box 13015, Lexington, KY 40512
V. K. Sethi
20. IOWA STATE UNIVERSITY, Materials Science and Engineering
Department, Ames, Iowa 50011
T. D. McGee
21. KENNAMETAL, INC., Philip McKenna Laboratory, 1011 Old Salem Road,
P. O. Box 639, Greensburg, PA 15601
B. North
22. LANXIDE CORPORATION, Tralee Industrial Park, Newark, Delaware 19711
E. M. Anderson
23. LAVA CRUCIBLE-REFRACTORIES CO., P. O. Box 278, Zelienople,
PA 106063
W. M. Davis
24. LUKENS STEEL COMPANY, Coatesville, PA 19320
J. A. Gulya
25. MASSACHUSETTS INSTITUTE OF TECHNOLOGY, Department of Civil
Engineering, 77 Massachusetts Avenue, Cambridge, MA 02139
O. Buyukozturk
26. MOBIL RESEARCH AND DEVELOPMENT CORPORATION, P. O. Box 1026,
Princeton, NJ 08540
R. C. Searles

27. MONTANA STATE UNIVERSITY, Physics Department, Bozeman, MT 59717
R. J. Pollina
28. NASA-LEWIS RESEARCH CENTER, Lewis Library, MS 60-3, 21000 Brookpark
Road, Cleveland, OH 44135
K. Grasse
29. NATIONAL BUREAU OF STANDARDS, Materials Building, Gaithersburg,
MD 20899
S. J. Dapkunas
30. NATIONAL MATERIALS ADVISORY BOARD, National Research Council,
2101 Constitution Avenue, Washington, DC 20418
K. M. Zwilsky
- 31-40. OAK RIDGE NATIONAL LABORATORY, P. O. Box X, Oak Ridge, TN 37831
Central Research Library (2)
Document Reference Section
Laboratory Records Department (2)
Laboratory Records, ORNL RC
ORNL Patent Section
R. A. Bradley
P. T. Carlson
R. R. Judkins
41. PENNSYLVANIA STATE UNIVERSITY, College of Earth and Mineral
Sciences, University Park, PA 16802
A. Muan
42. SHELL DEVELOPMENT COMPANY, P. O. Box 1380, Houston, TX 77001
L. W. R. Dicks
43. SHELL OIL COMPANY, Engineering Services, P. O. Box 3105,
Houston, TX 77001
E. L. Creamer
44. SOUTHWEST RESEARCH INSTITUTE, 6220 Culebra Road, P. O.
Drawer 29510, San Antonio, TX 78284
F. F. Lyle, Jr.
45. THE TORRINGTON COMPANY, Research Department, 59 Field Street,
Corrington, Connecticut 06790
W. J. Chmura
46. UNITED TECHNOLOGIES RESEARCH CENTER, East Hartford,
Connecticut 06108
K. M. Prewc

47. VIRGINIA POLYTECHNIC INSTITUTE AND STATE UNIVERSITY, Department of Materials Engineering, Blacksburg, VA 24601
J. J. Brown, Jr.
- 48-50. DOE, OFFICE OF FOSSIL ENERGY, Washington, DC 20545
J. P. Carr
F. M. Glaser
M. I. Singer
51. DOE, OFFICE OF BASIC ENERGY SCIENCES, Materials Sciences Division, Washington, DC 20545
F. V. Nolfi, Jr.
52. DOE, ENERGY CONVERSION & UTILIZATION TECHNOLOGIES DIVISION, Route Symbol CE-142, Forrestal Building, Washington, DC 20585
J. J. Eberhardt
53. DOE, OFFICE OF VEHICLE AND ENGINE R&D, Route Symbol CE-131, Forrestal Building, Washington, DC 20585
R. B. Schulz
54. DOE, OAK RIDGE OPERATIONS OFFICE, P. O. Box E, Oak Ridge, TN 37831
Assistant Manager for Energy Research and Development
- 55-56. DOE, MORGANTOWN ENERGY TECHNOLOGY CENTER, P. O. Box 880, Morgantown, WV 26505
D. Dubis
M. Ghate
J. S. Wilson
57. DOE, PITTSBURGH ENERGY TECHNOLOGY CENTER, P. O. Box 10940, Pittsburgh, PA 15236
S. W. Chun
- 58-59. DOE, OFFICE OF SCIENTIFIC AND TECHNICAL INFORMATION, Office of Information Services, P. O. Box 62, Oak Ridge, TN 37831
For distribution by microfiche as shown in DOE/TIC-4500, Distribution Categories UC-90c (Coal Conversion and Utilization-Coal Gasification), -d (Coal Conversion and Utilization-Liquefaction), and -h (Coal Conversion and Utilization-Materials and Components)

(Minimum of 2 copies to OSTI; original preferred)

U.S. DEPT. OF COMM. BIBLIOGRAPHIC DATA SHEET <i>(See instructions)</i>	1. PUBLICATION OR REPORT NO. NBSIR 87-3584	2. Performing Organ. Report No.	3. Publication Date JUNE 1987
4. TITLE AND SUBTITLE EFFECT OF SLAG PENETRATION ON THE MECHANICAL PROPERTIES OF REFRACTORIES: FINAL REPORT			
5. AUTHOR(S) S.M. Wiederhorn and R.F. Krause, Jr.			
6. PERFORMING ORGANIZATION <i>(If joint or other than NBS, see instructions)</i> NATIONAL BUREAU OF STANDARDS DEPARTMENT OF COMMERCE WASHINGTON, D.C. 20234		7. Contract/Grant No. DE-AI05-830R21349	8. Type of Report & Period Covered FINAL
9. SPONSORING ORGANIZATION NAME AND COMPLETE ADDRESS <i>(Street, City, State, ZIP)</i> U.S. Department of Energy, Advanced Research and Technology Development, Fossil Energy Materials Program, Oak Ridge National Laboratory, Oak Ridge, TN 37831			
10. SUPPLEMENTARY NOTES <input type="checkbox"/> Document describes a computer program; SF-185, FIPS Software Summary, is attached.			
11. ABSTRACT <i>(A 200-word or less factual summary of most significant information. If document includes a significant bibliography or literature survey, mention it here)</i>			
12. KEY WORDS <i>(Six to twelve entries; alphabetical order; capitalize only proper names; and separate key words by semicolons)</i> ceramics; corrosion; creep; gasification; refractories			
13. AVAILABILITY <input checked="" type="checkbox"/> Unlimited <input type="checkbox"/> For Official Distribution. Do Not Release to NTIS <input type="checkbox"/> Order From Superintendent of Documents, U.S. Government Printing Office, Washington, D.C. 20402. <input checked="" type="checkbox"/> Order From National Technical Information Service (NTIS), Springfield, VA. 22161		14. NO. OF PRINTED PAGES 144 15. Price \$18.95	



